VDI

REIHE 12
VERKEHRSTECHNIK/
FAHRZEUGTECHNIK

Fortschritt-Berichte VDI

Thorsten Lajewski, M. Sc.
Nufringen

NR. 816

Friction Potential Estimation for Autonomous Driving

BAND
1|1

VOLUME
1|1

Friction Potential Estimation for Autonomous Driving

vorgelegt von
Thorsten Lajewski, M. Sc.
geb. in Remscheid

an der Fakultät V – Verkehrs- und Maschinensysteme
der Technische Universität Berlin
zur Erlangung des akademischen Grades

Doktor der Ingenieurwissenschaften
- Dr.-Ing. -

genehmigte Dissertation

Promotionsausschuss:

Vorsitzender:	Prof. Dr.-Ing. Utz von Wagner
Gutachter:	Prof. Dr.-Ing. Steffen Müller
Gutachter:	Prof. Dr.techn. Manfred Plöchl

Tag der wissenschaftlichen Aussprache: 20.09.2021

Berlin 2021

VDI

REIHE 12
VERKEHRSTECHNIK/
FAHRZEUGTECHNIK

Fortschritt-Berichte VDI

Thorsten Lajewski, M. Sc.,
Nufringen

NR. 816

Friction Potential Estimation for Autonomous Driving

BAND
1|1

VOLUME
1|1

VDI verlag

VDI verlag

Lajewski, Thorsten, M. Sc.

Friction Potential Estimation for Autonomous Driving

Fortschritt-Berichte VDI, Reihe 12, Nr. 816. Düsseldorf: VDI Verlag 2022.

192 Seiten, 62 Bilder, 25 Tabellen.

ISBN 978-3-18-381612-5, E-ISBN 978-3-18-681612-2, ISSN 0178-9449

67,00 EUR/VDI-Mitgliederpreis: 60,30

Für die Dokumentation: Reifen – Reibwert – Autonomes Fahren – Trajektorienplanung – Straßenbau – Straßenwetter – Klassifizierungsverfahren

Keywords: Tyre – Friction – Autonomous Driving – Trajectory Planning – Road Maintenance – Road Weather – Classification Methods

Autonomous vehicles need information about the environment for trajectory planning. This information is usually stored in a high-definition map. This map is made available to the vehicle. This thesis deals with the friction potential, which is important for planning. The unitless value determines the maximum forces that can be transmitted between tyre and road. The friction potential is a function of many influencing factors. In this work, possibilities are evaluated to capture the most important of these influencing factors, the road surface and the intermediate layer, via external data sources. To determine the influence of the road surface, friction measurement methods established in road construction are compared with vehicle measurements. To determine the intermediate layer, data from weather stations, rain radar and a test vehicle are evaluated.

Bibliographische Information der Deutschen Bibliothek
Die Deutsche Bibliothek verzeichnet diese Publikation in der Deutschen Nationalbibliographie; detaillierte bibliographische Daten sind im Internet unter www.dnb.de abrufbar.

Bibliographic information published by the Deutsche Bibliothek (German National Library)
The Deutsche Bibliothek lists this publication in the Deutsche Nationalbibliographie (German National Bibliography); detailed bibliographic data is available via Internet at www.dnb.de.

Zugl.: Berlin, Technische Universität, Diss., 2021

ISBN 978-3-18-381612-5, E-ISBN 978-3-18-681612-2, ISSN 0178-9449

Danksagung

Die vorliegende Promotionsschrift ist das Ergebnisse mehrerer Jahre intensiver Arbeit. Die Resultate wurden von vielen Menschen mit geformt oder erst ermöglicht. Zuallererst möchte ich Herrn Prof. Dr.-Ing. Steffen Müller für die Betreuung der Arbeit danken. Die Treffen in Berlin und die Forschungsergebnisse des Fachgebiets Kraftfahrzeugtechnik haben viel zur Ausrichtung der Arbeit beigetragen. Mein weiterer Dank gilt Prof. Dr.techn. Manfred Plöchl für die Übernahme des Zweitgutachtens.

Einen großen Beitrag zu der Dissertation haben auch viele meiner Kollegen der Daimler AG geleistet, bei der ich zu dem spannenden Thema Reibwertpotentialschätzung forschen konnte. Insbesondere gilt hier der Dank Alex Wütherich, mit dem ich unter anderem zahlreiche Tage mit Messfahrten und Datenaufbereitung verbracht habe. Zusätzlich hat der Austausch mit Dr.-Ing. Jochen Rauh und Prof. Dr.-Ing Dieter Ammon viele Impulse bei der Umsetzung der Arbeit gesetzt. Zudem hat auch mein ehemaliger Büronachbar Josef Dürnberger viel geholfen, indem er den initialen Aufbau des Messfahrzeugs geplant und mir viel zum Thema Messtechnik beigebracht hat. Auch unsere Werkstatt hat bei den zahlreichen nötigen Auf- und Umbauten des Messfahrzeugs große Unterstützung geleistet.

Die Durchführung der Messungen mit den Mess-LKWs SKM und RoadSTAR wäre ohne die Unterstützung weiterer Personen nicht möglich gewesen. Ein Dank gilt Dr. Ulrike Stöckert von der Bundesanstalt für Straßenwesen, die mir einen ersten Einblick in die Daten der Zustandserfassung und Bewertung (ZEB) ermöglicht hat. Für die Durchführung der SKM Messungen danke ich dem Aalener Baustoffprüfinstitut. Die RoadSTAR Messungen konnten nur durch den großen Einsatz des Teams des Austrian Institute of Technology (AIT) und die Betreuung durch das Forschungsinstitut für Kraftfahrwesen und Fahrzeugmotoren Stuttgart (FKFS) durchgeführt werden.

Zu guter letzt möchte ich mich auch meiner Familie für die Unterstützung während meines gesamten Studiums und der Promotionszeit danken.

Böblingen, Februar 2021 Thorsten Lajewski

Contents

Abbreviations VIII

Symbols X

Abstract XVI

Kurzfassung XVIII

1 Introduction 1
- 1.1 Motivation . . . 2
- 1.2 State of the Art . . . 11
  - 1.2.1 Friction Potential Measurement Methods . . . 11
  - 1.2.2 Friction Potential Estimation Methods . . . 23
- 1.3 Objectives . . . 33
- 1.4 Outline . . . 34

2 Fundamentals of Tyre Friction and its Effect in Tyre Models 36
- 2.1 Important Influencing Factors . . . 36
  - 2.1.1 Road Surface . . . 37
  - 2.1.2 Tyre . . . 39
  - 2.1.3 Intermediate Layer . . . 46
  - 2.1.4 Vehicle . . . 50
- 2.2 Tyre Models . . . 50

3 Development of a Friction Potential Measurement Method 55
- 3.1 Test Vehicle . . . 55
- 3.2 Measurement Method - Single Wheel Braking . . . 57
  - 3.2.1 Safety Considerations . . . 58
  - 3.2.2 Measurement Data Processing . . . 61
  - 3.2.3 Comparison with Full Braking Measurements . . . 67
- 3.3 Measurements on Public Roads . . . 70
  - 3.3.1 Variation of Measured Friction Potential Values . . . 71

3.3.2 Influence of the Road Surface . . . 74
3.3.3 Influence of the Road Condition . . . 75
3.3.4 Influence of the Surface Temperature . . . 77
3.3.5 Influence of the Velocity . . . 78

4 Grip Map 81
4.1 SKM Measurements . . . 83
4.1.1 Test Track . . . 83
4.1.2 Public Road . . . 87
4.1.3 Comparison with Single Wheel Braking . . . 90
4.2 RoadSTAR Measurements . . . 92
4.2.1 Test Track . . . 93
4.2.2 Public Road . . . 97
4.2.3 Comparison with Single Wheel Braking . . . 101

5 Intermediate Layer Classification 104
5.1 Input Sources . . . 104
5.1.1 Road Weather Information System . . . 105
5.1.2 Radar . . . 106
5.1.3 Vehicle Data . . . 106
5.2 Ground Truth . . . 107
5.3 Classification methods . . . 110
5.3.1 Established Intermediate Layer Classification Methods . . . 111
5.3.2 Application of Classification Methods . . . 117
5.4 Comparison of Classification Results . . . 125

6 Remaining Risk of Overestimating the Friction Potential 127
6.1 Friction Requirements for Normal Driving . . . 127
6.2 Risk Estimation . . . 131

7 Conclusions 136

Appendix 139

A Vehicle Model 139

B Vehicle Measurements 142
B.1 Friction Measurements on FAT track . . . 142
B.2 Hydroplaning Example . . . 142

B.3 Measurements on Snow/Ice 145

C Continuous Friction Potential Measurements **147**

Bibliography **155**

Abbreviations

Abbreviation	Description
ABS	Anti-lock Braking System
AD	Autonomous Driving
ADAS	Advanced Driving Assistance System
ADC	Analogue Digital Converter
AIT	Austrian Institute of Technology
ANN	Artificial Neural Network
ASCII	American Standard Code for Information Interchange
AV	Autonomous Vehicle
BASt	Bundesanstalt für Straßenwesen
BPN	British Pendulum Number
BUFR	Binary Universal Form for the Representation of meteorological data
CAN	Controller Area Network
DWD	Deutscher Wetterdienst
EFI	European Friction Index
ESC	Electronic Stability Control
FAT	Forschungsvereinigung Automobiltechnik
FKFS	Forschungsinstitut für Kraftfahrwesen und Fahrzeugmotoren Stuttgart
GIDAS	German In-Depth Accident Study
GNSS	Global Navigation Satellite System
GPS	Global Positioning System
IFI	International Friction Index
LQR	Linear Quadratic Regulator
MASS	Mean Acceleration to Standstill
MFDD	Mean Fully Developed Deceleration
MLR	Multinomial Logistic Regression

Abbreviation	Description
MPD	Mean Profile Depth
MTD	Mean Texture Depth
PBFC	Peak Brake Force Coefficient
RWIS	Road Weather Information System
SAE	Society of Automotive Engineers
SCRIM	Sideway-force Coefficient Routine Investigation Machine
SKM	Seitenkraftmessverfahren
SRM	Stuttgarter Reibwertmesser
SRTT	Standard Reference Test Tyre
SWB	Single Wheel Braking
UNECE	United Nations Economic Commission for Europe
XBS	Extended Brake Stiffness

Symbols

Roman

Symbol	Description	Unit
A	Area of Contact Patch	m^2
ABS	Flag to Include ABS Operation in Friction Potential Estimation	
A_{ifi}	IFI Friction Device Parameter A	
B_{ifi}	IFI Friction Device Parameter B	
B_{MF}	Magic Formula Parameter B	
C	Height Correlation Function	m^3
C_1	WLF Equation Emperical Constant C_1	
C_2	WLF Equation Emperical Constant C_2	
C_{ifi}	IFI Friction Device Parameter C	
C_{MF}	Magic Formula Parameter C	
D	Set of Observations	
D_f	Fractal Dimension	
D_{MF}	Magic Formula Parameter D	
E	Young's Modulus	Pa
EIML	Estimated Intermediate Layer Class	
E_{MF}	Magic Formula Parameter E	
E'	Storage Modulus	Pa
E''	Loss Modulus	Pa
E^*	Loss Modulus	Pa
F_{30}	European Friction Index	
F_{60}	International Friction Index	
F	Input/ Feature	
$\mathbf{F}$	Input/ Feature Vector	
F_{adh}	Adhesion Component of Tyre Force	N
$F_{cohesion}$	Cohesion Component of Tyre Force	N

F_h	Horizontal Force acting in the X-Y-Plane	N
F_{hyst}	Hysteresis Component of Tyre Force	N
F_L	Lift Force	N
F_{vis}	Viscous Component of Tyre Force	N
F_x	Longitudinal Force	N
F_y	Lateral Force	N
F_z	Vertical Force	N
G	Shear Modulus	Pa
G	Ratio of Deceleration of Tested Tyre compared to Reference Tyre	
G_w	Weighting Function	
I	Number of Inputs	
IML	Intermediate Layer Class	
I_{yy}	Rotational Inertia of the Wheel	$kg\,m^2$
I_{zz}	Yaw Inertia	N m
K	Scaling Parameter K	
L	Length of Tyre Contact Patch	m
L_D	Diameter of Contact Area	m
M	Number of Features	
M_{brk}	Brake Torque	N m
M_z	Yaw Moment	N m
N	Number of Measurements / Observations	
O	Class	
P	Probability	%
R	Corner Radius	m
S	Number of Segments	
SD	Spin-down of Free Rolling Tyre Due to (Partial) Aquaplaning	%
S_p	IFI Corrected Surface Texture	
T	Temperature	K
TD	Thread Depth of the Tyre	mm
T_g	Glass Transition Temperature	T_g
TXD	Texture Depth of the Road Surface	mm
Tyre	Correlation Parameter for the Tyre Performance	
U	Number of Classes	
V	Viewing Distance	m

W	Width of Tyre Contact Patch	m
WD	Water Depth on the Road	mm
X	Random Variable	
X	Position X in Global Coordinate System	m
Y	Random Variable	
Y	Position Y in Global Coordinate System	m
a	Real Part of Complex Number	
a	Acceleration	$m\,s^{-2}$
a_{3s}	Mean Deceleration in the Three Seconds Interval starting from ABS Control Start	$m\,s^{-2}$
a_{mass}	Mean Deceleration in the Interval between ABS Control Start and Standstill	$m\,s^{-2}$
a_{mean}	Mean Deceleration in the Interval between Brake Pedal Application and Standstill	$m\,s^{-2}$
a_{mffd}	Mean Fully Developed Deceleration in the Interval between Brake Pedal Application and Standstill	$m\,s^{-2}$
a_x	Longitudinal Acceleration of Vehicle in Body Coordinate System	$m\,s^{-2}$
a_y	Lateral Acceleration of Vehicle in Body Coordinate System	$m\,s^{-2}$
a_{FAT}	Parameter a of Decision Function used in FAT Project	
a_{ifi}	IFI Surface Measurement Device Parameter a	
a_T	WLF Equation Superposition Parameter	
b	Imaginary Part of Complex Number	
b_{FAT}	Parameter b of Decision function used in FAT Project	
b_{ifi}	IFI Surface Measurement Device Parameter b	
c_{FAT}	Parameter c of Decision Function used in FAT Project	
c_κ	Longitudinal Slip Stiffness	
c_L	Lift Coefficient	
c_{rot}	Rotational Spring Stiffness	$N\,rad^{-1}$
dT	Evaluation Interval Length	s
f	Decision Function	
fl	Front Left Tyre	

fr	Front Right Tyre	
g	Gravitational Constant $9.81\,\mathrm{m\,s^{-2}}$	g
h	Height of Road Asperities	m
h_{cog}	Height of Center of Gravity over Ground	m
i	Feature Index	
i	Measurement Index	
j	Segment Index	
k	Brush Stiffness	$\mathrm{N\,m^{-1}}$
k_s	Factor Accounting for the Role Stiffness Distribution between Front and Rear Axle	
l	Weight Based on Correct Class	
l_{wb}	Wheel Base	m
l_f	Distance Center of Gravity to Front Axle	m
l_r	Distance Center of Gravity to Rear Axle	m
m	Vehicle Mass	kg
o	Correct Class for Training	
$\mathbf{o}$	Set of Correct Classes used for Training	
p_i	Internal Tyre Pressure	Pa
$\mathbf{q}$	Wave Vector	$1/\mathrm{m}$
r	Absolute Value of Complex Number	
r_0	Unloaded Tyre Radius	m
r_e	Effective Tyre Radius	
rl	Rear Left Tyre	
r_L	Loaded Tyre Radius	m
rr	Rear Right Tyre	
r_{xy}	Pearson Correlation Coefficient	
r	Yaw Velocity	$\mathrm{rad\,s^{-1}}$
s	Driven Distance	m
sig	Sigmoid Function	
s_N	Standard Deviation	
t	Time	s
t_f	Track Width Front	m
t_r	Track Width Rear	m
u	Weight based on Correct Class and Estimated Class	
v	Velocity	$\mathrm{m\,s^{-1}}$
v_{safe}	Safe Driving Velocity of the vehicle	$\mathrm{m\,s^{-1}}$

v_{crit}	Critical Aquaplaning Velocity	$m\,s^{-1}$
$\tilde{v}$	Velocity	kph
v_0	Start Velocity of Braking Test	$m\,s^{-1}$
v_x	Longitudinal Velocity of Vehicle in Body Coordinate System	$m\,s^{-1}$
v_y	Lateral Velocity of Vehicle in Body Coordinate System	$m\,s^{-1}$
w	Weight	
$\boldsymbol{w}$	Weight Vector	
x	Outcome of Random Variable X	
x_{in}	Input of a Neuron	
y	Outcome of Random Variable Y	
z	Output of a Neuron	
z	Complex Number	

Greek

Symbol	Description	Unit
E	Error	
Ω	Heading Angle	$^\circ$
Φ	Log Odds	
α	Lateral Slip	rad
χ	Value of Road Friction Potential Measurement	
δ	Phase Angle	rad
δ_W	Front Wheel Steering Angle	$^\circ$
ϵ	Strain	
η	Dynamic Viscosity	Pa s
η_D	Parameter of a Probability Distribution D	
κ	Longitudinal Slip	
κ_e	Ordinate of Slip-force Curve	
λ	Length of Road Asperities	m
μ	Friction	
μ_{pot}	Friction Potential	
$\mu_{Roadstar}$	Friction Potential measured by the RoadSTAR Truck	
ν	Poisson's Ratio	
$\dot{\omega}$	Rotational Acceleration of the Wheel	$rad\,s^{-2}$

ω_f	Angular Frequency	Hz
ω	Wheel Rotational Velocity	$\mathrm{rad\,s^{-1}}$
ϕ	Sliding Direction	rad
ψ	Twist Angle of the Suspension	rad
ρ	Density	$\mathrm{kg\,m^{-3}}$
σ	Stress	Pa
ζ	Zoom Factor	

Abstract

The friction potential is a unitless parameter of the maximal longitudinal and lateral forces transferable between vehicle and road normalized by the tyre contact forces. Exact knowledge of this parameter can improve advanced driver assistance systems. Autonomous vehicles require information about the friction potential for route and trajectory planning. Based on the friction potential the planned velocity has to be adopted in a way that the trajectory can be followed and that the stopping distance is inside the visible range of the vehicle sensors.

In order to meet these requirements, continuously available friction potential information must be provided. This requires knowledge of the friction potential with a preview of more than 100 m. Instead of estimating the exact friction potential, it is sufficient to be able to guarantee a lower boundary.

Due to the wide range of possible applications of the friction potential, many methods for estimating the friction potential have already been researched. These can be divided into two main categories: effect-based methods and cause-based methods. Effect-based methods estimate the friction potential on the basis of the driving dynamics variables measured in the vehicle. Cause-based methods use vehicle sensors and/or Car2x data to try to determine parameters that influence the friction potential, and from this information defer changes of the friction potential. Only cause-based methods can determine the friction potential with a sufficient preview. Therefore, in this thesis, modules of a cause-based method were evaluated.

The basis for the evaluation of each friction potential estimation method is the measurement of the real friction potential. This is typically determined by full braking tests. Since these tests can only be carried out on test tracks, a new method has been developed which brakes only one wheel for a short time until ABS control is activated. This method was used to perform repeated friction potential measurements at 74 defined points along public roads over a period of 6 months. Based on this data, the main influencing factors intermediate layer and road surface were confirmed as expected. Furthermore, differences between sets of tyres, even of the same type, were shown. These were attributed to wear and thus excluded in the evaluation. No other influences known from literature, such as a change in the friction potential with the season or a speed dependence, were found. An influence of the road temperature on the friction potential could not be excluded, but the influence differs greatly depending on the braking point, so that this dependence was included in the measurement uncertainty.

In order to analyze the influence of the road surface, the friction potential meas-

urement methods Seitenkraftmessverfahren (SKM) and RoadSTAR, which are used in road maintenance, were compared with the created database. The results of the Seitenkraftmessverfahren show no correlation with the friction potential measurements conducted by the test vehicle. The RoadSTAR results, however, show a clear correlation. Adjustments of the RoadSTAR truck to further improve this correlation have failed due to limitations of the measurement technology used.

The intermediate layer between tyre and road was estimated using external data from road weather station, rain radar and from the test vehicle using various machine learning methods. It was shown that the correct intermediate layer can be classified more than 90 % of the time. The classification of potential aquaplaning conditions and the influence of winter services on the intermediate layer proved to be problematic.

A final evaluation shows that using road information determined by RoadSTAR and an intermediate layer estimation by external data and machine learning, a residual risk of exceeding the friction potential of 1.9 % remains. 1.5 % of this remaining risk is due to the misclassification of the intermediate layer ice/snow.

In the future, further improvements could be achieved by adapting the working conditions of the RoadSTAR truck's measurement tyre to those of a passenger car tyre during ABS braking. A significant improvement of the intermediate layer classification seems only possible by using ploughing and gridding information of the winter service provider. Furthermore, the detection of potential aquaplaning conditions must be improved. The overall methodology can be improved by including further estimation methods and sensors.

Kurzfassung

Das Reibwertpotential beschreibt als einheitenlose Kenngröße die auf die Reifenaufstandskräfte normierten maximalen Längs- und Querkräfte zwischen Fahrzeug und Fahrbahn. Eine genaue Kenntnis des Reibwertpotentials kann viele Fahrassistenzsysteme verbessern. Autonome Fahrzeuge benötigen diese Größe zur Routen- und Trajektorienplanung. Sie wird verwendet, um die Geschwindigkeit anpassen zu können, sodass jederzeit der geplanten Trajektorie gefolgt werden kann und der Anhalteweg kleiner als die aktuelle Sichtweite ist. Um diese Anforderungen zu erfüllen, muss eine kontinuierlich verfügbare Information über das Reibwertpotential bereitgestellt werden. Dafür ist Wissen über das Reibwertpotential mit einer Vorschau von mehr als 100 m notwendig. Anstatt das genaue Reibwertpotential zu schätzen, ist es hierbei jedoch ausreichend, eine untere Schranke garantieren zu können.

Aufgrund der weiten Einsatzmöglichkeiten des Reibwertpotentials wurden bereits viele Verfahren zur Reibwertpotentialschätzung erforscht. Diese lassen sich in zwei Hauptkategorien einteilen: effektbezogene Methoden und ursachenbezogene Methoden. Effektbezogene Methoden schätzen das Reibwertpotential auf Basis der im Fahrzeug gemessenen Fahrdynamikgrößen. Ursachenbezogene Methoden hingegen versuchen das Reibwertpotential über Fahrzeugsensorik und / oder Car2x-Daten Parameter, die das Reibwertpotential beeinflussen, zu bestimmen und daraus auf Änderungen des Reibwertpotentials zu schließen. Nur diese Methoden können das Reibwertpotential mit einer ausreichenden Vorschau bestimmen. Daher wurden in dieser Arbeit Bausteine einer ursachenbezogenen Methode bewertet.

Gundlage für die Bewertung jeder Reibwertpotentialschätzmethode ist die Messung des realen Reibwertpotentials. Dieser wird typischerweise durch Vollbremsungen ermittelt. Da Vollbremsungen nur auf Testgeländen durchgeführt werden können, wurde eine neue Methode entwickelt, die nur ein Rad kurze Zeit bis in die ABS-Regelung bremst. Mit dieser Methode wurden über ein halbes Jahr hinweg wiederholte Reibwertbremsungen an 74 definierten Punkten entlang öffentlicher Straßen durchgeführt. Auf Basis dieser Daten wurden die erwarteten Haupteinflussfaktoren Zwischenschicht und Straßenoberfläche bestätigt. Zudem wurden Unterschiede zwischen Reifensätzen, sogar des gleichen Typs, gezeigt. Diese wurden auf Verschleiß zurückgeführt und für die weitere Bewertung nicht betrachtet. Keine weiteren in der Literatur gefundene Einflüsse, wie eine Veränderung des Reibwertpotentials mit der Jahreszeit oder eine Geschwindigkeitsabhängigkeit, wurden gefunden. Ein Einfluss der Straßentemperatur auf das Reibwertpotential konnte nicht ausgeschlossen werden, aber der Einfluss unterscheidet sich je nach Bremspunkt stark, daher wurde diese Abhängigkeit mit in die

Messunsicherheit aufgenommen.

Um den Einfluss der Straßenoberfläche zu analysieren, wurden die im Straßenbau verwendeten Reibwertpotentialbewertungsverfahren Seitenkraftmessverfahren (SKM) und RoadSTAR mit der erstellten Datenbasis verglichen. Die Ergebnisse des Seitenkraftmessverfahrens zeigen keine Korrelation mit den durch das Testfahrzeug bestimmten Reibwertpotentialmessungen. Die RoadSTAR-Ergebnisse hingegen zeigen einen deutlichen Zusammenhang. Anpassungen des RoadSTAR-LKW zur weiteren Verbesserung dieser Korrelation sind auf Grund von Limitierungen der verwendeten Messtechnik gescheitert.

Die Zwischenschicht zwischen Reifen und Straße wurde mit Hilfe von externen Daten aus Straßenwetterstation, Regenradar und aus dem Testfahrzeug mithilfe verschiedener Machine-Learning-Methoden geschätzt. Es wurde gezeigt, dass die richtige Zwischenschicht über 90 % der Zeit sicher eingeschätzt werden konnte. Problematisch erwies sich hierbei das Klassifizieren von potentiellen Aquaplaningbedingungen und die Beeinflussung der Zwischenschicht durch Winterdienste.

Eine abschließende Bewertung zeigt, dass unter Verwendung von Straßeninformationen ermittelt durch RoadSTAR und einer Zwischenschichtschätzung durch externe Daten und Machine-Learning ein Restrisiko einer Reibwertpotentialüberschreitung von 1.9 % bestehen bleibt. Davon entfallen 1.5 % auf das Fehlklassifizieren der Zwischenschicht Eis/ Schnee.

In Zukunft könnten weitere Verbesserungen erzielt werden, in dem die Arbeitsbedingungen des Messreifens des RoadSTAR-LKW an die eines PKW-Reifens während einer ABS-Bremsung angepasst werden. Eine deutliche Verbesserung der Zwischenschichtprognose scheint nur unter Verwendung von Streu- und Räumungsdaten des Winterdienstes möglich. Außerdem muss die Erkennung von potentiellen Aquaplaningbedingungen verbessert werden. Die Gesamtmethodik kann verbessert werden durch das Einbeziehen weiterer Schätzverfahren und Sensoren.

1 Introduction

Since its invention in 1886, the car has become the most used and most comfortable means of transport. According to Bundesanstalt für Straßenwesen (BASt)[1] [1], approximately 490 billion kilometers were traveled by privately owned vehicles in 2014 in Germany alone. This highlights the importance of individual transport solutions. The large amount of vehicles used poses several challenges, which autonomous driving can improve upon. Three of the most important aspects are

- safety,
- congestion, especially in densely populated areas, and
- costs of transportation.

Safety Worldwide, ambitious targets aim to reduce the number of accidents. One of these programs is 'Vision Zero' [2], which ultimately envisions to reduce the number of injuries and fatalities due to crashes to zero. Today, according to [3], 94 % of all crashes are caused by human errors.

The further development of Advanced Driving Assistance System (ADAS) and ultimately autonomous driving is one of the building blocks of Vision Zero. In the past, several of these systems have already proven to increase safety. The first introduced systems were Anti-lock Braking System (ABS) and its extension Electronic Stability Control (ESC). These systems support the driver to keep the vehicle steerable in emergency situations in which the maximal possible forces between an individual tyre and the road are exhausted. Lane keeping systems warn the driver if the vehicle crosses the lane markings and active systems can steer the vehicle back into the lane automatically. Similarly, collision warning systems can warn the driver of obstacles ahead of the vehicle and initiate emergency braking, reducing the impact energy or in the best case even preventing it altogether. Autonomous functions can help reduce certain accident types. Today, a very common cause for accidents is driver inattention. According to data collected in a 100 car naturalistic driving study, driver inattention contributed to

[1] Federal Highway Research Institute, Germany

73 % of the recorded crashes and 65 % of the near crashes [4]. A fully autonomous system is always attentive and thus reduces this error cause. The challenge of introducing more automation is that these systems introduce no new accident causes and are indeed safer than human drivers. One of the new tasks for autonomous systems is the correct reaction to changing driving environment conditions.

Congestion In cities, vehicles do not only require a large road infrastructure but also sufficient parking spaces. The search for parking spots increases the inner city traffic. According to [5], a driver in Germany wastes on average 41 h a year looking for parking. A fully autonomous vehicle does not need to find a parking spot but can drop off the passengers and drive to a designated parking area further away. If the autonomous vehicles are used in a shared transportation service, the inner city traffic can be reduced further. A simulation study conducted for Munich showed, that 18 000 autonomous electric vehicles would suffice to eliminate the need for 200 000 privately owned vehicles [6].

Costs An additional commercial impulse for the development of fully autonomous vehicles is the reduced need for human cab or lorry drivers, which can lead to reduced transportation costs. A huge benefit of autonomous vehicles is also that these systems are not bound to driving time limitations. Thus, they can have a better capacity utilisation. The removal of driving time limitations would also lead to operating times during night time, where road maintenance is reduced. Especially in winter, this can increase the importance of a friction potential estimation system.

1.1 Motivation

The Society of Automotive Engineers (SAE) International Standard J3016 [7] defines six levels of vehicle automation ranging from no automation to full automation. The definition of these levels is shown in figure 1.1. The first three of these levels (0-2) describe the different levels of ADAS as they are included in many cars today. Typical level 0 systems are ABS and ESC systems. Also automated emergency braking systems and lane keeping systems fit into this category. Level 1 systems take over either the longitudinal or the lateral vehicle control. Well-known ADAS of this category are cruise control systems. Level 2 systems combine lateral and longitudinal control. In this category, cruise control systems with steering assist and automated parking systems are available.

SAE level	Name	Narrative Definition	Execution of Steering and Acceleration/ Deceleration	*Monitoring* of Driving Environment	Fallback Performance of *Dynamic Driving Task*	System Capability *(Driving Modes)*
***Human driver* monitors the driving environment**						
0	No Automation	the full-time performance by the *human driver* of all aspects of the *dynamic driving task*, even when enhanced by warning or intervention systems	Human driver	Human driver	Human driver	n/a
1	Driver Assistance	the *driving mode*-specific execution by a driver assistance system of either steering or acceleration/deceleration using information about the driving environment and with the expectation that the *human driver* perform all remaining aspects of the *dynamic driving task*	Human driver and system	Human driver	Human driver	Some driving modes
2	Partial Automation	the *driving mode*-specific execution by one or more driver assistance systems of both steering and acceleration/ deceleration using information about the driving environment and with the expectation that the *human driver* perform all remaining aspects of the *dynamic driving task*	**System**	Human driver	Human driver	Some driving modes
***Automated driving system* ("system") monitors the driving environment**						
3	Conditional Automation	the *driving mode*-specific performance by an *automated driving system* of all aspects of the dynamic driving task with the expectation that the *human driver* will respond appropriately to a *request to intervene*	System	**System**	Human driver	Some driving modes
4	High Automation	the *driving mode*-specific performance by an automated driving system of all aspects of the *dynamic driving task*, even if a *human driver* does not respond appropriately to a *request to intervene*	System	System	**System**	Some driving modes
5	Full Automation	the full-time performance by an *automated driving system* of all aspects of the *dynamic driving task* under all roadway and environmental conditions that can be managed by a *human driver*	System	System	System	**All driving modes**

Figure 1.1: SAE levels of vehicle automation [7]

Starting with level 3, the systems are classified as automated driving systems. The distinction between the first three levels and the second three levels is that automated driving systems fulfil the task of monitoring the driving environment. Thus, while in level 0 to 2 systems, the driver is required to be concentrated on the road, starting with level 3, the driver can safely engage in secondary tasks in some driving situations. The difference between the three automated driving levels is the availability of the system and the handling of system faults. In level 3 and 4 systems, the automated driving function is only available in certain driving modes, for example only on highways. In level 3 systems, in case of a system fault, the human driver has to take over the dynamic driving task. In contrast to this behavior, level 4 systems must be able to safely stop the vehicle at the side of the road if the driver does not take over the driving task. Level 5 systems remove the limitation of only allowing the autonomous driving function in special driving scenarios and require the vehicle to operate in all conditions a human is able to drive.

The property road friction potential, which defines the possible vehicle accelerations, can be one of the decision factors to switch the Autonomous Driving (AD) function off

or on. In level 3 or 4, AD functions driving on slippery road surfaces might be excluded from the allowed driving modes, since these conditions increase the accident risk. If these slippery road conditions are excluded from the allowed driving modes, the AD system has to be able to detect these conditions. Since the level 3 or 4 system has to provide the driver with sufficient take over time or safely stop the vehicle before the slippery road surface is reached, this detection has to include a sufficient preview distance. Similarly, level 5 AD systems have to adapt their driving style, primary the velocity, before the slippery road is reached.

Autonomous driving requires the vehicle to supervise and interpret the entire environment around the vehicle correctly. This includes applying the traffic rules, tracking all other road users and planning a safe path through the available space. Planning this trajectory includes choosing an adequate velocity. This velocity depends on traffic rules, the view distance, which is determined by sensor ranges, the geometry of the environment and the possible vehicle accelerations. The accelerations mainly depend on the friction potential.

Friction μ is the transferred force in horizontal direction F_h normalized by the vertical force, while friction potential μ_{pot} is the normalized maximal transferable force. These forces are generated by a relative movement between the tyre rubber and the road surface. This relative movement is often represented by a variable called slip, which can be applied in longitudinal (κ) and lateral direction (α). Thus, the longitudinal force transmitted by a tyre is $F_x(\kappa)$ and the lateral force is $F_y(\alpha)$. Both functions normally cannot be used independently of each other. The combined maximal longitudinal and lateral forces are often approximated by an ellipse, the friction ellipse [8]. This ellipse symbolises the friction potential.

Depending on the application, the friction potential can be defined and measured differently. Two definitions are common, both are visualised in figure 1.2, while the distinction between both methods is not always explicitly done. The left part of the figure visualises the tyre perspective. The friction potential is defined by the forces acting on an individual tyre. At a certain slip condition, the forces created by the tyre are maximal. This point defines the friction potential. The friction potential can be calculated by equation 1.1. During normal driving situations, this point of the tyre force curve is never reached. In case of an emergency braking event, the ABS controls the tyre slip around this optimum point. This friction potential value is also known as peak brake force coefficient.

The right side of the figure shows the measured acceleration during a full braking test to standstill. This is a typical measurement manoeuvre for the friction potential. The maximal acceleration a does not only depend on all tyres of the vehicle but also

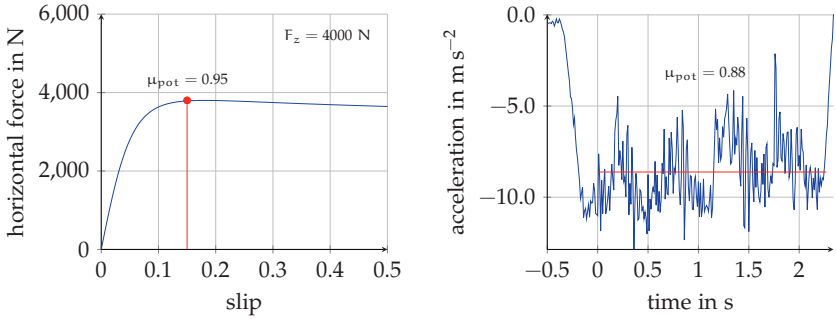

Figure 1.2: Definition of the friction potential μ_{pot}; left: tyre perspective; right: vehicle perspective

on the performance of the ABS controller and other vehicle properties like for example the load transfer during braking. In this case, the friction potential can be calculated by averaging the measured acceleration a during the full braking event and normalizing it by the gravitational constant g like shown in equation 1.2. The friction potential calculated this way will differ from the tyre perspective and shall be called vehicle perspective from now on.

$$\mu_{pot} = \max\left(\frac{F_h}{F_z}\right) = \max\left(\frac{\sqrt{{F_x}^2 + {F_y}^2}}{F_z}\right) \tag{1.1}$$

$$\mu_{pot} = \frac{|\bar{a}|}{g} \tag{1.2}$$

The friction potential is influenced by the complex interaction between several tyre and road properties. In many cases an intermediate layer, often due to water but also other contamination, plays an important role in the generation of friction and thus the friction potential.

A starting point to analyse the friction potential topic and derive requirements for an Autonomous Vehicle (AV) is to know the typically available friction potential. One extensive study to measure the friction potential on public roads has been conducted in [9]. Short full braking tests of about 0.5 s were repeatedly conducted on 32 points on public roads during a period of three years. These measurements generated a database consisting of over 4000 measurements. The results of these measurements are shown in figure 1.3. Clear differences in the measured friction potential of the

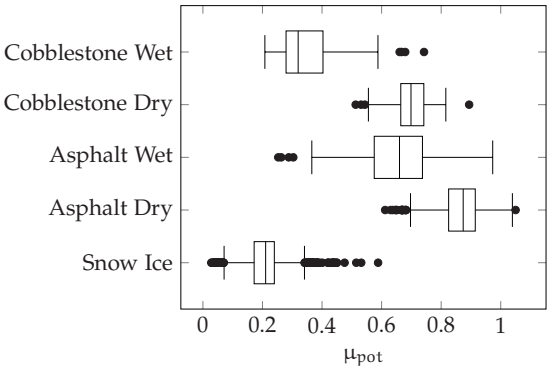

Figure 1.3: Published friction potential values of different road surface/road condition categories based on the data of [9]; box: lower quartile, median, upper quartile; whiskers: first data point inside 1.5 times the interquartile range (upper quartile - lower quartile)

different categories can be seen. The large spread in the measured friction potential indicates that other properties not resolved by the categorisation influence the friction potential.

The median friction potential value of measurements on dry asphalt is around 0.9. On wet asphalt a reduction in the friction potential is clearly visible. The median friction potential of this category is around 0.65. Especially, the spread of this category is very large including a few measurements with values as low as 0.2 and as high as 0.95. In case of a snow or ice surface, the friction potential drops to values between 0.05 and 0.35. The boxplot shows many outliers in the direction of higher friction potential values. These can be explained by measurements on thin snow/ice layers where the tyre can partly interact with the road surface and thus transmits larger forces. The reduction of the friction potential between the asphalt and the cobblestone surfaces shows that the surface properties of the road also have a significant influence on the measured friction potential.

In other literature, friction potential values in the range of 0.75 and 1.02 are given for dry roads. For wet roads, values between 0.6 and 0.9 are published [10]. These friction potential values confirm a similar friction potential range as the Forschungsvereinigung Automobiltechnik (FAT) project measured for the asphalt surfaces.

The differences in the available friction potential are also visible in accident studies. Accidents caused by a wrong friction potential assumption appear in accident studies and were explicitly examined in two different evaluations in [9]. The two different Ger-

man In-Depth Accident Study (GIDAS)[2] studies were conducted to analyse accidents on surfaces with a low friction potential. In the first study, accidents caused by unpredictable low friction potential events were compared with accidents on dry roads. The definition of unpredictable low friction potential used in this study was based on two requirements. First, the causes of the accidents had to be aquaplaning, ice or black ice. Secondly, the road condition changed suddenly, so that the driver was unable to react to that change. Of over 27 200 accidents with damage to persons in the database, only 129 have been caused by unpredictable low friction potential. These are only 0.5 % of all accidents. 78.1 % of these accidents took place on ice, while 14.5 % were caused by aquaplaning. The rest of these accidents were caused by hail or snow banks. Since the study is limited to accidents caused by unpredictable low friction potential, the study shows that over 70 % of the accidents in this category happened during periods without precipitation at that time.

In the second study, all accidents related to a friction potential reduction below 60 % of a nominal friction potential have been included. 981 of 29 500 accidents fall into this group. These are about 3.3 % of the included accidents. It has to be noted that low friction potential is not the cause of all these accidents but only a contributing factor. Over 50 % of the accidents took place during no precipitation, 23.8 % during rain and 18 % during snowfall.

According to the Statistisches Bundesamt[3], 13 936 of 302 656 accidents with damage to persons due to slippery road conditions were registered in Germany [11] in 2017. These are 4.4 % of all accidents with injured persons. In additional 4.1 % of accidents, reduced friction potential due to rain or ice contributed to accidents. The summed value of 8.5 % of accidents, in which a friction potential reduction contributed to the accident is significantly higher than the 3.3 % of accidents related to reduced friction potential in the GIDAS study. This could have several reasons. Either the size of the data base of GIDAS is not large enough or the included regions do not represent the climate across all of Germany well enough. Another possible reason is that friction potential related accidents may also happen when the friction potential is reduced to values above 60 % of the set nominal value or the conditions to classify an accident as caused by low friction potential are different.

In the published data, snow and ice caused 6103 accidents, while rain caused 6387 crashes. In Germany, rain and wet roads are far more common than snow or ice on the road. The similar accident number in each road condition indicates that snow and

[2] A Database containing reconstructed accidents with damage to persons from the areas Dresden and Hannover

[3] Federal Statistical Office, Germany

ice is significantly more dangerous than wet roads. This is an expected result of the published friction potential values in these road conditions but also indicates that a safe adoption of the driving style is often disregared by the driver or not possible, because the low friction potential was not detectable in time.

Two additional causes of accidents releated to the friction potential, not yet discussed, were road contamination and the road itself. 749 accidents are caused by natural contamination of the road like leaves or mud. 475 accidents are caused by spilled oil. Another 222 are attributed to contamination caused by other road users. Furthermore, 121 accidents originated by a combination of lane groves and rain or snow [11]. Lane groves increase the water height on the roads and thus can lead to dangerous aquaplaning situations.

An autonomous vehicle without any friction potential information cannot adapt its driving style and is at a higher risk of exceeding the available physical limits than a human driver. While many of the weather related accidents could be avoided by overall defensive driving, an increased risk of planning trajectories that cannot be followed remains. Weather conditions like rain and snow/ice mainly contribute to the accident statistics but dirt and overall poor road quality seem to have additional influence. Friction potential related accidents on a clean and dry road do not appear in the accident studies. It can be concluded that under these conditions the friction potential is sufficient.

Knowledge about the friction potential has been identified as beneficial for many ADAS applications. These applications include for example warning the driver about low friction potential values, setting the correct brake pressure at the start of an ABS intervention or initiating an emergency brake or evasion manoeuvre at the correct time. All these systems have different accuracy and availability requirements for the friction potential estimation.

In the driver warning case, on the one hand, a missed warning about a low friction potential might not lead to any problems since the driver should drive according to the environmental conditions anyway. On the other hand, regular unnecessary warnings will annoy the driver and he will likely ignore these warnings in the future and the benefits of the friction potential warnings are lost. In terms of accuracy, only a limited number of warning levels are required.

On the other end of the requirements scale, in order to improve the ABS performance, very accurate information about the friction potential is required. The potential of reducing the braking distance is discussed in [12].

In case of an excessive friction potential estimation, benefits of the system are lost but a too low friction potential estimation might degrade the performance of the initial

control cycles and of the ABS. If no information about the friction potential is available, a high assumption of the friction potential will lead to the performance of a standard ABS.

Requirements for ADAS to decide if an evasive manoeuvre or an emergency brake should be initiated are derived in [13]. The short time window to decide, which manoeuvre to use depends on the velocity and the friction potential. Therefore, very accurate information about the friction potential has to be available. Depending on the velocity and friction potential, the order of the point to start an emergency braking manoeuvre or an evasion manoeuvre can change. A wrong estimation can lead to the wrong decision and thus can lead to an accident, which could have been prevented.

The requirements for autonomous driving differ from the previously discussed use-cases, where a friction potential estimation for autonomous driving has to be used in a way to prevent emergency situations which require utilisation of a high percentage of the available friction potential. These situations can be minimised by accounting for the available friction potential on two planning levels, the route planning and the trajectory planning.

Route Planning

In the route planning stage, routes with expected low friction potential, e.g. steel bridge with ice risk, wet tram lanes or old cobblestone, can be excluded from the planned route or the AD functionality could be disabled altogether. Depending on the length of the route, this requires a large preview in time and position, but the accuracy requirements are not that high. A differentiation in potentially slippery and high friction potential should be sufficient at this stage. Although, if there are several possible routes, a further distinction between available friction potential levels can help choosing the safest one.

Trajectory Planning

Once the autonomous vehicle is driving, it has to consider the available friction potential in the planning process of its trajectory. The main controllable variable is the vehicle speed. When cornering without any velocity change, there is a physical relation between the required friction potential and vehicle velocity. A safe driving velocity v_{safe} for driving a corner with radius R can be calculated by equation 1.3.

$$v_{safe} < \sqrt{\mu_{pot} R g} \tag{1.3}$$

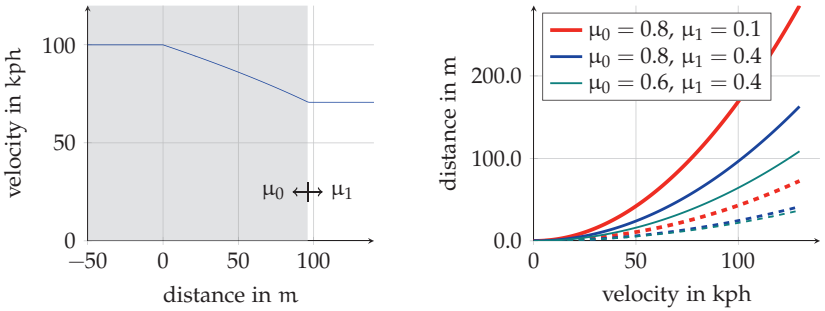

Figure 1.4: Trajectory planning preview requirements; left: comfortable velocity adaption ($a = -2\,m\,s^{-2}$), when detecting a friction potential change from $\mu_0 = 0.8$ to $\mu_1 = 0.4$ with sufficient preview; right: preview requirements for different friction potential changes, lines comfort ($a = -2\,m\,s^{-2}$), dashed lines maximal deceleration ($a = \mu_0 g$)

In the longitudinal direction, there is no direct physical relation between the friction potential and the vehicle velocity. Driving in a straight line at constant speed requires only enough friction to overcome the rolling resistance and drag of the vehicle. Instead, the relationship between the velocity and the driving velocity is imposed by safety considerations and prescribed by law[4]. The driver (or AV) is required to be able to stop inside the viewing distance V or in small streets with oncoming traffic inside half of the viewing distance. A simplified relation between the velocity and the viewing distance is given by equation 1.4. It is assumed that the maximal possible deceleration can be reached instantaneously.

$$v_{safe} < \sqrt{2\mu_{pot} V g} \tag{1.4}$$

As can be seen from the inversion of this equation, the required preview depends on the maximal velocity of the vehicle. For a comfortable deceleration in case of a decreasing friction potential, a significantly lower friction value should be used for the velocity adaptation. Figure 1.4 left shows an examplary velocity profile for a vehicle fulfilling equation 1.4, when driving on a high friction potential surface ($\mu_{pot} = \mu_0 = 0.8$) with 100 kph and encountering a lower friction potential surface ($\mu_{pot} = \mu_1 = 0.4$) with sufficient preview. A comfortable deceleration of $2\,m\,s^{-2}$ is assumed. The right side of the figure shows the required preview distances for different friction potential changes plotted over the initial velocity. The line indicates the required preview for a

[4] In Germany StVO §3(1)

comfortable deceleration and the dashed line the minimal required preview using an emergency brake to reach the lower velocity in time.

It can be seen that planning with an overall lower friction potential assumption, the preview requirements can be reduced, because the maximal possible friction potential reduction decreases. A too conservative friction potential assumption may lead to a lower driving velocity and the AV might impede human drivers. It can be seen that for velocities around 100 kph, a friction potential estimation with a preview of more than 100 m is required. In many driving situations, increasing the sensor view distance can reduce the required friction potential for planning but this is not possible for driving situations, where the sensor range is blocked by the road geometry for example when driving over a hill top.

1.2 State of the Art

Konwledge about the real friction potential is important to validate the friction potential estimation methods. Therefore, first several friction potential measurement methods are described in this section. After this, the current state of the art of estimating the friction potential is described. Due to the importance of the friction potential for vehicle control and ADAS, a lot of research on this topic has been conducted up to date. Nevertheless, because of the complexity of the problem, no product, which fulfils the previously derived requirements for friction potential estimation, is available yet.

1.2.1 Friction Potential Measurement Methods

Many different methods to measure the friction potential have been developed. Since the tyre friction potential is affected both by the tyre and by the road surface, friction potential measurement methods have been developed in the context of tyre testing and road maintenance. The authors of [14] specify a number of criteria to evaluate different friction potential estimators. These require a reference friction potential measurement. Therefore, they also define allowed measurement methods. The proposed methods are the measurement of the longitudinal force during an ABS braking test, measuring the acceleration during an ABS braking test or using special tyre test trucks. The authors do not provide further detail like starting velocities or evaluation intervals.

Regulations

Different standards are established, which more accurately specify the measurement conditions. Nevertheless, they result in different friction potential values.

ISO 8439 [15] focuses on three different methods to measure the friction potential and defines two different surface friction potential values. All three proposed methods require a special truck or trailer, which allows to brake a wheel and measure the generated forces. The focus of the norm is the surface friction potential and not the tyre friction potential. Therefore, a Standard Reference Test Tyre (SRTT) is used for the methods. The specified testing speed is 65 kph. The two friction potentials evaluated are the Peak Brake Force Coefficient (PBFC), which measures the friction potential similar to the previously described tyre perspective and a friction potential value measured with a fully locked tyre. The friction potential defined by a fully locked wheel is lower than the peak brake force coefficient and not relevant for vehicles equipped with ABS.

The first method increases the brake force applied to the wheel slowly until the wheel locks. The largest brake force applied before the wheel is locked divided by the load is the friction potential. In the next proposed method, the slip of the wheel is set to the slip value at which the PBFC was reached. An iterative procedure is required to find this slip value. This method allows to continuously measure the friction potential over longer distances. In the last method, instead of using the optimal slip value, a fixed slip value is used. This method can be used to compare friction values of different surfaces, but does not measure the maximum. The norm also specifies requirements for an artificial wetting system if measurements on a wet surface are required.

Instead of using special measurement trailers and tyres, the United Nations Economic Commission for Europe (UNECE) Regulation 13a [16] specifies a method which can use the vehicle and tyres, of which the friction potential shall be measured. Nevertheless, modifications to the vehicle are required, since the method requires to brake a single axis. Tests are conducted from an initial velocity of 50 kph. The axle is braked, so that the wheels just do not lock. Then the time the vehicle requires to decelerate from 40 kph to 20 kph is used to calculate the reference friction potential.

UNECE No. 117 [17], which specifies the wet grip measurements used for the wet label classification, specifies another method to measure the friction potential. Full braking tests with a starting velocity of 85 kph are used. The friction potential is calculated based on the average deceleration between 80 kph and 20 kph. The ABS controller of the vehicle is allowed to be active during the braking tests. Instead of using full braking tests, the regulation also allows tests with a trailer.

Test Vehicle Friction Potential Measurements

In research, other evaluation intervals, which do not require a specified starting velocity, have been used. Similar to the UNECE No. 117, full braking tests are usually employed. Although this measurement method is universally accepted, the measurement setups and evaluated measures vary. This can lead to different results. The main differences arise from the starting speed of the full braking test and the evaluation interval.

An ABS braking manoeuvre can be split into three different phases. In the first phase, after the brake pedal is applied, it takes some time until the maximal brake pressure is build up. Additionally, due to the weight transfer, the ABS controller algorithm may require some time until the maximal possible deceleration is reached. In the next phase of the braking manoeuvre, an optimal deceleration is reached. As the vehicle approaches standstill, the performance of the ABS controller can deteriorate since the discrete wheel speed sensor inputs are insufficient for the controller. The time spent in the different phases depends not only on the vehicle and ABS application[5] but varies also with starting speed, vehicle centre of gravity, tyres and even road condition.

In [18], an optical velocity sensor and an accelerometer have been used to evaluate the braking distance. The resolution of the optical sensor proved insufficient to derive accurate values. The selected starting velocities during the tests were 40 kph, 60 kph, 80 kph and 100 kph. The evaluated interval called mean acceleration a_{mean} starts when the brake pedal is pressed and stops when the vehicle reaches standstill. When the pedal is pressed the start velocity $vel0$ of the brake test is measured. In order to calculate the deceleration the time t required to stop and the stopping distance s are required.

$$a_{mean} = \frac{2s}{t^2} - \frac{v_0}{t} \tag{1.5}$$

All aforementioned braking phases are included in the interval used to calculate the friction potential.

In addition, the measurement interval Mean Fully Developed Deceleration (MFDD) has been investigated. The acceleration a_{mffd} is calculated by averaging over the interval between 80 % of the starting velocity and 10 % of the starting velocity. This way, depending on the starting velocity a part of the pressure buildup, ABS controller learning phase and the low velocity phase are not included in the evaluated interval. Therefore, the calculated value of the MFDD is usually higher than the mean accelera-

[5] The ABS controller is a compromise between separability and maximal deceleration.

tion. The resulting interval is similar to the interval used in UNECE No. 17, which also excludes the initial phase of the full braking tests and the last phase of the full braking test. The author concluded that the MFDD interval is inappropriate to estimate the stopping distance.

$$a_{mffd} = \frac{0.8v_0 - 0.1v_0}{2(s(0.8v_0) - s(0.1v_0))} \tag{1.6}$$

In [19], the author uses the MFDD interval to calculate the stopping distances of different vehicles. During these measurements, the vehicles had been equipped with an optical velocity sensor and an external wheel tick sensor. The starting velocities of the braking tests have been varied between 80 kph, 100 kph and 130 kph.

All previously mentioned studies used proving grounds and closed roads. During the measurements reported in [9], a measurement interval of 0.5 s after the applied brake pressure surpassed 175 bar has been used to evaluate the friction potential. During the measurements, the brake pedal has been released after the 0.5 s interval. Instead of measuring the vehicle velocity as mentioned in the previous two reports, an acceleration sensor has been used. The interval was chosen, because these measurements were conducted on public roads, which did not allow full braking tests until standstill. For the same reason, the starting velocity was between 30 kph and 120 kph and chosen as the surrounding traffic permitted. The 0.5 s full braking test can still have a negative impact since other road users are not used to sudden strong accelerations. In a later evaluation of the data [20], the 0.5 s interval was moved to the end of the full brake test duration, which resulted in an average increase of 0.07 of the measured friction potential.

Figure 1.5 depicts the three different measurement intervals discussed in this section. The fourth depicted interval is used in this thesis and introduced in section 3.2.3.

It has been discovered that repeated full braking tests with the same tyre set on the same surface can lead to increasing friction potential measurement values [21]. This is especially the case when these tests are conducted with winter tyres. The reason for this is believed to be a more even pressure distribution in the contact area during braking due to wear of the tyre profiles. Therefore, the wear of the tyres has to be observed and the number of full braking tests conducted with the same tyre should be limited.

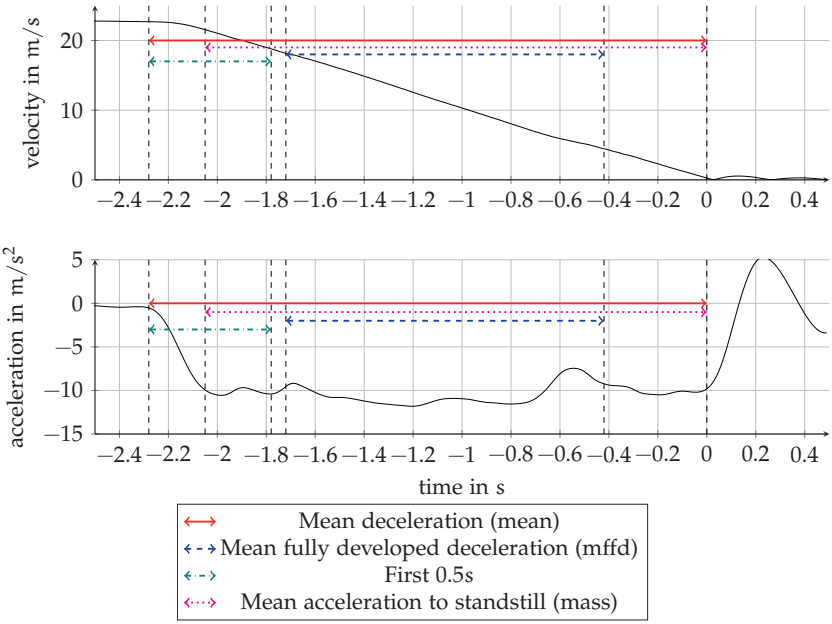

Figure 1.5: Evaluation intervals of full braking measurements found in literature and used in this thesis

Road Maintenance Friction Potential Measurement Methods

Road maintenance authorities use many different methods to measure the friction potential. Almost all countries have their own regulations and measurement systems. The focus of road maintenance friction potential measurements is usually on the wet friction potential. The methods can be grouped into methods for local friction potential measurements and methods for continuous measurements. All methods are based on directly or indirectly measuring the forces transmitted when pulling rubber over a road surface. The operating conditions and type of the rubber differ between all methods. An overview of several used methods can be found in [18], [22] and [23]. Only one method to measure the local friction potential and the two continuous methods used in the measurements conducted for this thesis are described.

One of the most used local friction potential measurement methods is the British Pendulum Tester shown in figure 1.6. The test procedure is specified in ASTM E303 [25]. A pendulum equipped with a small rubber slider is released from the horizontal po-

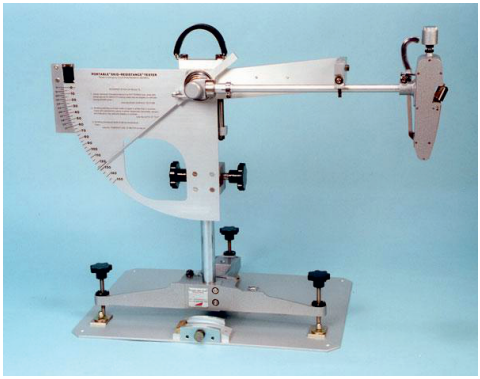

Figure 1.6: British Pendulum Tester [24]

sition. When the rubber pad hits the road surface it decelerates the pendulum. Depending on the remaining speed, the maximum amplitude defines the so called British Pendulum Number (BPN), a number between 0 and 150. A higher number indicates a larger surface friction potential. The sliding velocity of the rubber is around 10 kph. While this test is possible on dry surfaces, the standard test procedures use a wetted surface. In [26], measurements on six different asphalt surfaces resulted in values between 73 and 100.

Continuous surface measurements use trailers or trucks equipped with an additional measurement wheel to measure the friction potential. The tyre is forced into an operating point by either using a large side slip angle or large longitudinal slip values or it is even locked for the measurement. These methods are almost always used on wet roads, since the water cools the tyre preventing it from overheating and extensive wear. This enables these test methods to measure longer distances without changing the tyre. In addition, the dry friction potential is of less relevance to road maintenance. In this thesis, two continuous wet grip measurement methods have been used on a short test track.

Seitenkraftmessverfahren The Seitenkraftmessverfahren (SKM) method is based on the British Sideway-force Coefficient Routine Investigation Machine (SCRIM) used since 1970. Differences in the used measurement channels and tyres exist between the two methods. A comparison between Seitenkraftmessverfahren (SKM) and Sideway-force Coefficient Routine Investigation Machine (SCRIM) can be found in [27]. The

SKM method uses a truck with a large water tank equipped with a fifth wheel in the path of the right wheels. The tyre is purpose-built for the SKM truck. Compared to modern car tyres, the tyre is very slim and runs at a very high pressure. This wheel is mounted at a toe-in angle of 20°. The generated side-force of this wheel is measured using a load cell and divided by the static wheel load of 1960 N to calculate the friction potential. A speed-controlled amount of water is sprayed in front of the measurement wheel during measurements in a way that the calculated water height in front of the tyre is 0.5 mm. Additional measurements during the drive include the water temperature, the road temperature and the tyre temperature. Empirically derived correction equations for these temperatures and the driven velocity exist. A typical SKM truck and the measurement wheel can be seen in figure 1.7.

In Germany, the SKM method is used since 1990 during regular ZEB[6] road maintenance activities, where all motorways and federal streets are evaluated every 4 to 5 years. The typical measurement speed during these road surveys is 80 kph, with a valid measurement speed deviation of ± 4 kph, but measurement velocities of 60 kph and 40 kph for smaller roads are also specified. The measured friction potential values are usually averaged over 100 m, while raw measurement data is recorded every 0.1 m. The friction potential warning and limit values, required road renewal, have been defined based on the statistics of the first completed road network survey conducted in 1992 based on about 20 000 measurements. All recorded values were splitted into five classes. The lowest 5 % determine the renewal threshold. The next 10 % specify values below the warning value and 30 % of the roads are better than the target value. [19]

The derived values can be found in table 1.1. In addition, these values specified for the other allowed survey speeds of 40 kph and 60 kph are included.

RoadSTAR The RoadSTAR measurement truck has been developed in a cooperation between Forschungsinstitut für Kraftfahrwesen und Fahrzeugmotoren Stuttgart (FKFS) and Austrian Institute of Technology (AIT) in 1991. It is used to survey the wet road friction potential on Austria's highway network. The measurement method is based on a modified version of the Stuttgarter Reibwertmesser (SRM). This method uses a measurement wheel attached to the measurement truck behind the rear axle. The measurement wheel's rotation speed is reduced to a slip value of 18 % using a gearbox. A ribbed PIARC test tyre [30] is used as measurement wheel.

In front of the measurement wheel, a water height of 0.5 mm is applied, therefore

[6] Zustandserhaltung und Bewertung; regular road maintenance

Table 1.1: Assesment criteria for road friction potential with SKM and RoadSTAR method

Friction Class	Cumulative frequency	Method			
		SKM			RoadSTAR
		40 kph	60 kph	80 kph	60 kph
I	< 30	0.66	0.61	0.56	> 0.75
II	70–30	0.59	0.54	0.49	0.59–0.75
III	70–90	0.52	0.47	0.42	0.45–0.59
Warning Value		0.49	0.44	0.39	0.45
IV	90–95	0.45	0.4	0.35	0.38–0.45
Threshold		0.42	0.37	0.32	0.38
V	> 95	0.38	0.33	0.28	< 0.38

Table 1.2: Comparison of SKM and RoadSTAR method

	SKM	RoadSTAR
Method	Side Force Measurement	Longitudinal Force Measurement
Slip	20°	18 %
Water Height	0.5 mm	0.5 mm
Tyre	SKM	Ribbed PIARC
Dimension	3x20″	165R15
Load	1960 N	3500 N
Pressure	3.5 bar	2.0 bar
Measurement Speed	80 kph (40 kph, 60 kph)	60 kph (>40 kph)

the truck is fitted with a large water tank, which carries water for around 60 km of continuous measurement. In order to be able to use this measurement method in corners, the measurement tyre is fitted on a rotatable axis, which allows the tyre to move into a side-force free position by itself. Due to physical limits of this tyre rotation around this axis and the body roll of the measurement truck depending on the measurement velocity, a minimal measurable corner radius is specified [18]. The RoadSTAR truck and the measurement wheel can be seen in figure 1.7.

The resulting longitudinal force, static load and vertical acceleration are measured to calculate the friction potential. A standard measurement speed of 60 kph is used, while other measurement speeds faster than 40 kph are possible. In this case, the measurements are converted to a measurement speed of 60 kph using an empirical correction equation. The warning value and renewal threshold are defined in a similar empirical way as the SKM limits in Germany. These values are displayed in table 1.1. In addition to the standard measurement mode of 18 % slip, the RoadSTAR truck is also able to measure the locked wheel friction potential and simulate an ABS. The truck not only measures a friction potential but is also able to collect data on the lateral

(a) SKM truck

(b) RoadSTAR truck

(c) SKM measurement wheel

(d) RoadSTAR measurement wheel

Figure 1.7: Continuous friction potential measurement methods SKM [28] and RoadSTAR [29]

and longitudinal road evenness and the road texture using laser systems. A direct comparison of the friction potential measurement setups of SKM and RoadSTAR can be seen in table 1.2.

Comparison Between Different Measurement Methods

The large number of different friction potential measurement methods leads to the desire to compare measurements conducted with different measurement devices. Converting the BPN to friction potential values is difficult. In [31], a comparison between the British pendulum and the Grip Tester method, which is a trailer using the same measurement principle as the RoadSTAR truck, found no correlation. A more recent comparison between the British Pendulum Tester and the full braking test results conducted in [32] also found no correlation.

In 1992, 47 devices were tested on 54 different road surfaces in Spain and Belgium

[33]. A relation between the slip-speed, a macro-texture measurement, the Mean Profile Depth (MPD) and the measured friction potential was fitted with equation 1.7. The calculated value is called International Friction Index (IFI). It is supposed to describe the friction potential at a slip velocity of 60 kph. Therefore, it is often reported as F_{60}. This high slip velocity has been defined to represent a full braking manoeuvre with a locked wheel. Parameters for equation 1.7 and 1.8 are calculated using a linear regression. Parameters A_{ifi}, B_{ifi} and C_{ifi} belong to the friction potential measurement device, while parameters a_{ifi} and b_{ifi} belong to the surface texture measurement device and are used to calculate the correction parameter S_p.

$$F_{60} = A_{ifi} + B_{ifi}\mu_{pot}\ exp(-\frac{(60 - \tilde{v})}{S_p} + C_{ifi} \cdot MPD \tag{1.7}$$

$$S_p = a_{ifi} + b_{ifi} \cdot MPD \tag{1.8}$$

The reported error of the calculated F_{60} values is below 0.03 according to the PIARC measurement results [33]. Other researchers were not able to calculate these small errors. Problems with the IFI calculated by different measurement devices are for example discussed in [34].

In 1996, based on the PIARC experiment a new study using 15 friction potential measurement devices used in Europe has been conducted [35]. The aim of this study was to find a harmonisation between the different measurement devices used in Europe and to show a good reproducibility of measurement results, so that the European Friction Index (EFI) standard could be applied across Europe. A number of measurement trials was conducted across five European countries covering a representative amount of different road surfaces. The measured road surfaces included public roads and proving grounds. Instead of the slip speed of 60 kph, a slip speed of 30 kph was found to be more representative for devices used in Europe. The initial tested formula was kept from the IFI. In addition to the reduced slip speed, the two device specific parameters for the MPD a_{ifi} and b_{ifi} were replaced by fixed values. During the experiments, it was discovered that the procedures for finding the device specific parameters A_{ifi} and B_{ifi} were not iterating to physical valid results. With each calibration iteration the values for A_{ifi} increased and the values for B_{ifi} decreased. Therefore, very low grip surfaces would have a high friction potential of A_{ifi} and the sensitivity of the devices towards changes in friction potential would reduce due to the multiplication of the F_{30} value with B_{ifi}. In addition, some results did not follow the curve prescribed by the IFI model. Therefore, a number of different approaches to calculate the input parameters of each device have been tested. Although some

models were able to improve the correlations between different devices, no satisfying harmonisation model was found.

Since the IFI and EFI calculations are not sufficient to predict the friction potential and thus the maximum deceleration a vehicle could achieve, the relation between measurements of continuous friction potential measurement methods and the deceleration of a vehicle are of special interest. Two research projects already derived a relationship between the devices SKM and RoadSTAR used in this thesis. The results of these two research projects are summarised next.

Van der Sluis [19] compared SKM with 60 kph and 80 kph with measurements of full braking tests at starting velocities between 60 kph and 130 kph. The author used 20 m average SKM values in the analysis. The full braking tests were conducted with ABS switched on and off. Since all autonomous cars will be equipped with a functioning ABS, only these results are relevant for this thesis. The tests were conducted on closed highways and proving grounds. Different cars were used for the braking tests in order to include the influence of different vehicles but the final analysis conducted combines the measurements of the different types of vehicles. The tests conducted on 15 different surfaces were used to develop a relationship between the SKM value and the MFDD. The relevant results of this work are shown in figure 1.8. The linear correlation coefficient of around 0.6 only indicates a rather weak linear correlation between the SKM values and the MFDD.

The results of one specific vehicle, the Ford Mondeo, evaluated individually show a slightly better correlation coefficient of 0.71 but the results of this vehicle also show that the MFDD on roads with a very small SKM value around 0.3 can be as good as on roads with high SKM values of 0.9. In addition, the measurements of all vehicles show that on almost all surfaces MFDD values of more than $6\,\mathrm{m\,s^{-2}}$ can be reached.

Maurer conducted a similar work in order to find a correlation between RoadSTAR and the braking distance of vehicles [18]. Two different test series were conducted. The first test series was used to evaluate different influencing factors, while the second main test has been used to evaluate the relationship between the RoadSTAR and different vehicles. The main measurements were conducted on a proving ground with six different surfaces. The full braking tests were conducted by two vehicles and with different tyres. A new summer tyre, the same tyre with only 1.6 mm profile depth, an all year tyre and the ribbed and smooth PIARC tyre have been used in the tests. Different starting velocities of 40 kph, 60 kph, 80 kph and 100 kph have been used. Similar to van der Sluis, once again tests with activated ABS and without have been conducted. Over 200 measurements are included in the final analysis. In addition to the full braking tests, the vehicle tyres were fitted to the RoadSTAR truck and used to evaluate

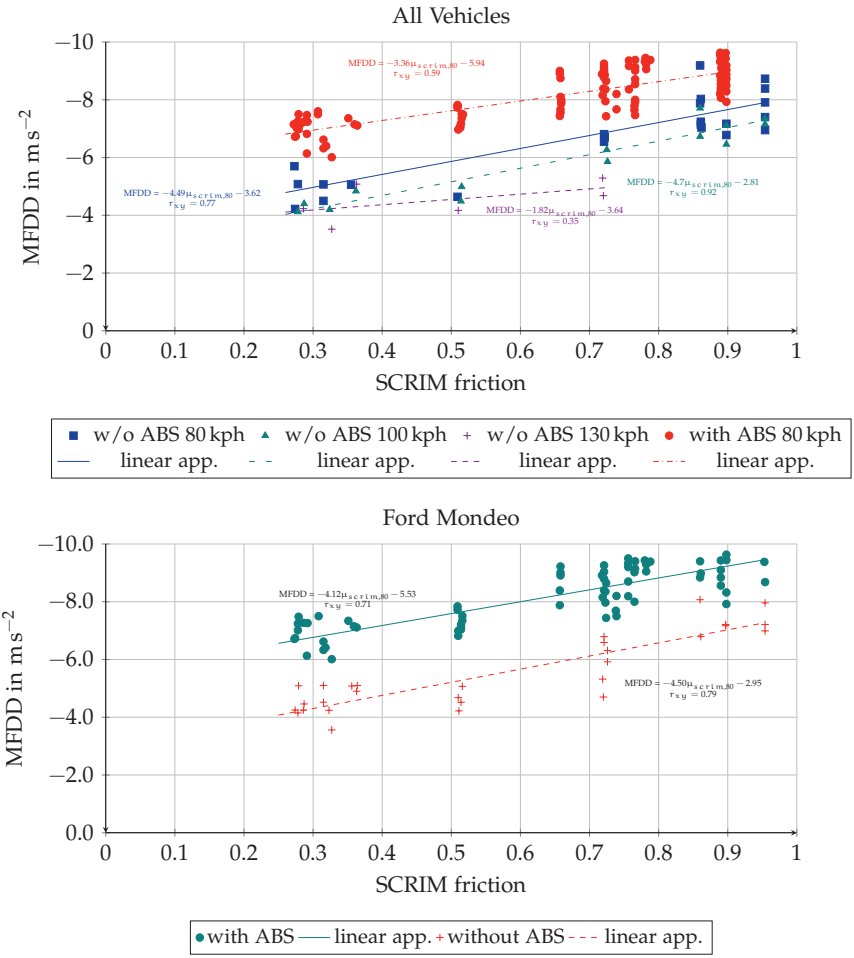

Figure 1.8: Correlation between vehicle deceleration and SKM measurements based on [19]

the friction potential of the six surfaces. A very good linear correlation between the stopping distance and the measured RoadSTAR measurements was found. For each tyre the correlation coefficient is above 0.9. Although this could be explained by the very low number of data points used in the calculation (< 10) and the large friction potential variation between the proving ground surfaces.

The relationship between the RoadSTAR measurements $\mu_{Roadstar}$ and a_{mean} of the vehicle can be described by

$$a_{mean} = g \cdot ABS \cdot Tyre \cdot K \cdot \mu_{Roadstar} \tag{1.9}$$

In equation 1.9, g is the gravitational acceleration constant $9.81\,m\,s^{-2}$. The variable ABS has been derived by comparing vehicle measurements conducted with and without ABS. In the first test series, it was found that for starting velocities above 80 kph, the deceleration with ABS is up to 25 % higher. During the main test, improvements between 20 % and 24 % were measured. The author chose to set the variable ABS to 1.25 if the ABS system is available.

The variable Tyre has been derived by comparing the friction potential measurements of the RoadSTAR Truck equipped with the standard ribbed PIARC tyre and the truck fitted with other tyres. It was found that the performance of the PIARC tyre can be seen as a lower bound. Other tyres proved to perform up to 42 % better. The remaining constant K has been fitted in a way that equation 1.9 fits the measurements. The constant K has values of around 0.75. Using the equation the measurement results of the full braking tests can be reproduced with relative errors below 12 %.

1.2.2 Friction Potential Estimation Methods

In the last almost thirty years numerous methods for friction potential estimation have been proposed. Due to the large number of different methods, different sorting schemes have been used in the past to sort the methods. In [36], the classes are divided into direct and indirect methods, while [37] differentiates between experiment-based and model-based classes. More commonly the classes effect-based methods and cause-based methods are used [38, 39, 40]. These two classes are equally used in this thesis.

Effect-based methods try to identify the effect of different friction potential values on vehicle dynamics or wheel dynamics. The name effect-based methods is equivalent to direct methods or model-based methods mentioned before. Cause-based methods measure one or several parameters linked to changes in the friction potential and use

empirical data or a model in order to infer the friction potential. A variety of published methods of both groups will be discussed in detail in the next sections. The friction potential estimation components proposed in this thesis fall into the group of cause-based methods.

Effect-based Estimators

A majority of research in the recent years focuses on the development of effect-based estimation methods. The advantage of these methods is that most of them use already available vehicle sensors. Three different groups of effect-based estimation methods are popular in literature: Methods estimating the effect of friction potential changes on the longitudinal dynamics, on the lateral dynamics and on the aligning moment. All these methods follow a similar process. First required vehicle or wheel operating conditions are measured or estimated. These are then used to fit a tyre model and finally this tyre model is extrapolated to find the friction potential value. The methods differ in the used estimators, sensors and tyre models.

Longitudinal Dynamics Methods estimating the friction potential using longitudinal dynamics can be further split into methods, which estimate the friction potential at very low acceleration levels, called slip-slope methods, and methods requiring larger utilisation levels of the friction potential.

Slip-slope Methods Slip-Slope methods operate on the assumption that the initial slope of the tyre force slip curve depends on the friction potential. One of the first publications of this method is from Gustafsson [41]. In his work, Gustafsson does not use a functional description of the dependence of the slip-slope c_κ and the friction potential μ_{pot} but only uses detected changes in c_κ to classify the road surface. c_κ is described by a linear relationship between the slip and the used friction (equation 1.10). The method thus only requires slip measurements and the traction torque of the driven axle. The wheel slips are calculated by comparing the wheel speeds of the driven axle with the free-rolling one, which defines the reference velocity. This limits the method to front or rear wheel driven vehicles and acceleration situations. Small differences in the tyre radii, rolling resistance and other uncertainties of the front and rear axle are included in an axis intercept parameter named κ_e.

$$\mu = c_\kappa(\kappa + \kappa_e) \tag{1.10}$$

Gustafsson proposes a least squares method and a Kalman filter to estimate the slip-slope c_κ. In order to separate the unknowns c_κ and κ_e and to cope with the noisy slip measurements, Gustafsson uses the transformed equation 1.11 in the estimator.

$$\kappa = \mu \frac{1}{c_\kappa} + \kappa_e \tag{1.11}$$

Of the two proposed methods, Gustafsson implements the Kalman filter. In order to have an accurate estimate of the slip-slope, the Kalman filter needs to be tuned very slow, which prohibits the filter to detect sudden changes in the slip-slope quickly. To solve this limitation, several error detection algorithms are compared and finally a two-sided cumulative sum method is used to adapt the covariance matrix of the Kalman filter. Gustafsson was able to detect the change between asphalt and gravel using this method online on a test track.

Gustafsson's method has been picked up by Yi et al. [42]. In this publication, a slip-slope based method is once again used. In order to estimate the required parameters, a linearised observer is developed to estimate the torque of the driven axle. The slip is once again calculated using the wheel speeds of both driven and undriven axles. The relationship between the slip and the tyre force is estimated by a least squares method or a linear observer method. In contrast to Gustafsson's work, a non-linear mapping between the slip-slope and the friction potential is assumed but the relationship is not specified. The estimators developed in this paper have been validated using a simulation, which employs a magic formula tyre model[7] and measurements with a test vehicle. Measurements published in this paper show that the slip-slope of wet asphalt is higher than the slip-slope of dry asphalt.

In contrast to this observation, Lee et al. [43] assume a linear relationship between the friction potential and the slip-slope with the slip-slope of wet asphalt being smaller than the slope of dry asphalt. In this paper, a least squares method is used to estimate the slip-slope. Lee included calculations for the normal force, tyre rolling radius and observers for the brake torque and traction torque in this model. This way, the method can be used during braking and accelerations but he required a fifth wheel to measure a reference velocity. Li [44] proposes the combined use of an extended Kalman filter and an observer with the measurement inputs wheel rotational velocity, traction torque and an accelerometer to estimate the reference vehicle velocity. Rajamani [45] proposes different sensor setups using Global Positioning System (GPS), accelerometers and traction/brake torque measurements to estimate the slip-slope. A slip-slope method is also included in the suite of estimators developed by Ahn [46]. Vehicle

[7] see section 2.2

measurements show different slopes of ice, snow and concrete with an assumed linear relation between slope and the friction potential in this study.

As the above mentioned sources show, the slip-slope method is a very popular method, since it only requires available sensors. Linear estimators are sufficient to estimate the slope parameter. In addition, normal driving would provide all required information to classify the friction potential but the sources use different assumptions on the correlation between the slope and friction potential. Since the simple brush tyre model[8] does not predict the relationship between the slope and the friction potential, several researches investigated this relationship in theory and with extended experimental tests. Uchanski [47] explained the decrease in slope on lower friction potential surfaces with the so called 'secant effect'. This effect explains the result by fitting a linear regression line through parts of the tyre-slip curve, which are already inside the non-linear region. Other possible effects have been proposed and measured in an extensive experimental study by Deur [48]. He attributes the decreased slope to shear effects in the ground plane for ice and snow. He provided evidence for this assumption by showing that dry ice resulted in a higher slope than wet ice, while the friction potential of both surfaces was low. He attributes additional changes in the slip-slope on different surfaces to different rolling resistances.

Additional measurements have been conducted by Müller [39], where repeatedly only the left-front wheel has been braked until the friction potential was reached. The friction force has been measured using a wheel torque sensor. This measurement method has some similarities to the proposed reference measurement method developed in chapter 3. The measurement results show, that the friction potential only depends on the estimated slip-slope if a significant amount of the available friction potential is used. This is an additional evidence for the 'secant effect'. Furthermore, it was stated, that measurement noise in the slip calculation leads to significant amounts of misclassifications. Although the slip-slope method is not the focus of this thesis, during the validation of the developed reference method, the tyre curves on seven different surfaces have been measured. These results are discussed in section 3.2.2.

Medium to High Acceleration In contrast to the slip-slope method, other methods require accelerations which use the non-linear part of the tyre slip-force curve to estimate the friction potential. Ono [49] introduced the Extended Brake Stiffness (XBS), which is defined as the derivative of the tyre force curve $\frac{dF_x}{d\kappa}(\kappa)$ at the current slip value. At the friction potential, this value is 0. Ono showed a relation between low

[8] see section 2.2

frequency wheel rotation vibrations to this XBS and used it to estimate the remaining margin to the friction potential. Villagra [50] used the extended slip stiffness to detect the wheel reaching the non-linear part of the slip curve and then fitted a Dugoff Tyre model to calculate the friction potential.

Ray [51] developed a particle filter based approach to estimate the friction potential. In her work, she used an extended Kalman filter to estimate vehicle states like slip and side slip angle and the tyre forces. These results are compared to results of a tyre model with different fixed friction potential values and the most likely solution is chosen as friction potential. This also requires knowledge about the tyre curves for the model. Lex [13] extended this particle filter approach and investigated different re-sampling methods for the particles.

In [36], the model parameters of a brush tyre model have been estimated using a least-squares method. This method only works if the gathered and stored force-slip data contain the curved part. A friction utilisation of around 80 % was required to achieve accurate results. Albinsson [52] tried fitting different tyre models to a large number of tyre measurements on snow and concluded that in order to estimate the friction potential with an error of less than 10 %, the magic formula tyre model required an acceleration of more than 65 % in the absence of noise, and more than 90 % with added measurement noise. Other tyre models showed worse performance than the magic formula.

It can be summarized, that methods to estimate the friction potential in medium to high acceleration situation exist. In this region, the relationship between the XBS and the friction potential is undisputed but clear disadvantages are that accelerations for accurate estimations rarely take place during normal driving and that assumption about the tyre curves (at least a simple non-linear tyre model) have to be available. Often non-linear estimation methods have to be used and estimating the correct reference velocity poses an even bigger problem than for the slip-slope methods.

Lateral Dynamics The principles behind friction potential estimation using the lateral dynamics are similar to the longitudinal dynamics. The difference is that these methods require lateral accelerations for the estimation. These methods require the measurement or estimation of the side slip angle or a related quantity. Hahn et al. [53] use differential GPS, steering angle and a gyroscope to fit a non-linear tyre model to the front tyres. The estimation algorithm is based on a simple bicycle model. Baffet et al. [54] use a comparable test setup and test an extended Kalman filter in combination with different tyre models. The test results show that slip angles larger than 4° are required to estimate valid tyre curves. In addition, he proposes a linear model

for the lateral tyre slip-stiffness. Solmaz [55] developed an estimation approach for estimating the side-slip angle and friction potential simultaneously using a number of models initialised with different friction potential values to estimate the side slip angle. The corresponding friction potential coefficient is then chosen by minimizing an error function. Villagra [50] extended his XBS to lateral slip estimation.

Aligning Moment A more promising approach investigated by several researchers is based on the aligning moment around the steer axis. The aligning moment is more sensitive to the friction potential than the longitudinal or lateral force [36], because two parameters depend on the friction potential, the lateral forces and part of the moment arm, the pneumatic trail. Matilainen [56] uses tie rod force measurements on both front wheels and derives an algebraic formulation for the friction potential. These kind of force measurements are normally not available in production cars. Therefore, other publications use the steering torque available from electronic power steering.

Hsu [57, 58] uses GPS to measure the vehicle slip angle and the steering torque from a steer by wire steering system. Together with a steering-system model and a non-linear observer, the pneumatic trail is estimated. Bobier [59] also applies this concept and proposes an optimised suspension design, which separates different torque components acting around the steering axis so that the performance of the friction potential estimator is improved.

A method comparable to the aligning moment estimator of Hsu is proposed by Matsuda [60]. Again a bicycle model and steering system model is used to estimate the friction potential and side slip angle. As estimator an extended Kalman filter is used, in which the friction potential is assumed as random walk variable.

Liang [61] published an aligning torque estimator, which is based on estimating the ration between the side-slip angle and the friction potential $\frac{\alpha}{\mu_{pot}}$. Inputs to this estimator are the steering torque, yaw rate, lateral acceleration and longitudinal velocity. The concept is based on two observers, where the first one estimates the lateral forces and the second one uses the output of the first to estimate the friction potential. An advantage of this algorithm is, that it uses a threshold to decide if a reliable friction potential estimation can be provided.

Intelligent Tyres The last group of effect-based methods presented is the only one requiring special sensors, which are currently not available in production cars. These estimators use sensors embedded in the tyre tread. Due to technical difficulties concerning power supply and data transmission in the rotating tyre, these kind of sensors

will pose increased costs and will only be viable if they provide significant benefits. Nevertheless, they are a popular research topic.

Niskanen [62] used a piezoelectric accelerometer and conducted measurements on different road surfaces. He shows that it is possible to classify the road condition this way. Singh [63] is also able to classify different road surfaces by measured vibrations using acceleration sensors. Matilainen [64] used a three-dimensional accelerometer to measure the contact length and has been able to detect aquaplaning situations early due to a decreased contact length.

While all the previously mentioned publications use acceleration sensors, Tuononen uses a camera mounted in the rim and a LED mounted on the inner liner of the tyre to measure the carcass deflection [65]. He showed that it is possible to measure longitudinal and lateral tyre forces and the normal load. These measurements can be used as inputs to friction potential estimators described in the previous section.

Cause-based Estimators

Cause-based friction potential estimators use sensors to detect factors influencing the friction potential. Due to its impact on the friction potential, the most common measured factor is the intermediate layer. Many of these concepts have been investigated in the EU-project 'Friction' [66]. Cause-based estimators often require special sensors for the measurement. In addition, a model of the friction potential dependence on the measured property needs to be known. Since not all influencing factors are measured, these methods are conceptually less accurate than effect-based estimators. Their main advantage is that they do not need any vehicle accelerations. As a consequence they can provide continuous friction potential information. The main groups of cause-based estimators will be presented in the next section.

Acoustic Eichhorn [67] first investigated the relation between tyre noise and friction potential. These kind of methods require a microphone near the tyre. The greatest challenge of these measurements is to filter out unrelated environmental noise. Often, models are used to subtract known noise sources like engine noise.

More recent publications rely on offline training and machine learning techniques to classify the road surface or intermediate layer. Zhang [68] used a microphone mounted near the tyre and compared the measurements to reference measurements with the aim to detect the mean texture depth. The data-set consists of 44 different road surfaces. The proposed estimation algorithm uses a principal component analysis to separate the tyre generated noise from other noise sources and calculated the energy

amount of the first component. Boyraz [69] used microphone measurements to train an artificial neural network to classify different road surfaces. She evaluated different measurement windows and features used for the classification. Abdic [70] used a large dataset of microphone measurements to train an Artificial Neural Network (ANN) to detect wetness. The large data set is used in order to account for different noise created on different road surfaces. All previously mentioned publications require external microphones. Akama [71] proposed using an internal voice recorder. He used previously measured reference recordings on different road surfaces and a Bayesian estimator to classify different road surfaces.

Vision Vision based methods use the cameras mounted in many vehicles. Thus, they only require special algorithms. Several researchers have proposed methods to use the camera images to classify the road condition.

Holzmann [72] extracted up to nine 30 pixel slices of the road ahead from an image. In each of these slices, he calculated a co-occurances matrix. This is a matrix, in which the gray-scale value of a pixel is compared to the gray-scale value of the right neighbour pixel. The most extreme non-zero entries in this matrix are used to map the image to one of six friction potential levels. Holzmann warrants this method a good performance without specifying any quality criteria.

Hartmann [73] proposes a method, which extracts an unobstructed part of the lane ahead from a front camera. Features like the reflectivity and the texture are extracted from this image. Finally, the classification method 'extremely randomized trees' is used to classify the image into the classes dry, wet and snow. This method identifies the correct road condition in 96.8 % of the tested cases.

Panhuber [74] extracts up to three different parts from the camera image. These are the tyre lanes behind the leading car and the road behind the leading car, if there is any and the road ahead of the own vehicle. For each region a different classification method is used. The tyre lanes of the leading car are classified using an ensemble of neural networks. The road behind the leading car is classified using random trees and the road in front of the car is classified using a convolutional neural network. The three methods are merged by weighting them according to a confidence parameter provided by all three classification methods. This fused method reaches a differentiation accuracy of 86 % between the classes dry and wet.

Special Sensors In several projects, a sensor called RoadEye has been used [66, 36]. This sensor uses several near infrared lasers and detects the back-scattered light to classify the road conditions dry, wet and ice. Casselgren [75] compares the results of

the RoadEye sensor to classification results of another special sensor called IcOR. The IcOR consists of two cameras, where one is fitted with a vertical shutter and the other with a horizontal one. The classification algorithm uses the differences of both images to detect water or snow on the road surface. Casselgren reports that the RoadEye Sensor is able to detect water or ice in 80 %-95 % of the measurements, while the IcOR sensor only archives a detection rate of 70 %-80 %.

Haekli [76] has deployed 24 Ghz radar to detect the surface condition. This radar prototype measures the horizontal and vertical back-scattering properties of the surface. Initial measurements suggest that this sensor can detect leaves and ice on the road. Previously, the use of radar has been assessed by Rudolf [77]. Although this work did not implement a classificator, conducted measurements on different surfaces indicate that the use of radar information to classify the road condition seems feasible.

Potentials of Vehicle2X Vehicle2X or Car2X communication is the basis for future intelligent transport systems, where X stands for the communication partner. Possible communication scenarios are vehicle communicating to other vehicles (V2V), vehicles communicating with surrounding infrastructure like traffic lights or traffic signs (V2I) or vehicles communicating to central control centers. The used communication methods are WLAN and mobile connections. [78]

The CAR2CAR Communication Consortium, a non-profit organisation founded by European vehicle manufacturers, which supports the development of the European Car2X standards, presents different applications in their manifesto [79], one of which is the decentralised environmental notification application, which includes a hazard warning use case. This use case includes warnings about dangerous road conditions like slippery roads with black ice listed as an example. Information about these events are generated through ESC interventions.

Atilla [80] describes an adverse weather warning system tested in a field operational for Car2Car communication in the context of sim^{TD}. This adverse weather warning system includes warnings, which are closely related to the friction potential. Warnings were generated by vehicles and Road Weather Information Systems (RWISs). Adverse weather warnings included in this project were heavy rain, reduced visibility due to fog, strong cross winds, slippery road due to ice or snow and aquaplaning. In [81], the message generation conditions are detailed and for the friction potential related messages repeated in the next paragraphs.

A vehicle sends a warning about a slippery road if the traction control system is active, while the throttle is opened less than 30 %, the outside air temperature is less or equal 2 °C and the velocity is less than 8 m s^{-1} or the ABS control is active while

the braking pedal is pressed less than 40 %, the outside air temperature is less or equal 2 °C and the velocity is less than 14 m s^{-1}. Additional information like acceleration levels increase the quality of the message. A RWIS[9] issues a slippery road warning, if the surface temperature is less or equal 0 °C the measured surface state is ice or snow and the surface layer thickness is more than or equal 2 mm.

On the vehicle site, a heavy rain warning is generated if the wiper runs at maximum level, the low beam is activated and the vehicle speed is below 28 m s^{-1}. A RWIS sends a heavy rain warning, if it measures more than 20 mm h^{-1} precipitation with precipitation type rain and an air temperature above 2 °C.

Aquaplaning warnings are generated by the vehicle if ESC or ABS are active, the brake pedal pressure is less or equal 40 % and the outside temperature is above 2 °C and the vehicle speed is below 25 m s^{-1}. Warnings are provided by the RWIS if the measured surface condition is wet and the surface layer thickness is more or equal 7 mm.

This weather warning functionality has been tested in a field operational test with 120 vehicles for a duration of 6 months and includes 15 000 slippery road situations. According to the author, the rate of undetected adverse weather situations is negligible low[10]. Similarly, the rate of falsely generated warnings is described as low.

Panahandeh [82] used Car2X data generated by Volvo vehicles during one year. These vehicles send information to a server on whether the road is slippery or not. Panahandeh investigated using these Vehicle2X events together with RWIS data to predict if the road is slippery in the next 30 minutes. For this prediction task, several machine learning methods, logistic regression, support vector machine and ANN are tested. The different classification methods resulted in a prediction accuracy between 70 % and 80 %.

Müller [9] used a combination of vehicle data, including wiper speed and outside temperature, together with weather data from weather stations and a RWIS to classify the road condition. The used classes were dry, moist, wet and snow/ice. A logistic regression method was used to combine the different data sources. The logistic regression parameters have been trained using data from two years of test drives around a specific track. The intermediate layer is correctly classified in about 85 % of the tested data. After the determination of the intermediate layer, a friction potential range is chosen from a database according to the intermediate layer and position on the course.

[9] see section 5.1.1 for a detailed introduction

[10] This result seems dubious given some of the trigger conditions. Especially, for the aquaplaning case the trigger limit is at very high water heights, while the literature described in section 2.1.3 indicates the possibility of aquaplaning at lower water heights.

Due to relatively large friction potential classes ($\Delta\mu \approx 0.3$) and overlapping friction potential ranges for the different classes, the correct friction potential range is provided in over 90 % of the collected cases.

1.3 Objectives

The state of the art showed that the previously developed methods do not fulfil the requirements needed for trajectory planning as they are not able to continuously guarantee the availability of the friction potential estimation and do not provide a sufficient spatial preview distance. Autonomous vehicles will have different accuracy and availability requirements and other technological capabilities than current road vehicles. Therefore, new approaches to estimate the property friction potential can be analysed. The main technologies applicable are that autonomous vehicles require a high definition map, which can be supplemented with additional information. In addition, the vehicle will always be connected to a backend server, which can handle large amounts of data and has a lot of processing power.

Thus, the main objective of this thesis is to develop a friction potential estimation method, which can be used for trajectory planning. This aspired method has to guarantee a lower bound of the friction potential. The information has to be available continuously and at least 100 m in front of the vehicle. According to the reviewed literature, this can only be achieved using a cause-based method, which incorporates external information like map data and weather information. The accident statistics (see section 1.1) and previous research of cause-based methods (see section 1.2.2) highlight, that the tyre type, the road surface and the intermediate layer have a significant influence on the friction potential.

Since no published method focused on the previously mentioned requirements, within the scope of this thesis, the important influencing factors shall be identified and their influence quantified. All relevant influencing factors will be considered in the cause-based method or it will be accounted for the introduced uncertainty by omitting them.

In order to evaluate the different influencing factors, a database of friction potential measurements will be collected and their influence on the friction potential will be evaluated.

Furthermore, since in literature the road surface texture is already identified as one of the main influencing factors, the wet friction potential measurement methods SKM and RoadSTAR used in road maintenance shall be evaluated and compared to the

collected database. The results of this evaluation will answer the question, if the measured data can be used to continuously map the friction potential for the use as a layer in the HD-map of the AV. The aspects focused on are the correlation of the different measurement methods, the repeatability and the achievable measurement coverage. In case of the RoadSTAR measurement, several measurement properties will be modified with the aim to represent the friction potential of the AV more accurately.

The intermediate layer is the other influencing factor covered by several cause-based methods. In order to fulfil the preview requirements, weather data will be collected for all measurements. This data is then used as input for several machine learning methods. The classification accuracy and possible modifications to these methods will be compared and the most appropriate selected to estimate the possible quality of the cause-based method.

Last, the friction potential that can be guaranteed using the selected method and the available friction potential measurements will be highlighted and the remaining risk of exceeding the guaranteed friction potential using the developed friction potential estimation method shall be gauged.

1.4 Outline

Chapter 1 gives a general introduction to the friction potential estimation problem. Friction potential related accident statistics are analysed. The specific requirements for friction potential estimation in the context of autonomous driving are introduced. The state of the art of friction potential measurement methods and friction potential estimation methods is provided.

Chapter 2 focuses on the relationship between different parameters influencing the friction potential. A short overview of the relevant rubber properties and rubber friction theories is provided. Furthermore, the mechanism of aquaplaning is highlighted. Finally, two commonly used tyre models are introduced.

Chapter 3 describes the development and validation of the new reference friction potential measurement method named Single Wheel Braking (SWB)$_3$. In addition, the process of generating a reference database using this measurement method is explained. The results gathered in this database are used to analyse the effect of several factors influencing the friction potential.

Chapter 4 describes the results of the SKM and RoadSTAR friction potential measurement methods, and their usability to generate a map attribute describing the

road surface properties. Results of both measurement devices are correlated to the vehicle measurements described in the previous chapter.

Chapter 5 deals with the problem of identifying the intermediate layer on the road. First, the available weather observations and reference sensors are introduced. Several classification methods are presented and compared. Two different classification methods, the linear classification method multinomial logistic regression and the non-linear method of a multilayer perceptron are applied to the data. The results of both methods are compared to several other methods found in literature.

Chapter 6 The results of the previous chapters are combined to provide a coarse approximation to the remaining accident risk if the grip map and intermediate layer estimation are applied.

Chapter 7 summarises the outcome of the thesis. Finally, an outlook of further required development steps will be provided.

2 Fundamentals of Tyre Friction and its Effect in Tyre Models

In the previous chapter, it was deduced that only an effect-based method is capable of providing the preview requirements needed for trajectory planning. Therefore, it is important to get an overview of the influencing factors in order to decide which ones should be considered in the estimation and how they influence the available friction potential. This chapter highlights the interaction of these influencing factors, starting with rubber properties, explaining the interaction between the tyre and the road surface, and highlighting two simple tyre models used in vehicle dynamics and effect-based friction potential estimation methods.

2.1 Important Influencing Factors

The friction potential depends on many different factors. Figure 2.1 provides an overview of them. These factors can be attributed to four different classes, the vehicle, the tyre, the road and an intermediate layer between tyre and road. Many of the influencing factors interact with each other. Thus, this chapter can be understood as overview, but no clear ranking of the influences can be given.

Friction μ between the rubber-block sticking or sliding over a road surface is the sum of different mechanisms generating a horizontal force F_h divided by the normal load F_z. In literature, the tyre road friction generation is split into several physical phenomena, which are often considered acting separately so that the contribution of each factor can be added to calculate the overall friction. The friction mechanisms considered as important vary in literature. According to Kummer [83], the four different mechanisms hysteresis F_{hyst}, adhesion F_{adh}, cohesion $F_{cohesion}$ and viscous F_{vis} force (equation 2.1) contribute to the rubber friction potential, while in his earlier publications, Persson argues that only the hysteresis is important [84]. In later research, Tolpekina and Persson [85] also attribute the adhesion component an important contribution to the friction potential. They also introduce another friction component, which they attribute

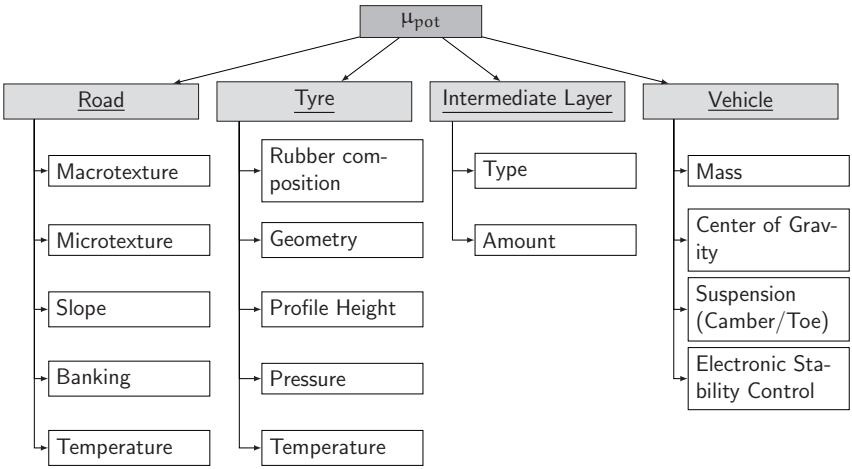

Figure 2.1: Overview of influencing factors

to hard filler material scratching over the surface.

$$\mu = \frac{F_h}{F_z} = \frac{F_{hyst} + F_{adh} + F_{cohesion} + F_{vis}}{F_z} \tag{2.1}$$

In the following sections, the relevant properties of the road surface are introduced. Next, the basic properties of rubber and rubber compounds used in tyres are explained, followed by a short introduction to Persson's rubber theory, which is able to predict the rubber friction potential in some cases. Finally, the influence of an intermediate layer is introduced. A special focus is on the aquaplaning phenomenon as well as ice and snow, since both are prominently featured in the accident statistics.

2.1.1 Road Surface

Road surfaces are commonly made of asphalt or concrete. The surface roughness originates from small stones embedded into the material. According to ISO 13473-2 [86], the relevant irregularities are named micro- and macrotexture. The microtexture is the road unevenness up to length scales of 0.5 mm. The road macrotexture is defined by wavelengths from 0.5 mm up to 50 mm. Both micro- and macrotexture contribute to the hysteresis friction. Persson's friction theory [84] uses the power spectral density of the road surface including micro- and macrotexture (equation 2.2). In this equation $h(x)$ describes the height of the road asperities and $h(0)$ denotes the average height of

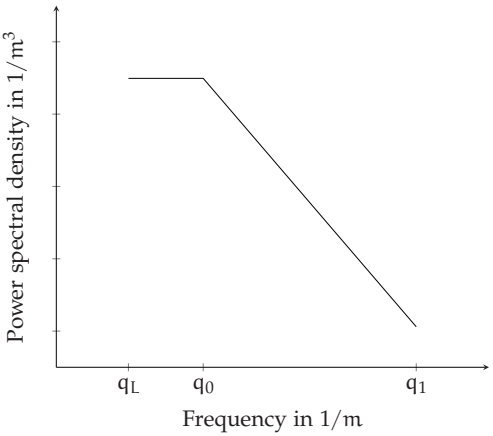

Figure 2.2: Power spectral density of a road surface which is self-affine fractal between $\mathbf{q}_0$ and $\mathbf{q}_1$ based on [87]

these asperities.

$$C(\mathbf{q}) = \frac{1}{(2\pi)^2} \int \langle h(\mathbf{x}) h(\mathbf{0}) \rangle e^{-i\mathbf{q}\mathbf{x}} \tag{2.2}$$

Road surfaces can normally be described as self-affine fractal surface between a well defined wave spectrum, where the cutoff frequency $\mathbf{q}_0 = 2\pi/\lambda_0$ is defined by the largest stones inside the asphalt. The slope of the curve is defined by the fractal dimension (D_f), which for road surfaces is between 2.2–2.5. The approximation of such a roughness power spectral density of a self-affine fractal road surface with cut-off length $\mathbf{q}_0$ can be seen in figure 2.2.

Other researchers use measurements of the road macro- and/or microtexture to calculate characteristics like the Mean Profile Depth (MPD) or the Mean Texture Depth (MTD) [88]. The macrotexture parameter MPD is defined by the distance of the average height of a baseline of 100 mm, and the average of the highest peak in the first 50 mm and the highest peak in the second 50 mm. The exact procedure to calculate the MPD is described in ISO 13473-1 [89]. The MPD is used to correlate the results of different friction potential measurement systems and calculate the EFI. Eichhorn [90] uses macrotexture measurements to define several own texture characteristics. Klempau [91] extended the model to include the microtexture since macrotexture alone proved insufficient to accurately estimate the friction potential.

The surface texture of roads changes due to wear. Thus, it is important to have surfaces which are resistant against wear. The polishing effects and prediction models are usually done in laboratory tests [92, 93] using a Wehner-Schulze friction test device, which allows to rotate rubber cones over a circular surface. Thus, it is possible to simulate the polishing effect of many vehicles in a short period of time. The device also allows the measure of a friction potential value. This measured friction potential has been related to RoadSTAR measurements in [94] with a rather good linear correlation, which results in a correlation coefficient larger than 0.8. Therefore, the model published in [93] can be used to predict RoadSTAR measurements. The road's micro- and macrotexture not only changes due to polishing, but researchers also observed seasonal changes [95, 96]. According to [95], in winter freezing water creates fractures and removes small stones, thus increasing the texture roughness. During the summer months, polishing once again reduces the texture roughness. Similarly to the surface texture, seasonal friction potential changes are observed. These changes are often attributed to the surface and ambient temperature instead of the surface changes [97, 98].

In addition to the contribution to the hysteresis friction, the road texture also is important for the drainage properties of the road. Especially a large macrotexture is important. On a larger unevenness scale, roads are usually designed with a banking, which supports effective drainage of the road. German highways are designed with a banking of at least 2.5 %, but lane grooves and other irregularities like pot holes can prevent an efficient drainage of the road.

Last but not least, the surface temperature influences the friction potential. The properties of the rubber are expected to change more with changing temperature than the properties of the surface. Therefore, the temperature effects are explained in the next section.

2.1.2 Tyre

The tyre is the counterpart of the road and thus its properties also have major impact on the transferable forces. Tyres are made of rubber, which is a visco-elastic material leading to complex interactions with the uneven road surface. These interactions are highlighted in this section by providing a short introduction to general rubber properties. Next, the previously mentioned rubber friction theory by Persson is summarised. Finally, a short overview of the construction of a tyre is provided and design considerations leading to different tyre performance are introduced.

Physical Properties of Rubber

Rubber is a material consisting of long polymer chains obtained from rubber trees or produced synthetically. It is a visco-elastic material combining mechanical properties of elastic and viscous materials. The stress σ of an elastic material is proportional to the strain ϵ with the factor E known as Young's modulus

$$\sigma = E\epsilon. \tag{2.3}$$

Given a sinusoidal input with angular frequency ω_f and amplitude ϵ_0 for the strain

$$\epsilon = \epsilon_0 \sin(\omega_f t), \tag{2.4}$$

the stress can be calculated by

$$\sigma(t) = E\epsilon_0 \sin(\omega_f t) = \sigma_0 sin(\omega_f t). \tag{2.5}$$

In a viscous material, the stress is proportional to the strain rate. The property η is called the dynamic viscosity of the material.

$$\sigma = \eta \frac{d\epsilon}{dt} \tag{2.6}$$

Given the same sinusoidal input as before, the resulting stress is

$$\sigma(t) = E\epsilon_0 \sin(\omega_f t) = \sigma_0 sin(\omega_f t + \delta) \tag{2.7}$$

with a phase lag $\delta = \frac{\pi}{2}$. For visco-elastic materials, the phase lag δ is unequal $\pi/2$ and in case of rubber also depends on other influencing properties like temperature.

The response of a visco-elastic material to strain is in general described by the complex modulus of elasticity E^*. Following the derivation of [99], the resulting stress σ can be split into an elastic part (with $\delta = 0$) and a viscous part ($\delta = \frac{\pi}{2}$)[1].

$$\sigma(t) = \sigma_0 \sin(\omega_f t)\cos(\delta) + \sin(\delta)\cos(\omega_f t) = \epsilon_0 E' sin(\omega_f t) + \epsilon_0 E'' \cos(\omega_f t) \tag{2.8}$$

with

$$E' = \frac{\sigma_0}{\epsilon_0}\cos(\delta) \text{ and } E'' = \frac{\sigma_0}{\epsilon_0}\sin(\delta). \tag{2.9}$$

[1] Using the trigonometric addition formula $\sin(\alpha+\beta) = \sin(\alpha)\cos(\beta) + \cos(\alpha)\sin(\beta)$

E' and E'' in equation 2.9 are the storage modulus and the loss modulus, respectively. The storage modulus describes the energy stored during elastic deformation while the loss modulus corresponds to the energy converted into heat due to inner friction. This loss modulus contributes to the hysteresis friction. Using complex numbers, both moduli can be combined to the complex modulus using the definition of a complex number z.

$$z = a + ib = r(\cos(\delta) + i\sin(\delta)) = re^{i\delta} \tag{2.10}$$

In this equation a denotes the real part and b the imaginary part. In polar coordinates this can be reformulated using a distance from the origin $r = \sqrt{a^2 + b^2}$ and an angle δ. This representation fits the form of the E' and E'' in equation 2.9.

Therefore, strain and stress (equation 2.4 and equation 2.5) are reformulated using complex numbers.

$$\epsilon = \epsilon_0 e^{i\omega_f t} \qquad \sigma = \sigma_0 e^{i(\omega_f t+\delta)} \tag{2.11}$$

This results in

$$E^* = \frac{\sigma}{\epsilon} = \frac{\sigma_0}{\epsilon_0} e^{i\delta} = \frac{\sigma_0}{\epsilon_0}(\cos(\delta) + i\sin(\delta)) = E' + iE'' \tag{2.12}$$

Similar to the complex modulus E^*, a complex shear modulus $G^* = G' + iG''$ can be derived. The tangent of the phase angle can be calculated by equation 2.13 and is called loss factor.

$$\tan(\delta) = \frac{E''}{E'} \tag{2.13}$$

In the $\tan(\delta)(\omega_f)$-function the maximum value is one of the possible definitions of the glass transition temperature T_g [100]. This temperature describes the region of the transition between the rubbery state and the glassy state of the rubber. Figure 2.3 shows typical curves for the storage and loss moduli of a rubber compound. The significant change of the material behaviour between the rubber region and the glassy region is clearly visible.

In figure 2.3 a reference temperature is provided because the complex modulus changes not only with frequency, but also with temperature. This behaviour of rubber is called time-temperature superposition [101]. The dependency was first studied in experiments by Grosch [102], who measured the forces of a rubber block sliding over a glass surface at different (small) velocities and temperatures. He discovered that measurements conducted at different velocities and temperatures can be shifted so that all measurements form a curve. These curves are known as master curves. An empirical

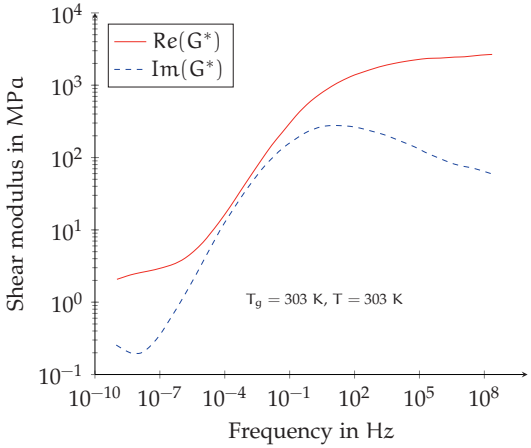

Figure 2.3: The real and the imaginary part of the shear modulus of polyisoprene rubber as a function of frequency for $T = 303\,K$ based on [84]

equation to calculate the shift factor has been found by Williams, Landel and Ferry [103] and is known as WLF equation 2.14. The empirical factors C_1 and C_2 can be determined using rubber porperty measurements at different temperatures.

$$\log(a_T) = \frac{-C_1(T - T_{ref})}{C_2 + (T - T_{ref})} \tag{2.14}$$

The complex modulus becomes

$$E^*(\omega_f, T) = E^*(a_T \omega_f, T, T_{ref}). \tag{2.15}$$

Another effect increasing the effort to model the complex modulus is named the Payne effect [104]. This effect is prevalent in filled rubber materials, which all modern tyres consist of. This effect describes a non-linear decrease in the loss modulus at large strain values.

In order to describe the rubber material properties, which influence the rubber friction, the complex modulus has to be measured in the correct temperature, frequency and strain range corresponding to the operating conditions of the tyre-rubber during normal driving conditions.

Rubber Friction

The two main phenomena generating the rubber friction are the hysteresis friction and the adhesion friction. In recent years, several friction theories to describe the interaction between the rubber and a randomly uneven road surface have been developed. Most noteworthy are the theories of Persson [84], and Heinrich and Klüppel [105]. Both theories are able to model the interaction between a rubber element sliding over an uneven surface, a comparison of these can be found in [106]. Persson has extended his initial published modelling approach to include effects like heating in the surface, which limits the generated friction potential. In addition, this theory provides an explanation for the friction potential loss on wet surfaces. Results using this theory have also been compared to friction potential measurement methods [107] similar to one described in section 1.2.1. Therefore, in the following sections, a short introduction to Persson's theory is given.

Hysteresis Friction The hysteresis friction is the friction generated by the small deformations of the rubber sliding over an uneven road surface. Road irregularities down to a few micrometers already influence the friction potential. The maximum hysteresis friction was found to be around the glass transition, depending on the temperature and the frequency, at the maximum of the loss factor [108].

According to [84], the dominating friction component for tyre-road friction is the hysteresis friction. This friction component strongly depends on the load, the surface roughness and the material properties of the rubber. While the relevant rubber properties have already been mentioned in section 2.1.2, Persson's theory models the elastic-deformation losses of the rubber while interacting with the surface. The modelling approach is based on the observation that the load on the rubber is usually not sufficient to deform the rubber in a way that it is in contact with the complete rough surface. Furthermore, Persson postulates that the deformation at each wave length is equally important for the hysteresis friction and therefore no wave length can be disregarded. Therefore, Persson derives an equation which describes the real contact area, when only considering unevenness down to a length scale λ and smooth beyond that value. Throughout the whole theory, this assumption is used by the introduction of a zoom factor ζ. The real contact surface fraction at a zoom $\zeta \geqslant 1$ is defined as equation 2.16, with A_0 defining the macroscopic contact area. This magnification factor can also be applied to the wave vector with $q = 2\pi/L_D$ defining the smallest wavelength and $q = q\zeta$ defining all larger wavelengths.

$$P(\zeta) = A(\lambda)/A(L_D),\ \lambda = L_D/\zeta, A(L) = A_0 \tag{2.16}$$

Persson describes the contact area calculating the pressure distribution and thus deformation of the rubber in vertical direction. The model assumes the rubber to be a linear elastic material and only considers the deformation along the z axis. This deformation depends on the elastic modulus of the rubber E', which itself is a function of the sliding velocity ν, and the pressure σ on the rubber. σ_0 is the average pressure over A_0. The pressure distribution at larger wavelengths depends on the power spectral density of the surface $C(\mathbf{q})$. The overall equation of Persson's model is given by equation 2.17, with Poisson's ratio ν of rubber around 0.5 and the introduction of a sliding direction ϕ.

$$P(\mathbf{q}) = \frac{2}{\pi}\int_0^\infty \frac{\sin(x)}{x}\exp(-x^2 G(\mathbf{q}))dx \tag{2.17}$$

$$G(\mathbf{q}) = \frac{1}{8}\int_{q_L}^{q} \mathbf{q}^3 C(\mathbf{q})\left(\int_0^{2\pi}\left|\frac{E(\mathbf{q}\nu\cos(\phi))}{(1-\nu^2)\sigma_0}\right|^2 d\phi\right) dq \tag{2.18}$$

At large magnifications, the real contact area approaches the value of zero but Persson postulates, that an earlier cut-off frequency should be used. This cut-off frequency is a parameter, which can depend on dirt particles on the road or rubber wear and is a free parameter of the model. The cut-off is typically at an unevenness of a few µm.

Finally, using the real area of contact and the rubber deformation, the resulting hysteresis friction according to Persson is given by

$$\mu = \frac{1}{2}\int_{q_L}^{q_1} \mathbf{q}^3 C(\mathbf{q}) P(\mathbf{q})\left[\int_0^{2\pi}\cos(\phi)\,\mathrm{Im}\left(\frac{E(\mathbf{q}\nu\cos(\phi))}{(1-\nu^2)\sigma_0}\right) d\phi\right] d\mathbf{q}. \tag{2.19}$$

Sharp [109] applied the rubber friction theory to the experiments of Grosch and found that the frequency of the friction potential can be replicated well by the theory. He attributes the discrepancy between the results of Grosch's experiments and the friction theory at slower speed to omission of the adhesion friction but also discovered, that for larger velocities the calculated friction decreases faster using the theory than seen in the experiments.

Large slipping velocities require inclusion of the heat generated in the contact area. The heat generation and dissipation has been included in an extension of this model derived in [110]. The temperature called flash temperature in this publication is the temperature arising inside the contact area due to a significant increase in local pres-

sure inside the contact area when viewed at larger magnification levels. The long-term increase inside the bulk of the rubber is not included in this model but can be included by assuming different background temperatures of the rubber and using the correct scaling of the complex modulus. The inclusion of the flash temperature does not lead to a closed form solution but an iterative method is required. Without the inclusion of the heat generation, the predicted friction potential rises to larger values for larger slip velocities. The heat generation limits the predicted friction potential.

The theory including the flash temperature has been applied by Ückermann [107] and compared to friction potential measurement with two devices. Most notably a device called ViaFriction was used, which uses the same measurement principle as the RoadSTAR truck. Although only a few surfaces have been evaluated and not the correct rubber properties were used, the model is able to predict the measured friction potential with good accuracy and a variance of only 0.02 is calculated. In order to reach these small errors, the cut-off frequency and background temperature had to be varied.

Adhesion Adhesion describes the molecular interaction between the rubber and the road. This interaction is the result of van der Waals forces. Based on the observations in Grosch's experiments, adhesion models, which show the same temperature-frequency superposition as the hysteresis friction, have been developed [111].

Lorenz [112] describes the process of adhesion by the elongation of the polymer chains. During the sliding of the rubber through van der Waals forces bound polymer chains get elongated until the attraction breaks due to the stress. This leads to a dissipation of the stored energy and the resulting adhesive force. The adhesive force is described as proportional to the real area of contact.

The peak of the adhesion friction is at lower sliding velocities than the hysteresis friction at the maximum of the loss modulus E" [108]. The adhesion friction follows a Gaussian distribution around this peak.

Tyre Construction

The tyre construction is a compromise between many design targets. Three of them are featured on the EU wet grip label [113]. These are the rolling resistance, the wet grip and the rolling noise but many others like tyre wear, velocity class or handling and comfort are also important. In order to optimise the different requirements, the properties of tyre rubber are modified with other chemicals and filler materials during the curing process. The two most common filler materials are carbon black and

silica [114].

The EU wet grip label is measured according to the previously introduced regulation [17]. The performance of the tyre is classified relative to measurements conducted with the SRTT by calculating the ratio G of the MFDD of the tyre divided by the MFDD of the SRTT. The performance range of different tyres can be observed by comparing the factors G of the different label classes. A tyre of the best category A has to perform more than 55 % better ($G \geqslant 1.55$) than the SRTT, while a tyre of the worst category F performes less than 9 % ($G \leqslant 1.09$) better than the SRTT resulting in a difference between the tyres of more than 40 %. Although the test surface and ambient conditions are closely defined in the test regulations, a new amendment [115] introduces correcting factors in the calculation of the factor G based on the reference surface friction potential either determined by the BPN or SRTT and the surface temperature. The introduced correction parameters differ for summer and winter tyres.

The internal tyre pressure influences the pressure distribution and size of the contact area. In modern vehicles, sensors monitor the internal tyre pressure and warn about a sudden pressure drop. Apart from a small pressure increase in the beginning of a drive due to heat up of the tyre, the tyre pressure can be assumed as constant.

Not only the rubber compound but also the tyre construction influences the tyre properties. In terms of friction potential especially on wet or snow surfaces, the tyre profile is important. The free volume created due to negative profile channels allows water to be transported away from the contact area. The profile of winter tyres often consists of many small sipes, which increase the contact area in snow conditions.

2.1.3 Intermediate Layer

The presence of an intermediate layer between the tyre and road can significantly reduce the friction potential. Only the most common type of an intermediate layer, an intermediate layer consisting of water, is discussed. Friction potential measurements on other contaminations are not that common but some values can be found in [116]. For example measurements on a road contaminated with engine oil led to a friction potential reduction of 36 % compared to a wet intermediate layer.

Rubber Friction on Wet Surfaces

The classic explanation of the friction potential reduction on wet surfaces is that the adhesion component vanishes as soon as the surface gets damp. In Persson's early friction theory, the high frequency cut-off due to dirt particles is larger than the contact

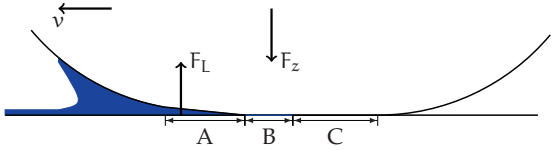

Figure 2.4: Sketch of the three zones concept of aquaplaning

distances required to form molecular bonds. Therefore, according to this theory, adhesion is negligible even on dry surfaces. The friction potential reduction between dry and wet surfaces is explained by another effect termed the sealing effect [117]. Water on the road gets trapped between the rubber and the smallest road asperities. Thus, the roughness spectral density is lowered, reducing the hysteresis friction. In addition, the water on the surface cools the rubber compound. Therefore, a lower bulk temperature should be used to calculate the friction potential. In a later publication, Persson also acknowledges an adhesion friction contribution on wet surfaces [85]. Thus, the friction potential reduction on wet surfaces can most likely be attributed to both a decreased adhesion and hysteresis friction.

Aquaplaning

A larger water layer on the road can lead to aquaplaning, which can lead to a complete loss of the friction potential. An early model often used is the three zone model [118, 119]. These three zones are visualised in figure 2.4. The inertia forces of the water form a bow wave in front of the tyre. If the velocity is high enough, the resulting water pressure forces lift the front of the contact patch. In this zone (A), the tyre is completely supported by the water and no road contact exists. In the second zone (B), some road asperities are in contact with the rubber and in the last zone (C) the tyre is in contact with the whole road surface. In the situation of full aquaplaning and complete loss of control only the first zone exists. If zone B and C are also present, this is usually called partial aquaplaning.

One of the most important variables influencing aquaplaning is the velocity. Therefore, a lot of effort has been invested to determine the aquaplaning speed. Horne [120] defined the point of aquaplaning as the speed v_{crit}, at which the wheel load F_z is in equilibrium with the lift force F_L.

$$F_z = F_L \tag{2.20}$$

This equilibrium has been calculated using a hydrostatic approach and resulted in equation 2.21, with p_i the tyre pressure, ρ the density of water and c_L a lift coefficient, which was empirically determined to be around 0.7. Early numerical models to calculate the aquaplaning phenomena have been developed in [121]. The author's calculations show a theoretical lift factor between 0.55 and 0.7, which confirms the experimental results.

$$v_{crit} = \sqrt{\frac{2p_i}{\rho c_L}} \tag{2.21}$$

Although Horne's equation does not depend on the water height, Horne noted that a minimum water height is required for aquaplaning to appear. The exact minimum water height is influenced by the tyre tread design and the surface roughness. The lowest water heights which supported aquaplaning were identified between 0.5 mm and 2.3 mm.

Yeager [122] describes the qualitative influence of several factors. According to Horne's equation, he describes that increasing the inflation pressure increases the aquaplaning velocity. He states that increasing the tyre load has a negligible influence on the aquaplaning speed. The largest influence on the aquaplaning speed according to Yeager has the thread design and the negative volume of the tyre profile.

An empirical equation incorporating several more influencing factors has been developed by Gallaway [123]. He uses another definition of aquaplaning, the spin-down of a free rolling tyre. This spin-down takes place because the center of lift is in front of the wheel center. Thus, a counter moment to the rolling resistance moment is generated, which brakes the wheel. A spin-down of 10 % is used in the emperical equation 2.22. In this equation, SD is the spin-down in %, p_i the pressure in kPa and TD the profile depth in mm. The value for A is calculated according to equation 2.23, which introduces a dependency of the critical velocity on the water depth *WD* in cm and the surface texture TXD in cm.

$$v_{crit} = 0.2506 SD^{0.04} {p_i}^{0.3} \left(\frac{TD}{0.794} + 1\right)^{0.06} A \tag{2.22}$$

$$A = max\left(\frac{11.08}{WD^{0.06}} + 3.507, \frac{26.871}{WD^{0.06} - 6.861} TXD^{0.14}\right) \tag{2.23}$$

Horne concluded that there is no exact relation between the spin-down of a free-

rolling tyre and the critical speed according to his definition. He stated, that the 10 % spin-down can appear in a range between 80 % and 120 % of this velocity. Further empirical equations and experimental results are summarised in [124].

While Gallaway's equation includes most influencing factors, the equation is only a fitting to experimental results. In recent years, several researchers conducted detailed fluid-structure interaction finite element method simulations to understand the hydroplaning phenomena [125, 126]. The results show that the thread profile can significantly reduce the hydrodynamic pressure and increase the aquaplaning speed. Thus, the previously cited equations should only be used as a rough estimate.

Snow

On snow, the tyre profile is one of the most important influencing factors. The small sipes in the profile block allow an indentation of the snow surface and ploughing. In a series of laboratory measurements presented in [127], the effect of the rubber compound and profile geometry was evaluated. The friction potential value on hard packed snow was measured between 0.3 and 0.6. The slip-stiffness of the tyre is limited by the shear forces transmittable through shearing of the snow layer. If the temperature is close to the freezing point or a large sliding velocity is applied, a small water layer is formed between the tyre and snow surface, which significantly reduces the friction potential.

Ice

On ice, the hysteresis friction is the main contribution to the friction potential. Due to its smooth surface, the roughness of the rubber block is important. This has for example been included in the modelling of ice friction according to Persson's friction theory in [128]. The rubber block sliding over the ice surface results in heating and local melting of the surface, which results in a small viscous force component but also polishes the ice surface further reducing the hysteresis friction. The local melting depends on the sliding velocity and surface temperature. A relationship of both factors has beeen analysed in [129]. The laboratory experiments show that in very cold conditions, no melting takes place and a 'dry' contact patch is possible, which leads to friction potential values of above 0.7. As soon as the temperature approaches the melting point, the experiments resulted in friction potential values between 0.14 and 0.366.

2.1.4 Vehicle

The vehicle influences the usable tyre friction with many properties. The vehicle load influences the pressure in the contact patches of the tyres. The centre of gravity determines the load transfer during accelerations. Because of the degressive load influence, both factors change the at maximum possible friction potential. The suspension kinematics of the vehicle change the operating point of the tyre by applying camber or toe angles. This changes the pressure distribution inside the contact patch and thus the friction potential.

The largest influencing factor is the calibration of the ESC. The setup of the vehicle determines, which vehicle side-slip values and wheel slips are deemed safe. If these boundaries are violated, the ESC limits the vehicle capabilities by braking single wheels, reducing the engine torque or steering interventions.

2.2 Tyre Models

Persson has developed a two dimensional tyre model [130] which includes his complete friction theory but in general the required rubber properties and road unevenness are not available and the increased accuracy is not required. In vehicle dynamic applications (like many of the approaches presented in section 1.2.2), simpler tyre models are preferred. Many different models are used and a detailed introduction is out of the scope of this thesis. Instead, a short introduction to the magic formula and brush tyre model is presented and the influence of different friction potential values on these models is derived.

Commonly, two auxiliary quantities are used in tyre models, the effective rolling radius r_e and the longitudinal slip κ. The tyre radii are visualised in figure 2.5. Radius r_0 is the unloaded radius of the tyre, and r_L the loaded radius of the tyre. Typically, $r_L < r_e < r_0$.

There are many different definitions for the longitudinal slip κ, which can easily be translated into each other. Throughout this thesis the definition

$$\kappa = \frac{\omega r_e - v}{v} \tag{2.24}$$

is used, where v is the velocity of the wheel center and ω is the rotational velocity around the y-axis of the tyre. Using this definition, a fully locked tyre has $\kappa = -1$ and a spinning tyre has $\kappa = +\inf$. The effective radius is chosen so that a free rolling tyre has a slip value of 0. The effective radius is also the lever arm for the transmitted

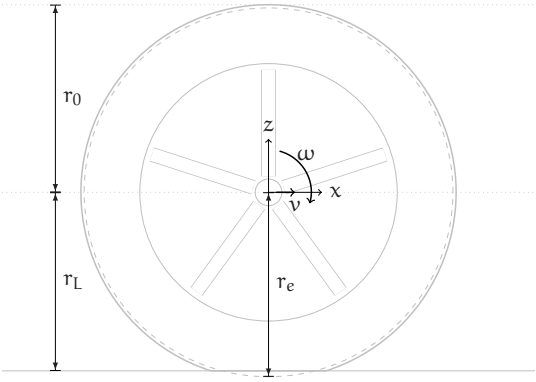

Figure 2.5: Definition of tyre radii

torque [131].

$$\alpha = \frac{v_y}{v_x} \tag{2.25}$$

Similar to the longitudinal slip κ, in lateral direction the slip angle α can be used. The combinations between longitudinal and lateral slip define approximately a friction potential circle or ellipse. In reality, combined slip conditions can transfer less forces than lateral or longitudinal slip seperately.

The magic formula model is an empirical tyre model initially developed at Delft University [132]. Its basic form can be described by equation 2.26.

$$F_x = D_{MF} \sin(C_{MF} \arctan(B_{MF}\kappa - E_{MF}(B_{MF}\kappa - \arctan(B_{MF}\kappa)))) \tag{2.26}$$

It can clearly be seen, that the parameter D_{MF} determines the maximum transferable forces. As approximation, D_{MF} can be substituted with $\mu_{pot} F_z$. The tyre stiffness (slope at $\kappa = 0$) can be calculated by $B_{MF} \times C_{MF} \times D_{MF}$. This would indicate, that the initial slope scales with the friction potential (if only the factor D_{MF} is scaled), which is an important observation. This will be of further importance throughout the next chapter. In current versions of the magic formula model the parameters B_{MF}, C_{MF}, D_{MF}, E_{MF} themselves are calculated using more than 100 parameters to account for the wheel operating conditions [133]. This model allows an exact replication of test bench measurements.

In contrast to the empirical magic formula, the brush tyre model is a simple physics

based tyre model. There are many different extensions of the brush tyre model available in literature [134, 135]. In the simplest version, the carcass of the tyre is assumed as a rigid belt, which is connected to the road by a series of brushes. This is visualised in figure 2.6. The carcass moves with a velocity of ωr_e in positive ξ direction, while the road contact moves with a velocity of v. A brush entering the contact area at $\xi = 0$ is undeformed. Due to the different velocity of the road and the carcass, the spring starts to deform over time.

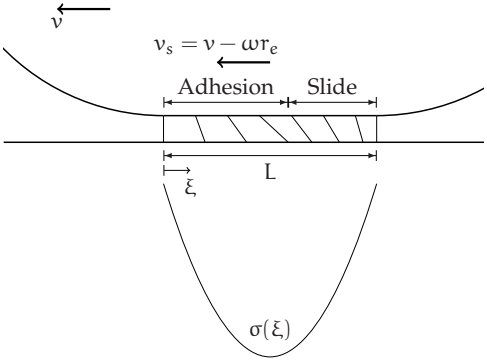

Figure 2.6: Brush tyre model

$$d(\xi) = (\omega r_e - v)t(\xi) = \frac{\omega r_e - v}{\omega r_e}\xi = \frac{\kappa}{1+\kappa}\xi. \tag{2.27}$$

If the friction force of the spring reaches the adhesion limit ($\mu_{adh}\sigma(\xi)$), it starts sliding, transferring the maximal possible sliding friction ($\mu_{slide}\sigma(\xi)$). Normally, a parabolic pressure distribution along the contact area is assumed (see equation 2.28).

$$\sigma(\xi) = \frac{3F_z}{2LW}\left[1 - \left(\frac{0.5L - \xi}{0.5L}\right)^2\right] \tag{2.28}$$

The point ξ_{slide}, where the rubber contact starts sliding, can now be calculated by solving equation 2.29, where k is the stiffness of the brushes. This results in the solution 2.30.

$$\begin{aligned} kd(\xi_{slide}) &= \mu_{adh}\sigma(\xi_{slide}),\ \text{if}\ \kappa >= 0 \\ kd(\xi_{slide}) &= -\mu_{adh}\sigma(\xi_{slide}),\ \text{if}\ \kappa < 0 \end{aligned} \tag{2.29}$$

$$\xi_{slide} = max\left(0, L - \frac{k\left(\frac{\kappa}{\kappa+1}\right)L^2}{4\mu_{adh}\sigma_0}\right) \tag{2.30}$$

Finally, the overall tyre friction for slip values, where not the whole contact area is sliding ($\xi_{slide} > 0$), can be calculated by equation 2.31 and otherwise $F_x = \mu_{slide}F_z$.

$$\begin{aligned} F_x(\kappa) &= W\int_0^{\xi_{slide}} kd(\xi)d\xi + W\int_{\xi_{slide}}^{L} \mu_{slide}\sigma(\xi)d\xi = \\ &= W\left[\frac{kL^2}{2}\left(\frac{\kappa}{\kappa+1}\right) - \frac{k^2L^3}{4\mu_{adh}\sigma_0}\left(\frac{\kappa}{\kappa+1}\right)^2 + \frac{k^3L^4}{32\mu_{adh}^2\sigma_0^2}\left(\frac{\kappa}{\kappa+1}\right)^3\right] \\ &\pm W\mu_{slide}\left[\frac{k^2L^3}{8\mu_{adh}^2\sigma_0}\left(\frac{\kappa}{\kappa+1}\right)^2 - \frac{k^3L^4}{48\mu_{adh}^3\sigma_0^2}\left(\frac{\kappa}{\kappa+1}\right)^3\right] \end{aligned} \tag{2.31}$$

The tyre stiffness of the brush tyre model can be calculated by $0.5kL^2W$, which indicates that this model does not predict any dependence of the tyre stiffness on the friction potential.

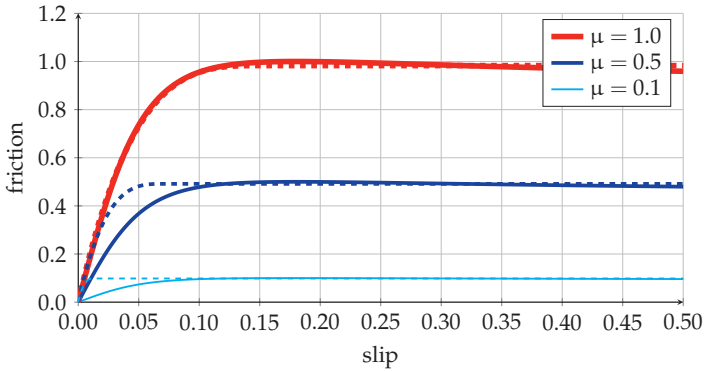

Figure 2.7: Typical tyre force curves for different friction potential values generated with the magic formula (solid lines) and brush tyre model (dashed lines)

Figure 2.7 shows tyre curves of both models for different friction potential values.

Both models have been fitted to match for $\mu_{pot} = 1$. For the other friction potential values, the factor D_{MF} of the magic formula model and the parameters μ_{slide} and μ_{adh} of the brush tyre model have been scaled. The ratio between μ_{slide} and μ_{adh} has been kept constant. It can be seen that both tyre models suggest a different dependency on the friction potential. The required model parameters are derived using test bench measurements [136], which are conducted on test benches and are usually conducted on a dry safety walk. Adapting the parameters to other road conditions would require measurements using these conditions, which cannot be achieved in most test benches. Instead of only changing the parameter D_{MF}, by also scaling B_{MF} and C_{MF}, the magic formula model can replicate the same constant slip stiffness behaviour as the brush tyre model.

3 Development of a Friction Potential Measurement Method

In this chapter, a new method to measure the friction potential using a test vehicle is developed. The idea behind this method is to reduce the deceleration of the vehicle by only braking one wheel for a limited time instead of braking all four wheels in a full braking test. This method will be called Single Wheel Braking (SWB) in the following chapters. Since every wheel supports about one quarter of the vehicle mass, only around a quarter of the maximal possible deceleration is reached while one wheel is reaching the friction potential. After a short description of the test vehicle and the used software and sensors, it is shown by simulation and tests on a proving ground that this method is safe to use on public roads. The proving ground Single Wheel Braking (SWB) tests are compared to full braking tests and a correlation between both measurement methods is derived.

After the qualification of the SWB method, a larger friction potential study on public roads was conducted. The SWB tests were triggered based on the Global Navigation Satellite System (GNSS) position, so that repeated measurements on 74 points around a short representative route were possible. The results of this study are presented in section 3.3 and used to discuss the observed influence of different factors.

3.1 Test Vehicle

The test vehicle used throughout the measurements described in this thesis is an all-wheel drive Mercedes S-Class equipped with several extra sensors shown in figure 3.1. The vehicle's ESC unit was programmed with a special custom software, which allowed requesting brake torques on each wheel separately via a Controller Area Network (CAN) message. If the requested brake torque surpasses the friction potential, the wheel is still ABS-controlled.

The special CAN messages are sent from a DSpace Microautobox, which in combination with a measurement computer and the software ControlDesk is also used for

Figure 3.1: Test vehicle used for SWB measurements

the visualisation of current sensor values. All series vehicle communication busses and measurement busses are recorded on a logger and converted to .mat-files, which were then analysed in Matlab.

During the test campaign, the vehicle had been equipped with four wheel-force measurement wheels produced by Kistler. These wheels use four 3D load cells which measure the applied forces along three orthogonal directions. A 360 ticks-per-rotation wheel-tick sensor fitted to a stator part is used to transform these forces into the vehicle coordinate system. This calculation is done on the measurement control unit. This way, all three forces and moments acting on each wheel and the wheel rotation speed are measured. In addition, the vehicle has been fitted with four brake pressure sensors measuring the brake pressure in each brake cylinder. A differential GNSS, which is coupled with a high precision 6D inertial measurement unit, is used to automatically trigger measurements and to measure the vehicle accelerations and velocity. This system allows a localisation of the vehicle with an accuracy of less than 0.02 m with optimal GNSS signal and usually less than 1 m deviation during all measurements on public roads.

For additional sensors used to classify the intermediate layer, the vehicle has been equipped with a modified bike rack. The bike rack has been fitted with two MARWIS sensors produced by Lufft Gmbh. These sensors measure the road surface temperature, dew point and classify the road condition via infrared-spectroscopy. The sensor also provides information about the water height and the ice content. The results of these sensors are discussed and used in section 5.2.

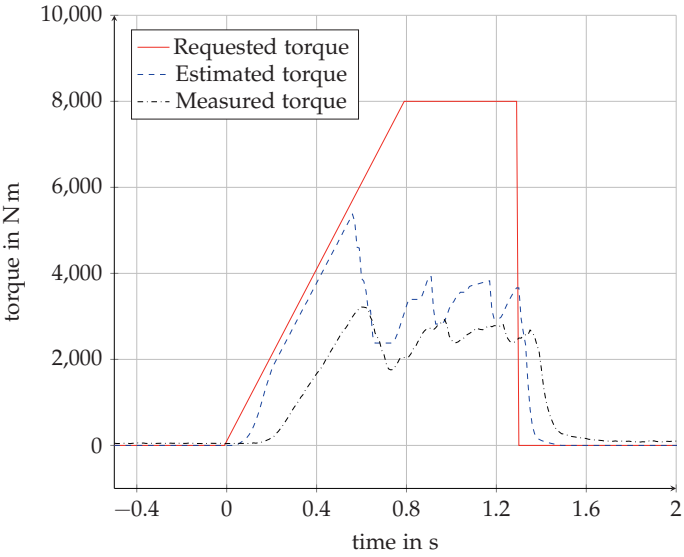

Figure 3.2: Requested, estimated and measured wheel torque during a single wheel braking test

3.2 Measurement Method - Single Wheel Braking

The idea of the single wheel braking test is to brake one wheel of the vehicle until the friction potential is reached. The brake torque is increased linearly until a theoretical brake torque of 8000 N m is reached. After the maximum is reached, the brake torque is kept constant for 0.5 s, after which the requested brake torque is set to 0 N m again. The actual set brake torque differs from the requested brake torque significantly, since the ESC is not calibrated for these kinds of brake torque requests on one wheel and because the actual transfer factor between the brake pressure and the brake torque can differ depending on factors like the brake pad conditions or temperature. The real brake torque applied is measured using the force measurement wheels. The requested, internally by the ESC estimated and measured brake torque of a single wheel brake test can be seen in figure 3.2. The delay of the measured torque and the estimated torque is caused by the internal filter of the force measurement wheels. This delay of around 0.07 s is corrected in all subsequent plots.

During all measurements, the chosen wheel for SWB was the front right wheel. The

right hand side of the vehicle was chosen because the continuous measurement methods SKM and RoadSTAR also measure the friction potential in the right wheel track. The front wheel was the preferred choice because on wet roads, the front wheels displace water so that the rear wheels might have better friction potential values. Selecting between braking a front wheel or a rear wheel is also a trade-off between stability and controllability. Braking the front wheel reduces the steerability of the vehicle, while braking a rear wheel would reduce the stability. Braking either the front or rear wheel, a yaw moment is introduced which needs to be corrected by the driver.

3.2.1 Safety Considerations

In order to use the SWB method on public roads, the safety of this method has to be guaranteed. In order to show, that a trained driver can keep the vehicle on the road in a first step, several simulations have been conducted. The SWB tests have been simulated using a simple horizontal two track vehicle model. Weight transfer between the wheels due to longitudinal or lateral accelerations is included, but no body roll or pitch. A constant steering-ratio between the steering-wheel and both front wheels is assumed. The parameters of the vehicle model have been fitted to the test vehicle. A magic formula model derived from test bench measurements has been used to calculate the tyre forces. All model equations can be found in Appendix A.

As no ABS-controller has been implemented in the simulation, the brake torque request will always lead to a completely locked wheel. The consequences of this simplifications lead to two inaccuracies. First, the generated yaw moment is underestimated since a locked tyre is unable to utilise the friction potential. Second, the locked tyre cannot transfer lateral force, which leads to an overestimation of the yaw moment. Also no suspension compliance is considered in the simulation. Therefore, it is expected that the real yaw moment will be lower than the simulated one. Thus the simulation should provide a safe approximation.

In the first simulations, the steering wheel input has been fixed to zero degrees and the lateral offset and heading error at the point the requested brake moment is set back to zero has been analysed. These results can be seen in figure 3.3. As expected, both the y-offset and the heading error increase with increasing velocity. It can be seen that, while for slower velocities, the errors are negligible, especially for highway velocities resulting trajectory errors are too large to stay inside the driving lane. At a speed of 30 kph, the y-offset is only 0.17 m and the heading error about 2°. At speeds of 80 kph, the y-offset reaches over 1 m and the heading error is around 6°. These values are too large to conduct tests on public roads. Thus, it has to be accessed if

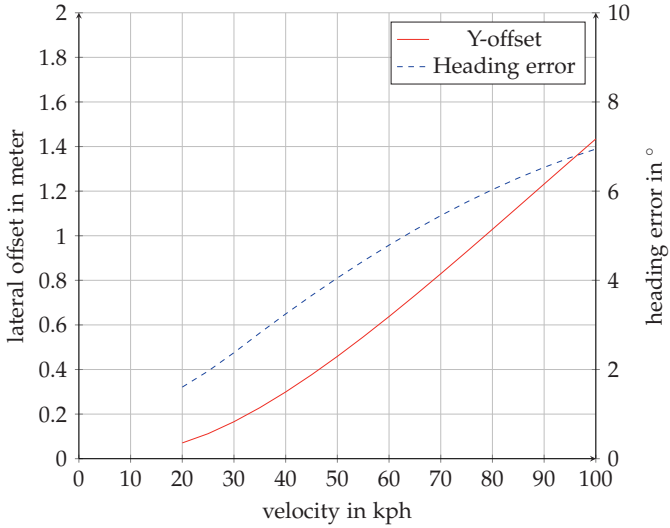

Figure 3.3: Y-offset and heading error resulting from a SWB test with fixed steering wheel over velocity

a trained safety driver can correct this offset. Therefore, a lateral Linear Quadratic Regulator (LQR) as proposed by Odhams [137] has been used to simulate the driver input. The controller inputs are the lateral velocity, yaw rate and predicted y-offset at equidistant points up to 4 s into the future[1]. In addition, the controller uses an input delay. This delay and all gain parameters have been derived by Odhams using a simulator study, in which the test subjects needed to follow a random road. This means the controller is optimised for path-following and not for disturbance control, which would better present the application of a SWB. The controller was chosen because it is easy to implement and all gain parameters were provided and derived from human drivers. Figure 3.4 (left) shows a comparison between the y-offset with controller and with fixed wheel at 80 kph and $\mu_{pot} = 1.0$. The idealised SWB torque is applied at about 44 m after 2 s of simulated straight line driving. This is shown at 0 m in the figure. The plot shows clearly that the modeled driver is able to decrease the lateral offset down to 0.34 m. Since a motorway lane has a specified width of 3.50 m in Germany and a vehicle has a width of about 2 m, a margin of about 0.75 m is available to either side. Thus, the reduction in y-offset is enough to stay inside the lane boundaries by some

[1]The parametrised controller only uses about 2 s of preview points.

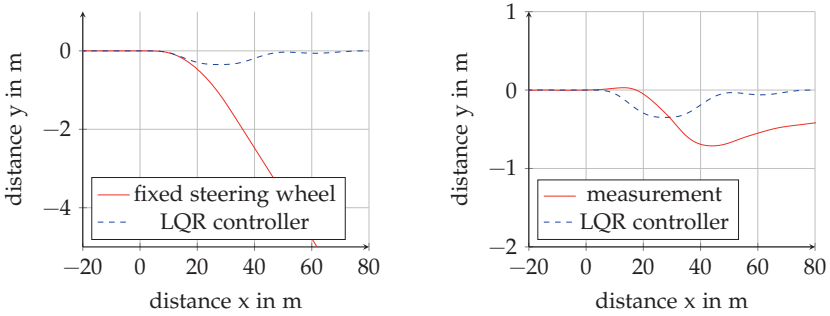

Figure 3.4: X-Y-trace comparison between SWB with fixed steering wheel and LQR controller (left) and between LQR controller and measurement (right)

margin. The at maximum required steering angle is only 32°, which leaves the driver with enough margin to correct additional disturbances.

In a next step, SWB tests have been conducted on several proving grounds to prove, that a real driver can also reduce the lateral deviation enough and establish a correlation between SWB measurements and the correct friction potential. Figure 3.4 (right) shows a comparison between a simulated SWB test and a real SWB test measurement at around 80 kph. The driver was able to keep the vehicle inside the lane during more than 140 tests conducted on different surfaces with varying friction potential and starting velocities. Since the objective of the human driver is always to stay inside the lane and not to follow the center line exactly, the remaining error is never corrected.

The velocity difference between the start and the end of the simulated SWB brake is 11 kph and the peak deceleration about $3.5\,\mathrm{m\,s^{-2}}$. This still is a high deceleration compared to the acceleration experienced during normal driving[2]. Nevertheless, human drivers are more used to these decelerations and therefore can react to it accordingly if required. Due to the minimal velocity change, the influence on following traffic is minimal. In order to conduct measurements on public roads, additional safety measures have been implemented. First of all, the SWB test can only be activated, if the GNSS reception is good. This prevents unexpected SWB events for the driver. On top of that, the driver has to keep a steering wheel button pressed all the time. As soon as he stops pressing this button, the brake moment request is set back to 0 N m. Therefore, the driver can control the activation of the SWB and is able to cancel the applied brake moment at any time.

[2] see section 6.1

3.2.2 Measurement Data Processing

During SWB tests, the moment balance in equation 3.1 should be fulfilled. The brake moment M_{brk}, the brake force ${F_x}^{dyn}$ and the wheel acceleration $\dot{\omega}$ are measured by the force measurement wheels. The wheel acceleration is calculated by differentiating the wheel rotation velocity measurement. The moment arm, the effective radius, has been determined during a coast down test. The inertia I_{yy} has been fitted to available data. Nevertheless, it was discovered that, without additional corrections, a systematic error which increases with increasing brake moment, exists.

$$I_{yy}\dot{\omega} = M_{brk} - {F_x}^{dyn} r_e \tag{3.1}$$

The reason of this problem was found in an elasto-kinematic rotation in the suspension due to the applied brake force. This twisting suspension also rotates the wheel tick sensor of the measurement wheels. Thus, the normal direction of the wheel coordinate system is no longer parallel to the gravity vector. This is sketched in figure 3.5. The amount of this twist has been estimated by locking one wheel and slowly accelerating until the locked wheel starts sliding. The measured wheel load during this test is shown in figure 3.6. Another possible method to derive the suspension twist is by optimising ${F_x}^{dyn}$ in equation 3.1.

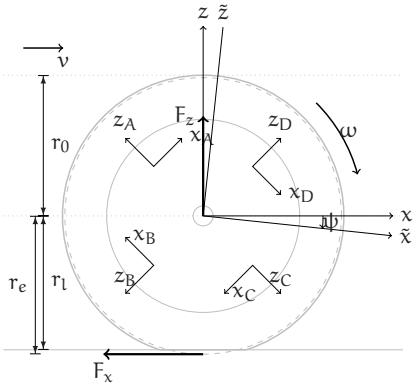

Figure 3.5: Measurement wheel schematic during SWB measurement

The corrected measurements are calculated by

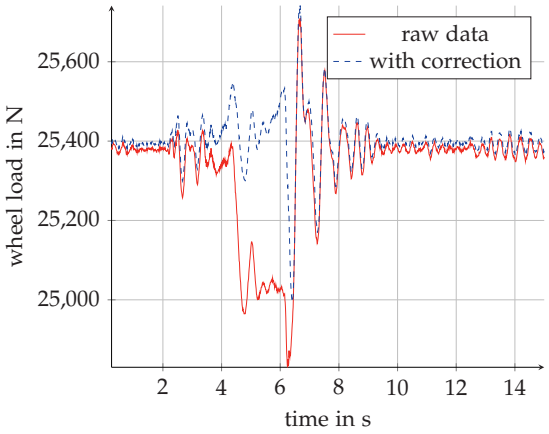

Figure 3.6: Effect of the suspension twist correction

$$\begin{pmatrix} F_x \\ F_z \end{pmatrix}_{\text{corrected}} = \begin{pmatrix} \cos(\psi) & -\sin(\psi) \\ \sin(\psi) & \cos(\psi) \end{pmatrix} \begin{pmatrix} F_x \\ F_z \end{pmatrix} \tag{3.2}$$

where the rotation angle ψ is modeled as a function of the measured torque. An approximation of the suspension as linear torsion spring proved sufficient. The rotational stiffness c_{rot} has been fitted so that during the measurement plotted in figure 3.6 the measured vehicle mass remained approximately constant. In [138] the effect of applying the correction to ${F_x}^{dyn}$ in equation 3.1 has been shown. The same value of c_{rot} provides reasonable results for both experiments. Thus, it is applied to all further results. Applying the correction reduces the measured friction potential.

$$\psi = f(M_{brk}) = \frac{1}{c_{rot}} M_{brk} \tag{3.3}$$

Other factors, which are not measured, also influence the tyre curves. First of all, as reference velocity, the speed of the left front wheel is used with the assumption that this wheel is rolling freely. Due to the four-wheel drive vehicle this is not exactly true. Second, the suspension of the left wheel not only twists the suspension but also pushes the suspension back as soon as brake force is applied. A third effect is the dynamic tyre behavior, which leads to a delay between the slip and the build up of the corresponding static tyre forces. The force measurement wheels determine the slip of the rim κ_{rim} but measure the dynamic force of the tyre ${F_x}^{dyn}$. For single point

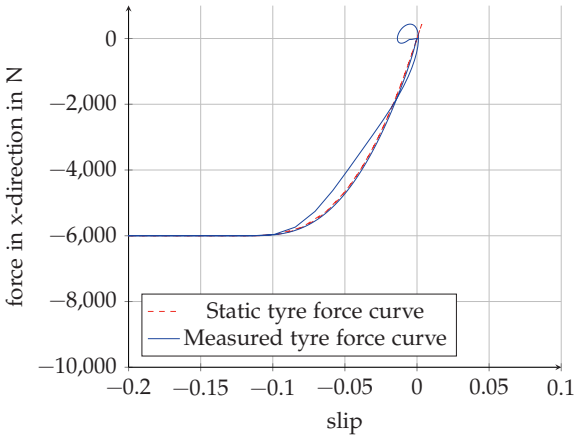

Figure 3.7: Simulation of effect of neglecting transient tyre behaviour and suspension deformation

contact models like the simple models described in section 2.2, the concept of the relaxation length has been proven sufficient to model the dynamic behavior. Different models for the calculation of the relaxation length exist, e.g. four different models are discussed in [133]. A mathematical derivation for a first-order transient tyre model can be found in [139]. The concept of this model is to model the road contact of the wheel via a spring and shock-absorber. A simulation using the fully-transient tyre model described in [133] and including the suspension deformation has been used to show the effect. This is plotted in figure 3.7. The static tyre curve used for the simulation is plotted as reference. The simulated 'measurement' curve using the force measurement wheels shows the hysteresis due to the dynamic tyre behavior. The main deviation from the static tyre curve only appears after the locked wheel is released again. It was determined that during the pressure build-up until the ABS operation starts this can be neglected.

In order to measure different friction potential values, special brake test courses on a proving ground have been used to generate the tyre curves. Altogether, repeated tests on four different surfaces were planned, an asphalt, a concrete and a cobblestone road. In addition, epoxy tiles of low friction potential have been used. All surfaces except the epoxy tiles can be used in dry and wet conditions. The epoxy tiles can only be used in wet conditions. Therefore, altogether seven different tyre curves can be generated from the measurement data.

Table 3.1: Friction potential on test track surfaces according to tyre perspective

Surface	Intermediate Layer	μ_{pot}
Concrete	dry	1.22
Concrete	wet	0.67
Asphalt	dry	1.02
Asphalt	wet	0.92
Cobblestone	dry	0.77
Cobblestone	wet	0.36
Tile	wet	0.06

Due to cloudy weather conditions, the cobblestone road did not dry on time. Therefore, for the combination dry/cobblestone similar measurements, conducted earlier during the development of the SWB test, were used. The main difference during these tests was that the maximum prescribed brake torque was only set to 4000 N m. Later, it was discovered that due to the poor estimation of the real brake torque, this torque was not high enough to guarantee ABS operation on all surfaces. Although the car was fitted with the same tyres, these were worn further down in the second measurement campaign. The profile depth was measured about 6 mm in the first measurement series compared to 4 mm in the second. Also the first measurements were conducted during significantly hotter temperatures.

The aim of the measurements was to get ten repeated measurements on each surface. Due to technical problems during some measurements and general time constraints, this number of repetitions has not been achieved for every surface. All results are plotted in figure B.1. Measurement values from the start of the brake torque request until the ABS controller started reducing the brake pressure in the front right wheel are used in these curves. For these tests, the data of the measurement wheels was logged with 200 Hz. The measured friction potential values according to the tyre perspective can be found in table 3.1. The largest friction potential was measured on dry concrete, while the wet tiles allow almost no force transfer. Thus, the whole range of possible friction potential values is covered by the surfaces.

In section 1.2.2, it was found that many methods postulate a relationship between the slip-stiffness of the tyre and the friction potential. The SWB measurements can now be used to gain further insight, if this is a viable estimation strategy. Figure 3.8 shows the conducted steps to fit the brush tyre and the magic formula tyre model to the measured slip-force curves. Figure 3.8 (top left) shows the raw data of all measurements conducted on the concrete surface. It is apparent that the slope of the curves is

alike. Instead of the linear relationship, the curves have a small dent near the origin, which is most likely due to the applied filtering in the rotational velocity and force measurement channels. In a first step, a linear tyre model has been fitted according to equation 1.11. The dent and the non-linear part of the slip-force curve have been excluded from the fitting process by only using slip-force measurement points which fulfil the requirement that the measured force is between 20 % and 45 % of the maximal measured force. The results of this fitting can be seen in figure 3.8 (bottom left). The estimated slope of the surfaces concrete and asphalt is almost the same. Due to the small friction potential, not enough measurement points to fit a straight are available for the tile surface. The cobblestone measurements show a smaller slip-stiffness than concrete and asphalt. On this surface, the wet road condition also leads to a visibly lower slip stiffness than the dry road condition. A reason for this behaviour could be the very uneven stress distribution in the contact area. The size of the cobblestones is smaller than the contact length of the tyre L, thus the parabolic stress distribution assumption which was used in the simple brush tyre model is not valid anymore. Inside the contact area, there could be many transitions from adhesion to sliding regions, which increase in number as the adhesion friction decreases.

In figure 3.8 (top right), the two tyre models brush tyre and magic formula are fitted to the raw data of the measurements on dry concrete. Since only the data until the ABS-controller activation has been used to fit the tyre curves, no data of the sliding friction is available. Therefore, in case of the brush tyre model it was assumed that μ_{slide} equals μ_{adh}. This simplification has also been used in [134]. The geometric parameters L and W have been set to constant values of $\mathrm{L} = 0.3\,\mathrm{m}$ and $W = 0.25\,\mathrm{m}$ respectively. The change of contact area with increasing load has been neglected. The friction potential was found using the median of the maximum measured value of all measurements and the brush stiffness was adopted that it fits the linear tyre model. Therefore, all parameters of the model were found analytically.

A similar process has been used to fit the magic formula parameters $\mathrm{B_{MF}}$, $\mathrm{C_{MF}}$, $\mathrm{D_{MF}}$, $\mathrm{E_{MF}}$. $\mathrm{D_{MF}}$ was set to the median of the maximal measured value of all measurements. $\mathrm{C_{MF}}$ determines the friction value of the locked wheel. Since no information about this operating conditions is available it was assumed to be 90 % and the value of $\mathrm{C_{MF}}$ was calculated according to [140]. Factor $\mathrm{B_{MF}}$ was chosen so that the initial slip-stiffness fitted the linear tyre model. Finally, the last parameter $\mathrm{E_{MF}}$ has been optimised so that the peak of the tyre force curve is at the correct slip value. The results of this fitting process for all surfaces can be seen in figure 3.8 (bottom right). It can be concluded, that the measurements on the test track do not show a clear relationship between the initial slip-stiffness and the friction potential. A distinction between the tyre curves at

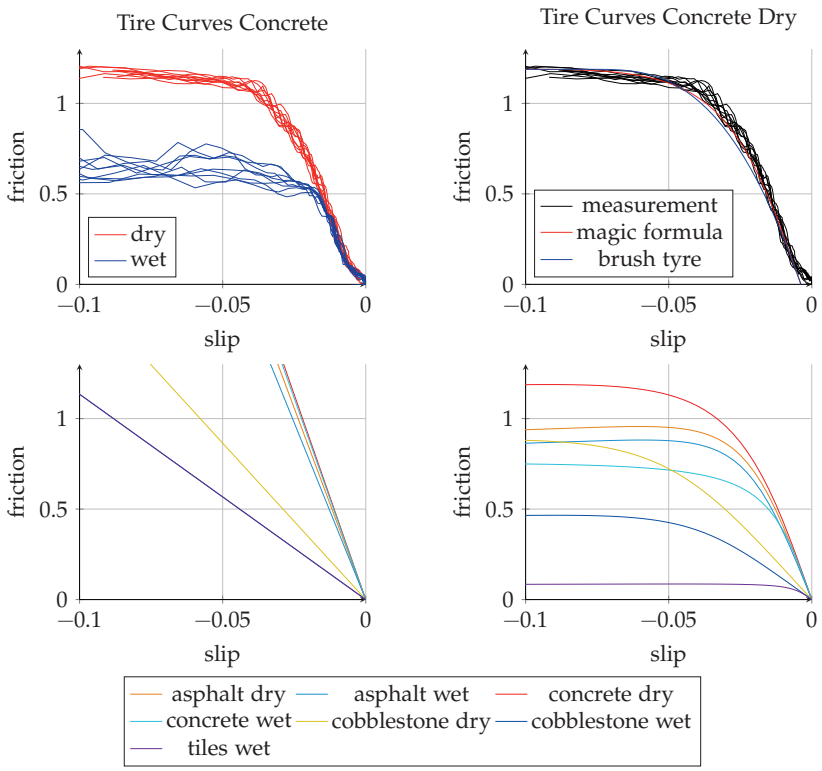

Figure 3.8: Process of fitting tyre models to measurement data on the different test track surfaces; top left: comparison of raw measurement data on dry and wet concrete; top right: fitted magic formula and brush tyre model to measurement data of concrete dry; bottom left: fitted linear tyre model for all surfaces; bottom right: fitted magic formula model for all surfaces

a typically low slip value seems difficult even if force measurement wheels are used. It has to be noted, that in a customer vehicle neither the correct longitudinal force nor the wheel load are available. The slip calculation suffers from a coarse resolution and slower update rate. In addition, during normal driving, only a very small part of the tyre force-curve is measured, which does not allow to fit a non-linear tyre model. Therefore, based on the measurements conducted on the proving ground slip-slope based methods cannot estimate the friction potential during normal driving situations. In case of a larger friction usage, these methods can still contribute as an early warning

just before the whole friction potential is utilised.

3.2.3 Comparison with Full Braking Measurements

Since the objective of the SWB was to find replacement for full braking measurements before each block of the SWB measurement tests, a number of full braking tests on the same surfaces has been conducted. Instead of using one of the intervals found in literature and plotted in figure 1.5, an additional interval, which averages the acceleration starting at the point the ABS controller starts to reduce brake pressure at one of the wheels until standstill has been used. This interval is also included in figure 1.5. For future reference this interval has been called Mean Acceleration to Standstill (MASS). The interval has been chosen because the full braking tests were initiated by a human driver. In future, this will be taken over by the autonomous system. Therefore, the pressure build-up phase will change and is excluded in this evaluation interval.

The initial speed was always set around 80 kph. Again, it was aimed to measure ten repetitions on each surface but this number was, due to similar reasons as mentioned for the SWB tests, not always reached. The results of all full braking tests are plotted in figure B.2. It has to be noted that similar to the SWB tests, the full braking measurements on dry cobblestone of an earlier test day had to be used since the cobblestone surface did not dry up on time for the measurements on the same day. The measurement intervals cannot be evaluated for the braking tests on the wet tiles because the reached deceleration was not enough to stop on the surface. The deceleration a_{3s} in the first three seconds after the ABS started are used as friction potential. The resulting values evaluated in the intervals introduced in section 1.2.1 are summarised in table 3.2. As expected, the interval a_{mean} results in the lowest friction potential values, because the pressure build-up phase and the stopping phase of the full braking test are included in this interval. The difference between a_{mass} and a_{mffd} is mostly marginal.

The interval a_{mass} was used to find a correlation with the SWB tests. The highest decelerations were achieved on the dry concrete surface with a friction potential around 1. On wet concrete, the calculated friction potential values are about 10 % lower. It is peculiar that the reached deceleration increases over time until it reaches values similar to the deceleration on dry surfaces. Therefore, the calculated friction potential in the interval a_{mean} is significantly lower than the one calculated in the other intervals. The reason of this slowly increasing friction potential is unknown. Possible explanations are that at the starting speeds partial aquaplaning decreases the available friction potential or that it is due to the ABS algorithm. It has to be noted that the SWB tests on wet concrete led to friction potential measurements similar to those measured at the

Table 3.2: Full braking test results

Surface	Intermediate Layer	a_{mean}	a_{mffd}	a_{mass}	a_{3s}
Concrete	dry	0.97	1.01	1.02	-
Concrete	wet	0.9	0.96	0.94	-
Asphalt	dry	0.85	0.89	0.89	-
Asphalt	wet	0.76	0.77	0.79	-
Cobblestone	dry	0.89	0.92	0.93	-
Cobblestone	wet	0.40	0.42	0.41	-
Tile	wet	-	-	-	0.08

beginning of the full braking tests. Dry asphalt and dry cobblestone led to very similar results with friction potential values around 0.9. While on the wet asphalt, the friction potential only decreases to values slightly below 0.8, on wet cobblestone the friction potential decreased to less than half its dry values with a remaining friction potential marginally above 0.4.

In the previous section, the results of the SWB tests have been presented. The evaluation of the tests focused on the tyre perspective. The ABS controller cannot control all wheels at the optimal slip at all time, leading to reduced friction potential values calculated for the vehicle perspective. Therefore, a suitable evaluation interval of the SWB measurements, which approximates the results of the full braking measurements as closely as possible, has to be found. The friction potential for each tested surface is calculated by averaging all repetitions in the interval MASS. Similarly, the average of all SWB measurements in the optimised interval has been used. Two parameters have been used for the optimisation: t_0 the start of the interval, where 0 was set to the point at which the ABS controller started to reduce the brake pressure, and dT the length of the interval. The resulting error function thus is

$$E = \frac{1}{n}\sum_{s=1}^{n}\left[\left|\frac{1}{m_s}\sum_{r=1}^{m_s}\frac{a_{mass}}{g} - \frac{1}{l_s}\sum_{q=1}^{l_s}\mu_{SWB}(t_0, dT)\right|\right]. \tag{3.4}$$

In this equation r denotes the repetition of the full brake measurements on the surface s and q the repetition of the SWB measurements on the same surface. Figure 3.9 shows the errors for several parameter variations of t_0 and dT.

It can be seen that if an evaluation interval around the start of the ABS intervention is chosen, the average error varies only slightly. Therefore, a symmetric interval around the starting point t_0 was selected. An interval length of $dT = 0.2\,s$ was chosen with a corresponding $t_0 = -0.1\,s$. Given the 100 Hz measurement frequency used for all

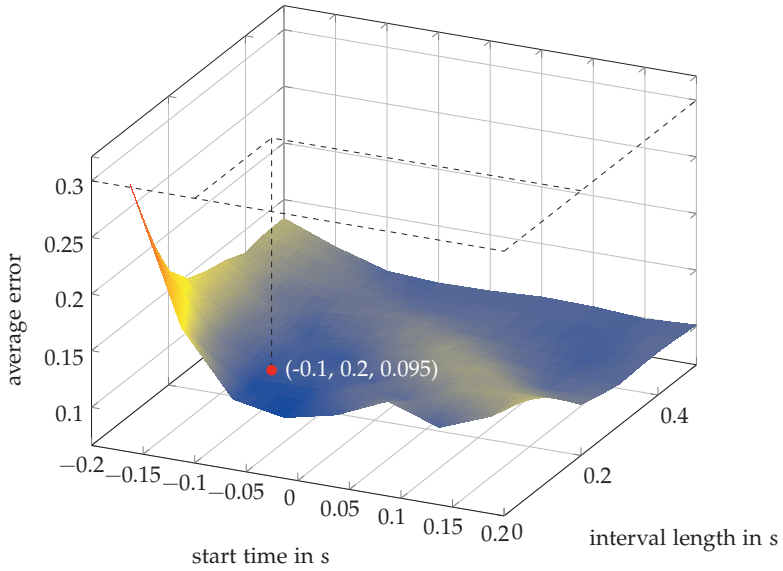

Figure 3.9: Average error between friction potential measured with full braking tests (a_{mass}) and SWB evaluated over different intervals on the seven test surfaces; the marker specifies the chosen interval

later measurements, the resulting friction potential is the average of 20 values. The average friction potential measurement error between this SWB interval and the full braking measurements is just below 0.1. The measured friction potential of the full braking interval a_{mass} and the chosen SWB interval are plotted in figure 3.10. It can be seen that a relative large error is present on the wet surfaces. This is due to the increasing deceleration over time on wet surfaces during the full braking tests. This leads to an underestimation of the friction potential measured with SWB. There is also no guarantee that the friction potential of the surface is homogenous over the braking distance.

The short SWB interval cannot replicate both effects. Therefore, as an additional comparison, the friction potential of the full braking tests evaluated in the same 0.2 s interval as the SWB is added in the figure. The average error using the same interval reduces to 0.049. The standard deviation of the evaluated full braking intervals and SWB are plotted as horizontal and vertical error bars for each surface.

In the MASS full braking interval the standard deviation varies between the different

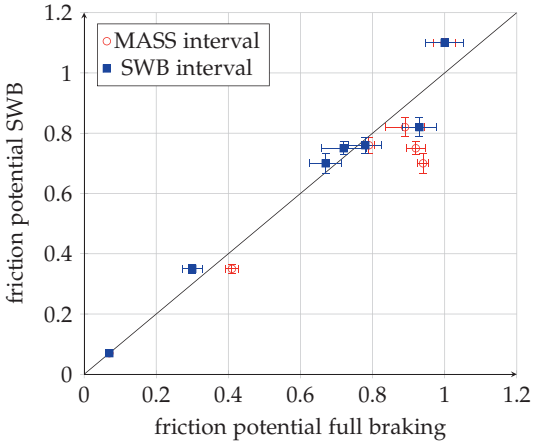

Figure 3.10: Correlation between SWB and full braking tests on the test track surfaces; circle: comparison between SWB interval and MASS full braking test interval; square: same interval used for both measurement methods

surfaces. The largest one of 0.053 was measured on dry asphalt and the smallest of 0.003 on the epoxy tiles. The others lie around 0.03. The standard deviation of the SWB measurements varies less. All measured variations lie between 0.013 and 0.033. The exception is the epoxy tiles surface with a standard deviation of 0.006. The smallest variance in both the full braking tests and SWB tests can be explained by the very small measured deceleration values.

Since there is no way to reduce the errors in the correlation and underestimating the real friction potential for planning purposes is safe[3], a one to one mapping between the measured SWB friction potential and the real friction potential is assumed. In addition, a safety margin of 0.1 is introduced for all SWB measurements.

3.3 Measurements on Public Roads

Using the newly developed SWB test method, friction potential measurements on public roads were possible without affecting other traffic participants. In order to gain deeper insights into the effect of different influencing factors, repeated measurements on a specified route were made during October 2016 and July 2017. Based on an initial

[3] although this may reduce the actual driving speed

SKM measurement explained in detail in the next chapter and some points of interest[4], 74 GNSS coordinates for SWB were selected. An error of 1 m in x- and y- direction was allowed for the activation of the measurement. The test track was chosen to include a wide variety of different roads. This includes roads in industrial areas, small residential streets, a country road, highway-like roads and highways. All but one point were on asphalt surfaces, while one measurement point has been placed on a cobblestone surface. During the test period, several of these points were resurfaced so that the data collected before and after the resurfacing have to be analysed separately. These road construction also led to longer periods of road closures so that not always the whole track was driven. In addition, traffic jams and vehicles parking on braking points prevented some measurements. Nevertheless, 4773 valid measurements were conducted and are available for further analysis. During this evaluation, it was discovered that the ABS algorithm implemented in the special ESC software did not utilise the full friction potential if the braked wheel was a wheel on the inside corner. Thus, while measurement points were set in corners, these measurements are not included in the following discussion but are used in chapter 5. These led to a remainder of 65 evaluated measurement points. In order to reduce the influence of contamination, all measurement with visible road contamination or unclear road condition have been excluded from the friction potential evaluation. This was especially the case for measurements during winter, where large amounts of salt residue were visible. 3812 measurements remain after applying this filter.

During the measurement period, three different tyre sets were used. The one used during the development of the SWB method, a winter tyre set and a new summer tyre set of the same type as the first summer tyre set. The used summer tyres have a EU wet grip friction label A, the winter tyres are labeled B.

In addition to the friction potential measurement, information about the weather conditions was stored. This allows to compare measurements during different road conditions[5]. Using this large database, the influence of different factors on the friction potential is analysed for selected braking points in the next sections

3.3.1 Variation of Measured Friction Potential Values

The spread of the SWB measurements during the development of the method has been discussed in the previous section. If the variance during the measurements on public roads is larger, this indicates that influencing factors, which were constant during the

[4] especially bridges, because different surface conditions were expected there
[5] The process of finding the correct road condition is explained in section 5.2.

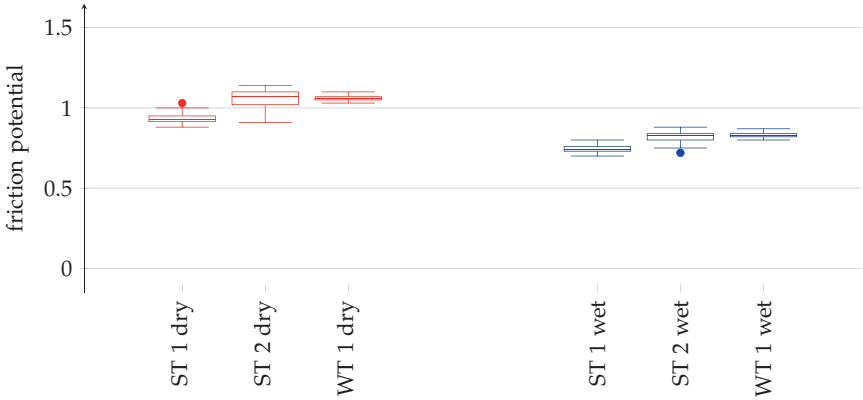

Figure 3.11: Friction potential measurements on brake point 29 splitted by used tyre and road condition

development of the method, produce this additional variation in the measurements. In order to evaluate this variance, brake points with many valid measurements have been chosen. A few brake points are analysed in detail. The results for all braking points can be found in appendix B.

The most valid measurements were conducted on brake point 29 with 129 measurements. These are split into 29 with the first summer tyre set, 64 with the second summer tyre set and the remaining 36 with the winter tyre set. The results of all tyres can be seen in figure 3.11. In order to exclude the influence of the tyre set from the results, only measurements with the second set of summer tyres are evaluated. 22 of these measurements were conducted on a wet road and 41 on a dry one. During one measurement, the brake point was visibly contaminated by dirt. This measurement is excluded. The average friction potential of the dry surface is 1.06 with a standard deviation of 0.057. On the wet surface, the mean value is 0.82 and the standard deviation 0.039. The first observation of these values is that the standard deviation of the measurements on the dry surface is larger than on the wet surface, despite different water heights on the wet surface. Both standard deviations are only slightly larger than the one measured on the test track. The relatively small variance on the wet confirms the assumption that as soon as the surface is wet, the water height does not influence the friction potential anymore until partial aquaplaning effects appear. At point 29, the normal driving velocity is around 40 kph so that aquaplaning effects should never occur.

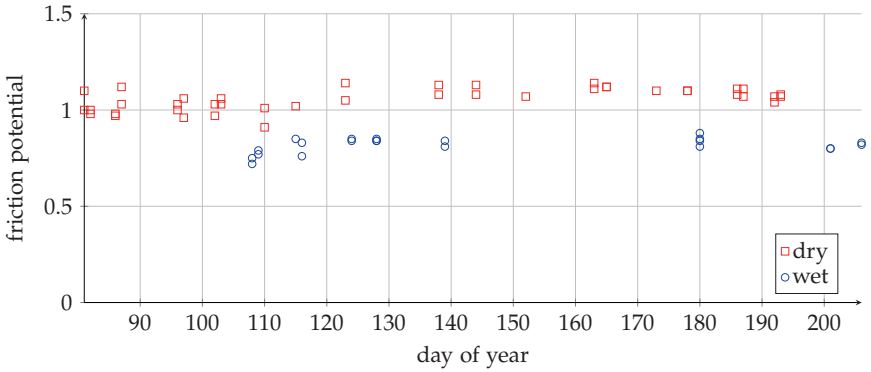

Figure 3.12: Friction potential measurements on brake point 29 over day of year

Next, the collected data with the first summer tyre set at that point (29) is compared to the data of the second summer tyre set. Dry measurements on point 29 with the first set average to 0.94 with a standard deviation of 0.042. In wet conditions, the mean value is 0.74 with a standard deviation of 0.028. This indicates that the friction potential of the first tyre set is about 0.1 lower than the second set. This can be caused by different factors. The first tyre set was used during the development of the method. Therefore, the tyres were worn down to about 4 mm. Also, the first tyre set was used until the beginning of January, while the second set was used from end of March to August. As mentioned in chapter 2, several researches found an influence of the season on the friction potential. The extent of this seasonal effect is dependent on the overall weather conditions and road surface and unknown for point 29. In the period in which the second summer tyre was used, no seasonal development can be derived. This can also be seen in figure 3.12. This data neither supports a sinusodial seasonal change nor a friction potential reduction due to polishing effects. Therefore, it is more likely that the wear state of the tyre influences the friction potential. This should be evaluated in a future measurement campaign not part of this thesis.

Next, the summer and winter tyre results are compared. The winter tyre produces almost the same friction potential as the second summer tyre set, even in wet conditions even though the winter tyres have a worse label than the summer tyres. The measurement spread in the plots is rather small. This is caused by the low number of measurements with winter tyres with only 13 measurements on dry and 11 on wet. All these measurements showed very similar friction potential values.

3.3.2 Influence of the Road Surface

The measurements on the brake testing surfaces already showed, that the road surface can have a significant impact on the friction potential. The road surfaces on the test track are designed for this variation. Therefore, one goal of the repeated measurements on the public roads was to provide an overview of the friction potential, which can be expected on public roads. Therefore, in figure 3.17 the friction potential values of all brake points on straights for dry condition and wet condition are plotted. If there was a known road maintenance on the brake point, the measurements are separated into all measurements taking place before and after the road maintenance.

After the road maintenance is finished, all measurements conducted on these brake points are split into a new brake point highlighted by a $*$ after the original brake point number. The connecting lines between the brake points have no physical meaning and are only added to highlight the friction potential changes between the braking points. The friction potential variation between the measurement points is discussed in the next chapter.

In order to compare the friction values, the used tire set is introduced as subscricpt, the intermermediate layer as subsubscript and the brake point as superscript. The friction potential of all dry measurements is around 1.0. The change of the measured friction potential between the different brake points is almost the same for each tyre. This indicates that the influence of the different rubber in the winter and summer tyre is marginal. The first summer tyre set always provides a lower friction potential than the second set, indicating that the tyre wear reduced the friction potential equally on all brake points and not only on brake point 29. The friction potential change between the brake points for summer tyre set 1 is only 18 %. Since with summer tyre set 1 no measurements on dry cobblestone were conducted, only asphalt surfaces are considered. The minimum value measured is $\mu^{\mathrm{BP1}}_{\mathrm{SR1}_{\mathrm{dry}}} = 0.9$ and the maximum $\mu^{\mathrm{BP15}}_{\mathrm{SR1}_{\mathrm{dry}}} = 1.1$. Measurements on dry cobblestone (brake point 51) were conducted with the second summer tyre set and the winter tyre set. The friction potential measured is lower than on all asphalt points with $\mu^{\mathrm{BP51}}_{\mathrm{SR2}_{\mathrm{dry}}} = 0.9$ and $\mu^{\mathrm{BP51}}_{\mathrm{WR}_{\mathrm{dry}}} = 0.86$ respectively. For these tyres, the minimum measured friction potential value on asphalt is $\mu^{\mathrm{BP5}}_{\mathrm{SR2}_{\mathrm{dry}}} = 0.98$ and $\mu^{\mathrm{BP21}}_{\mathrm{WR}_{\mathrm{dry}}} = 1.0$. The relative change of friction potential between the different asphalt braking points for the second summer tyre set is 17.6 % and for the winter tyre set only 12.3 %. All the friction potential values are very high compared to the friction potential required for normal driving[6]. This indicates that the change of friction potential between the measured points is of minor relevance if there is no intermediate layer but

[6] see section 6.1

the conclusion is limited to the few measured brake points on the track. Other surfaces with a larger spread in the dry friction potential might exist and can only be found by extending the SWB measurements to new locations.

On wet surfaces, the friction potential spread is larger. The measured friction potential of the first summer tyre set varies by 28.6 %, of the second summer tyre set by 26.9 % and of the winter tyre set by 34.2 %. The minimal measured friction potential value is between 0.72 and 0.76. On cobblestone, the minimal measured friction potential is 0.64 measured with the winter tyre. The measurements on the brake test track and measurements conducted on the FAT project track (discussed in appendix B.1) highlight that asphalt and cobblestone surfaces with even smaller friction potential values exist. These lower friction potential values are required far more frequently for normal driving. Therefore, knowledge about the wet friction potential is important for the trajectory planning task.

One last interesting feature, which can be seen in the plot, is the change of the friction potential after the road maintenance. It is unknown if the road maintenance consisted of a surface treatment or a complete resurfacing. According to the influencing factors discussed in the introduction, a new surface should improve the microtexture and therefore the friction potential. At some brake points, measurements with the second summer tyre were conducted before and after the road maintenance. The number of repeated measurements is very small so that the changes might also be due to measurement noise or other unobserved influences. At brake point 8, two measurements on a wet surface resulted in an average friction potential of 0.78 before the road maintenance. After the road maintenance, three measurements showed an average of 0.92. A similar increase of up to 0.1 can be seen for points 7, 9, 14, 16 and 18. Contrary, point 15 showed a marginal decrease in friction potential from 1.04 down to 1.02. This decrease is well within the measurement inaccuracy. The wet friction potential before the maintenance was already very high so that road maintenance to increase it further was not required.

3.3.3 Influence of the Road Condition

In the previous section, it was already visible that a significant difference exists between the friction potential on dry and wet roads. Therefore, in this section, the friction potential reduction from dry to wet will be discussed. Figure 3.13 shows a histogram of the distribution of the relative friction potential reduction for each tyre. It can be seen that the histogram looks rather similar for each tyre. Most likely is a friction potential reduction between 20 % and 25 % compared to the dry values. There are some

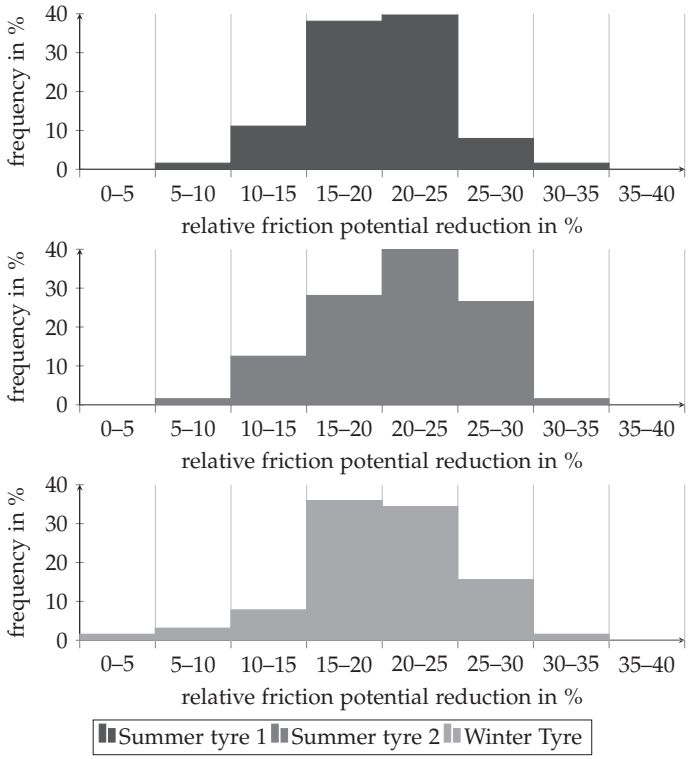

Figure 3.13: Relative reduction of the friction potential on a wet compared to a dry road surface

braking points where a friction potential reduction of less than 10 % (The minimum is 2.6 % with the winter tyre set, which could be caused by a small number of measurements.) are measured, while others showed a friction potential reduction of up to 32 %. This shows, that for the measured brake points, the difference between a dry road surface and a wet road surface can have an equal impact on the friction potential as the difference between a brake point with a good wet friction potential and a worse friction potential. It can be concluded that a detection of the road surface condition is as important as knowledge about the road-surface-tyre-interaction itself.

During the measurements on public roads, no aquaplaning or partial aquaplaning was encountered. Some aquaplaning measurements conducted with a different test

vehicle on a test track are presented in appendix B.2 to highlight the importance of correctly identifying this driving situation.

Similarly, during the measurement period only three measurements with a visible snow/ice surface were conducted. The measured friction potential value was between 0.32 and 0.36. Further results of measurements on snow / ice conducted with the same test vehicle but a different set of winter tyres during tests in Sweden are presented in appendix B.3.

3.3.4 Influence of the Surface Temperature

An additional measured influencing factor is the road surface temperature. At brake point 29, measurements were conducted at surface temperatures between −1 °C and 44 °C. The results for dry and wet road condition can be seen in figure 3.14. Both figures suggest that the friction potential increases with increasing temperature. Over the whole temperature range, the increase is up to 0.2, which is larger than the expected measurement spread. The measurements indicate a different relationship for dry and wet surface conditions. The measurements on the dry surface indicate a linear relationship, while the measurements on the wet surface indicate a non-linear relation with a clearly visible increase of the friction potential below 10 °C, almost no influence between 10 °C-20 °C and once again a visible increase of the friction potential above 20 °C.

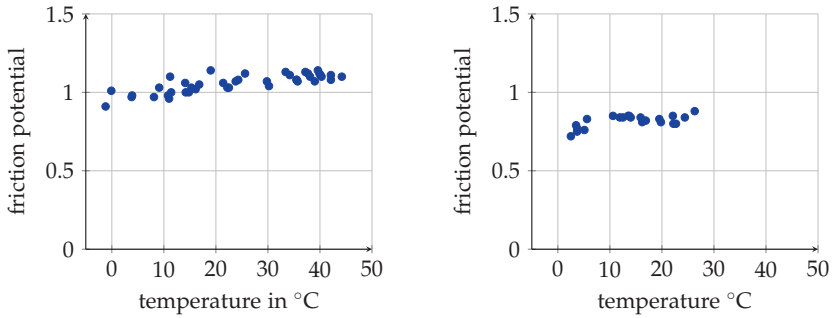

Figure 3.14: Temperature influence for all measurements with summer tyre 2 at brake point 29; left: dry road condition, right: wet road condition

Figure 3.15 shows the same plots for brake point 20. On the dry surface, once again, a linear relationship can be assumed. The measurements on the wet road surface do

not show the behaviour seen at brake point 29. This indicates that, while a dependency of the friction potential on the road surface temperature cannot be ruled out, the road surface temperature cannot be considered separately. According to the rubber properties (see section 2.1.2), the surface temperature shifts the frequency response of the rubber and thus changes the hysteresis friction component depending on the rubber excitation. Thus, the temperature dependency can only be considered in combination with the microtexture of the surface and the rubber properties. If these are not available for trajectory planning, safety margins wich also account for the road surface temperature should be introduced.

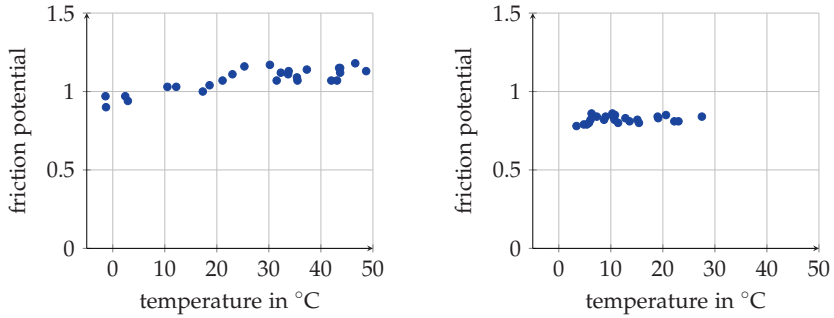

Figure 3.15: Temperature influence of all measurements with summer tyre 2 at brake point 20, left: dry road condition, right: wet road condition

3.3.5 Influence of the Velocity

Finally, as last influencing factor, the driving speed is discussed. A brake point with a higher allowed maximum speed is better suited for this analysis because at these locations traffic conditions lead to more varying start velocities. The number of conducted measurements on these brake points is significantly reduced due to construction work and traffic jams, which did not allow measurements. Figure 3.16 shows the measured friction potential plotted over the velocity at brake point 56 on a highway.

During dry road conditions measurements with starting velocities from 79 kph up to 99 kph were driven. During wet conditions the spread in starting velocity is larger with the slowest starting velocity at 57 kph and one measurement with a starting velocity of almost 114 kph. The plot indicates that for both road conditions, no change of the friction potential depending on the starting velocity can be seen. Therefore, the measured

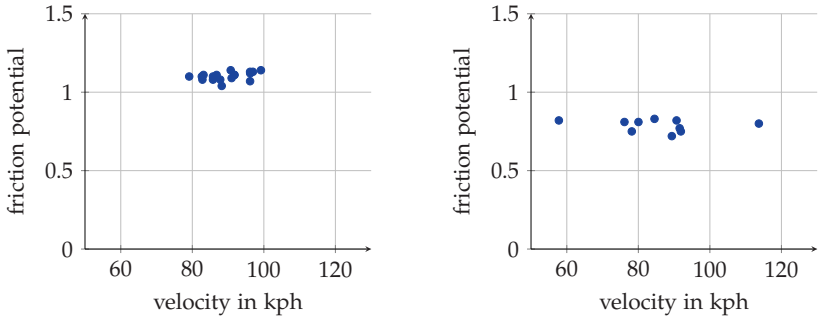

Figure 3.16: Velocity influence of all measurements with summer tyre 2 at brake point 20; left: dry road condition, right: wet road condition

friction potential can be assumed valid for every velocity. For the wet surface, this is only true if no aquaplaning can be assured. Since no aquaplaning like situations were encountered during testing, this assumption is true for all conducted tests.

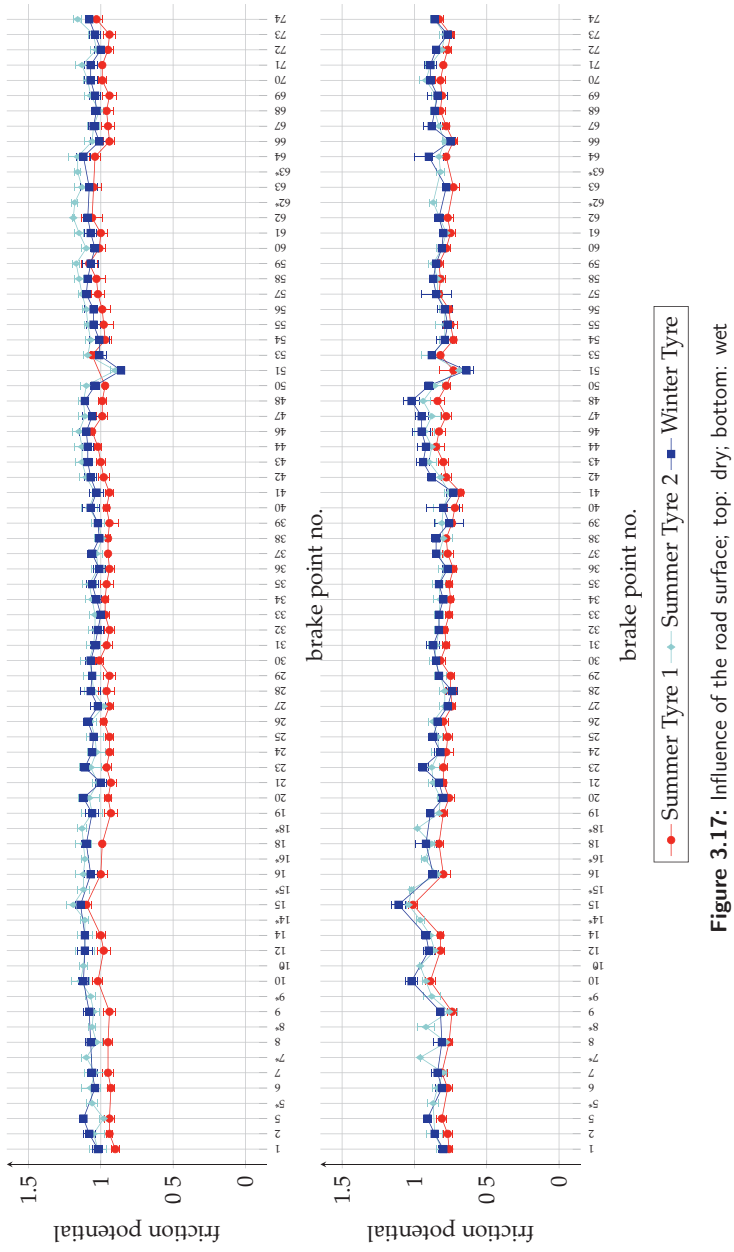

Figure 3.17: Influence of the road surface; top: dry; bottom: wet

4 Grip Map

In order to provide continuous information about the friction potential to the AV, information about the road surface needs to be available. The SWB method discussed in the previous chapter only allows measurements at discrete points and does not scale for mapping a whole road network. Therefore, a continuous friction potential measurement method needs to be used. Measurements found in literature and the measurements discussed in section 3.3 indicate that knowing the exact wet friction potential value is more important than the dry friction potential. The wet friction potential is lower and a larger difference between the friction potential values was found on wet surfaces. Friction potential related accidents on wet roads appear in the accident statistics (see section 1.1). The significant reduction on wet surfaces is shown by previously published measurement results (see section 1.1), while the measurements conducted during this project show a reduced, but still reasonable high friction potential. One possible reason could be due to the small number (74) of tested surfaces, which were by chance all in good condition. The possible large spread in wet friction potential led road maintenance authorities to use the wet friction potential values as one indicator for road renewal. Similarly, the wet friction potential is used as one of the categories on the EU tyre label.

Continuous friction potential measurement methods are a well established methodology in road maintenance (see section 1.2.1). These continuous measurement methods are normally used for larger road classes like highways. Therefore, usually high driving speeds are required by the specification. The tyres and the operating points of the tyre differ from the typical operating conditions during an ABS full braking manoeuvre of a modern vehicle. This means that some differences between the continuous measurement methods and the available friction potential of an AV exist. Additional challenges for these friction potential measurement methods are the changing driving velocities and smaller corner radii on smaller road types. Initial research to use the SKM method on smaller road has been conducted in [141]. Due to the inhomogeneous road surfaces in cities, a reduction of the measurement interval from 100 m down to 20 m or even 10 m is used. This requires a more accurate localisation of the measure-

ments[1]. Friction potential measurements were only available in one city. Since this data was not enough to derive empirical threshold and warning values, a linear scaling (depending on the measurement velocities) of the values applied for highways is proposed.

Since apart from this publication no information about the usability of continuous measurement methods on city roads was available, measurements with the two devices SKM and RoadSTAR have been conducted. The following analysis will show whether continuous measurements can be used to map the friction potential of a city road network. The measurements include tests on a test track consisting of two straights with several different asphalt and one concrete surface and measurements on the public road course used for the SWB tests. Due to the project time-line, the SKM and RoadSTAR measurements have been conducted one year apart. As already discussed in the previous chapter, between the measurements several segments of the public route have been renewed. Thus, a direct comparison between both measurements cannot be done for the whole route. In the time between the SKM and RoadSTAR measurements, the single wheel braking tests have been conducted. At the 74 SWB brake points, the measured friction potential is compared to both continuous test methods. In the previous chapter, differences between the tyres have been identified. Therefore, the measurement results are analysed separately for each tyre. Since all continuous friction potential measurement methods always measure wet friction potential values, only measurements on wet surfaces are considered.

One of the main tasks in the evaluation of the measurements of both trucks is to match the measurements to a location on the track. Both trucks are equipped with a GNSS system, but it turned out that the performance of both systems varied. The SKM truck is fitted with a standard GNSS. In the provided XML-file format, only one GNSS point each 10 m is provided, which further complicates the localisation of the measurements. The RoadSTAR truck uses a differential GNSS system. This system is also coupled with odometry from the wheels. Measurement files provided in csv file format provide one coordinate each meter. The results of this system are comparable to the accuracy reached by the differential GNSS system fitted to the test vehicle. Therefore, one measurement of the RoadSTAR truck was used as reference track. The other measurements were matched to this reference track by calculating the length of the normal to the reference track between the reference track GNSS points and the measurement GNSS points. In order to find a valid match, the normal distance is allowed to be less than 5 m. GNSS errors along the driving direction cannot be

[1] This also proved a problem during the measurements described in this chapter.

corrected this way. The heading difference between both tracks is only allowed to be 25°. These relatively high tolerances have been used in order to find matches for the SKM measurements. Nevertheless, the matching process has difficulties to match parts of the tracks with obstructed satellite visibility.

The reference track was split in 5 m long segments. The reason for the 5 m segments is, that in order to affect the vehicle behaviour negatively, a reduced friction potential needs to persist over a certain distance. The 5 m segment length ensures that the friction potential is influencing all wheels of the vehicle, while the used resolution is significantly smaller than the 100 m segments used in road maintenance.

For the track on public roads, the 5 m segments are numbered continuously from 1 to 7013. On the test track, both straights are numbered separately from 1 to 195 and from 1 to 204, respectively. The average of all provided friction potential values of these 5 m segments was used as friction potential for each segment.

4.1 SKM Measurements

The SKM measurements took place in the summer of 2016. The measurements included three laps around the public roads track. After that, a larger number of tests took place on the test track. All measurements were conducted at the same day using the same SKM tyre. The measurements were provided in xml. Every 10 m a new coordinate was given. The other measured values were provided with one value each meter. The provided values are the friction potential, the velocity, the lateral distance to the lane border and four temperature values; road surface temperature, tyre temperature, air temperature and water temperature. It has to be noted that μ is calculated by dividing the measured side force by the static load. No dynamic load measurements are used in SKM trucks. The temperature sensors are used for applying empirical derived friction potential corrections. Since all measurements took place on the same day, the temperature conditions were almost constant. Therefore, no temperature correction is applied to the provided friction potential values. The velocity dependency is discussed in the next section.

4.1.1 Test Track

The slowest valid SKM measurement speed of 40 kph and the fastest allowed velocity of 80 kph have been tested repeatedly on the two straights of the test track. Due to problems with the measurement system, the number of available repetitions varies. On the first straight, nine measurements at 40 kph are available as are ten on the second

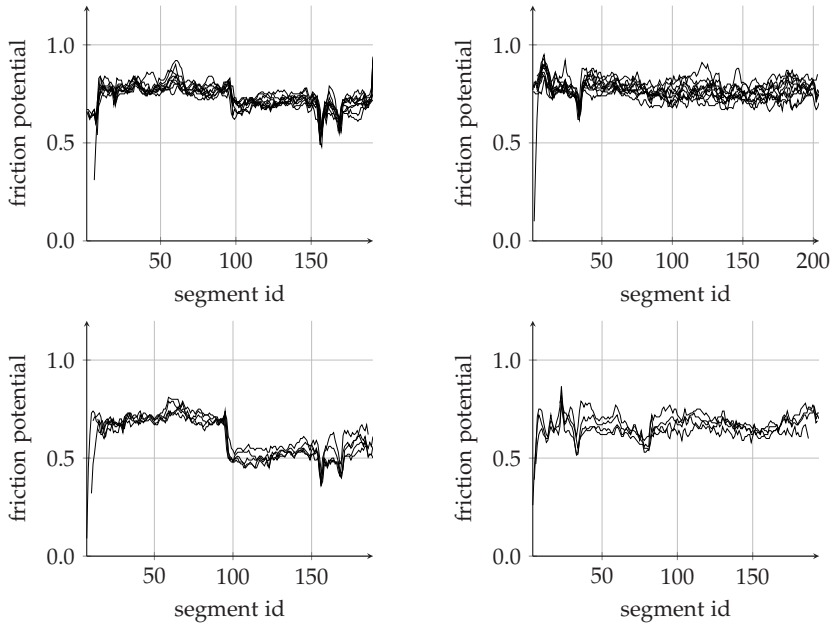

Figure 4.1: SKM measurements on test track; left column: straight 1; right column: straight 2; first row: 40 kph; second row: 80 kph

straight. The measurement at 80 kph resulted in five measurements on the first straight and only four on the second. All the measurements matching the segments are shown in figure 4.1. On the first straight at the change from asphalt to concrete (around segment 100), a drop in measured friction potential is visible with both velocites. The remaining parts of the two straights provide a friction potential value of around 0.8 at 40 kph and around 0.7 at 80 kph. This indicates a velocity dependency of the SKM measurements. Overall, the measured friction potential is significantly higher than the warning value for SKM measurements, which indicates good friction potential properties on both straights.

Reproducibility

The reproducibility of a measurement describes the variance of measurements conducted on the same surface. An important indicator for the repeatability is the sample standard deviation s_N of the measurements. N is the number of measurements, χ_{j_i}

is the i-th measurement value at segment j and $\bar{\chi}_j$ is the mean value of all values measured on segment j.

$$s_{Nj} = \sqrt{\frac{\sum_{i=1}^{N_j}(\chi_{j_i} - \bar{\chi}_j)^2}{N-1}} \tag{4.1}$$

In order to calculate the standard deviation, repeated measurements are required. For the measurements at 40 kph, the available number of measurements is sufficient. The small number of 80 kph measurements does not allow an accurate calculation of the standard deviation. Therefore, it was assumed that the standard deviation of a segment is independent of the mean value of the segment. For each segment, the distance between the mean value of the segments and the measurements is calculated. Finally, the standard deviation is calculated using the distances of all S segments and a mean of zero. For the 40 kph measurements, both calculation methods are used to compare the effect of this approximation.

$$\bar{s_{Nm1}} = \frac{s_{Nj}}{S} \tag{4.2}$$

$$\bar{s_{Nm2}} = \sqrt{\frac{\sum_{j=1}^{S}\sum_{i=1}^{N_j}(\chi_{j_i} - \bar{\chi_j})^2}{\sum_{j=1}^{S} N_j}} \tag{4.3}$$

Using the first method (subscript m1), the average sample standard deviation of measurements taken on the first straight is 0.027, while the maximum standard deviation is 0.14 and the minimum is 0.006. For the second straight, the results are mean 0.046, min 0.0138 and max 0.227. It has to be noted, that only segments with more than nine measurements were used in the calculation. This way, the suspiciously low friction potential measurements at the start of some measurements are not included in this evaluation. These are most likely due to the start of the measurement after a very narrow corner. If both straights are merged together, the average standard deviation is 0.0362. The second calculation method (subscript m2) results in an average standard deviation of 0.0382, which is similar to the first method.

Figure 4.2 shows some information about the standard error distribution. The left part of the figure shows the distribution of the errors used to calculate the standard deviation in the form of a histogram. On the right hand side of the plot, the error distribution is plotted in a q-q plot. If the data was normal-distributed, the q-q plot would follow the straight line with slope s_N. This is the case for most measurement errors, except large positive errors. These errors appear to be more likely than predicted by

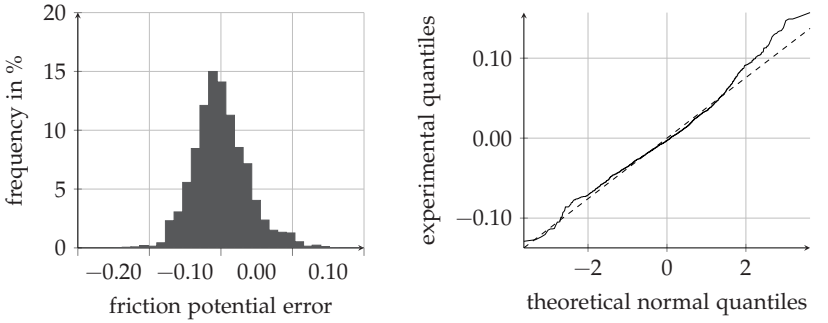

Figure 4.2: Error distribution of SKM measurements on test track; left: distribution of measurement errors; right: q-q plot showing normal error distribution

the normal distribution. Since the error is calculated by substracting the measured μ_{pot} from the average $\bar{\mu}_{pot}$, a positive error means that it is more likely that a significantly too large friction potential is measured.

Using the second method to calculate the average sample standard deviation of the 80 kph measurements results in $s_N = 0.0304$, indicating that measurements at this speed vary less. It has to be noted that at this speed the measured friction potential values are also smaller. Since the number of measurements is insufficient to calculate the variance of each segment according to equation 4.1, the standard error of different segments cannot be compared directly. The large differences between the measurement errors on different segments indicate, that some other properties at these segments influence the measurement result. One possible explanation would be dynamic load changes due to road unevenness. In the absence of additional measurement channels, this cannot be investigated further.

Velocity Dependency

As already discussed at the beginning of this section, a velocity dependency of the SKM measurements can clearly be seen. The mean of all measurements for each speed is plotted in figure 4.3. According to the criteria listed in table 1.1, a velocity increase of 20 kph decreases the measured SKM friction potential by 0.07. This would lead to a reduction of 0.14 of the 40 kph measurements compared to the 80 kph measurements. As can be seen in the figure, this offset does not universally apply to the measurements. The different behaviour on the asphalt segments of the straights and the concrete ones

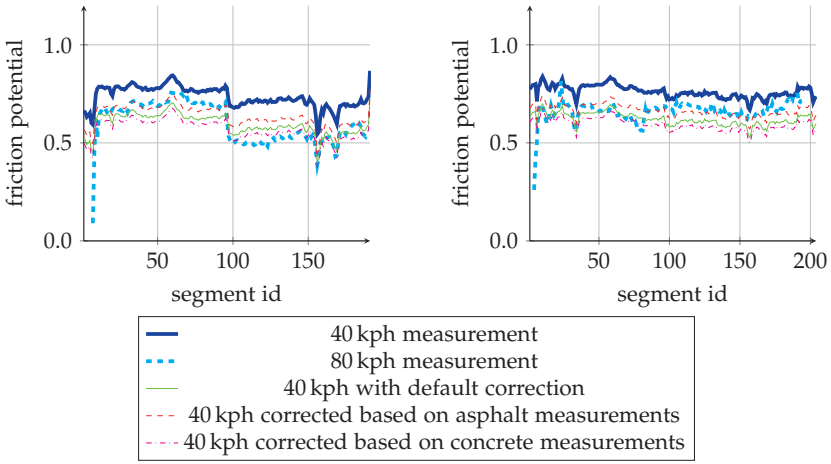

Figure 4.3: SKM measurement velocity dependency on test track

require different offsets for both parts. These offsets are calculated by calculating the mean difference between the 80 kph and the 40 kph measurements on asphalt and concrete segments, respectively. The calculated value for the asphalt part is 0.0973 and 0.1683 for the concrete part. Since no universal applicable offset was found, it was decided to analyse measurements taken at different measurement speeds separately.

4.1.2 Public Road

During the measurements on the public road, the measurement was stopped whenever a corner or the traffic situation did not allow homogenous measurements. Therefore, in the continuous map, there are segments without measurements. Additional measurement gaps arise due to the gaps between the valid SKM measurement speeds. Although the minimal allowed SKM measurement speed is 40 kph, the public road track also included 30 kph zones. These SKM values have been compared to the SWB measurements. Therefore, an additional valid measurement speed of around 30 kph was introduced, resulting in four velocity categories, 30 kph, 40 kph, 60 kph and 80 kph, each with an allowed average deviation of ± 4 kph. In the appendix, figure C.1 shows the provided friction potential values for all three laps plotted over the track segments of the reference track. The colour denotes the speed category in which the measurement was conducted in.

Table 4.1: SKM standard error comparison between public road and test track

Velocity	StdErr Test Track	StdErr Public Road Track
40	0.0382	0.0476
60	-	0.0429
80	0.0304	0.0201

In laps one and two, the highway section, the only part measured at 80 kph, apparently also has the smallest friction potential. That this difference might only be down to the higher driving velocity can be seen in lap three. At the end of the highway section, a traffic jam reduced the driving velocity to measurement velocities of the 30 kph or 40 kph category. This decrease of the measurement velocity increases the measured friction potential to a similar magnitude as other roads measured at this velocity. A comparison of the measurements conducted with the normally allowed measurement speeds with the official warning values shows that about 1 % of the measurements conducted with 40 kph are below the warning value of 0.49; 0.03 % of the 60 kph measurements below the warning value of 0.44 and 0.65 % of the 80 kph measurements below the warning value of 0.39. Further analysing segments with friction potential values below the warning value shows that these values are not reproduceable. For example, the smallest friction potential value with 40 kph was measured on segment 4688 in lap two with a value of 0.32 In the other two laps, the same segment has been measured with values of 0.47 and 0.54. The value of 0.32 is below the threshold value indicating that immediate road renewal is required, while the value of 0.54 is above the warning value and would not require any further action.

The measurements on the test track show that most segment measurements are repeatable with only a small variance, while there are others, which can show a quite significant variance. On the public road, at most three measurements of every segment are available so that only method two can be used to calculate the average measurement standard error. A comparison between the measurement error on the public road and the test track can be found in table 4.1. No clear conclusion can be derived. The standard error of the 40 kph segments is about 0.01 larger while the error for the 80 kph segments is 0.01 lower. Thus, the results derived on the short test track are a good representation of the overall measurement quality.

The average variance cannot help to identify segments with a high measurement spread. Therefore, it was decided that if more than one measurement of the same velocity category was available, the median of all available measurements was used. This way, only 0.28 % of the measurements conducted at 40 kph are below the warning

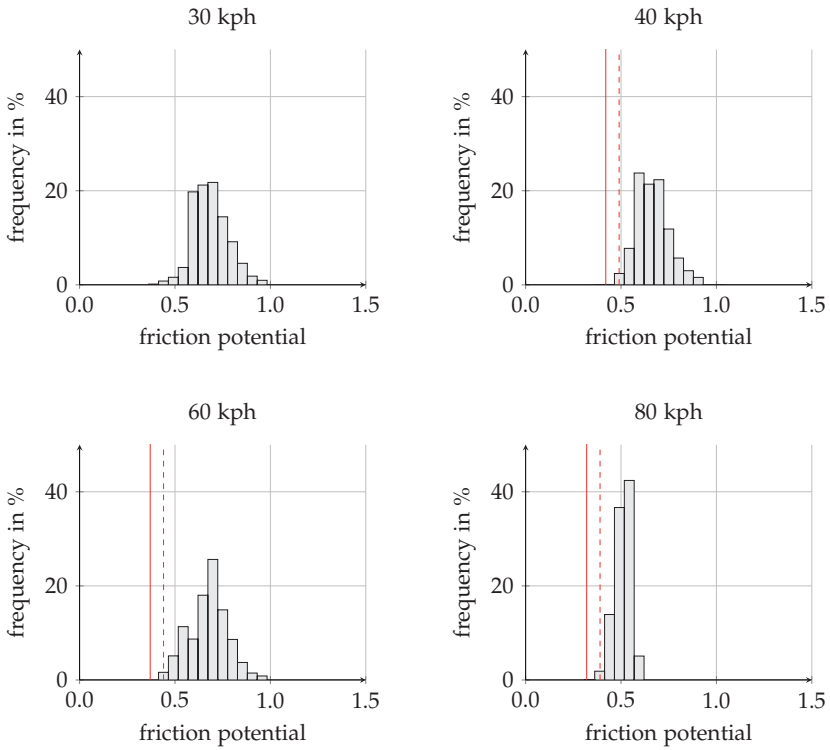

Figure 4.4: Friction potential distribution of public road track measured with SKM

value. At most two segments after each other (10 m) are below this value.

The friction potential distribution of the segment median for each of the four velocity categories can be seen in figure 4.4. For the three velocities usually valid, the warning value is added as dotted line and the threshold value as solid line. The plots indicate that according to SKM the overall grip of the public road is rather good.

In addition to the variation of the measurements on the public road, another important measure is the number of segments with valid measurements. After the three measurement laps, on 70 % of all segments at least one valid measurement was conducted. Lap one and lap two resulted in a quota of about 58 % of the segments, while the third measurement lap achieved only a 41 % covering due to increased traffic on the lap.

4.1.3 Comparison with Single Wheel Braking

Despite of the unexpected large velocity influence on the SKM measurements, the continuous measurements are now compared to the results of the single wheel braking measurements. A good correlation between both measurements would be a first indication that the continuous method could be used to derive a continuous friction potential map but for a final conclusion, the number of compared SWB points is still low.

It was shown in chapter 3 that the measurement results of the different tyres used during the SWB tests also differed. Although the most likely reason for the differences was the tyre wear, a contribution of the road surface could not be excluded as possible reason. Because of the encountered differences, the SKM results are compared with the results of the first (SR1) and second (SR2) summer tyre set separately. The SKM measurements are compared with all measurements conducted before the road renewal, if any took place during the SWB test period.

Only SWB measurements on a wet surface were used. In addition, only the tyres SR1 and SR2 are used in the analysis. The winter tyre set has not been used due to the rather low number of measurements and the discovered friction potential changes due to wear [21].

The results for the different SKM velocities are shown in figure 4.5. Since no speed conversion for the different valid SKM measurement speeds has been derived, the different measurement speeds have to be analysed separately, further reducing the number of brake points used in the analysis. As can be seen, the correlation coefficent and linear approximation of the relation vary a lot between the different measurement velocities. Measurements at a velocity of 30 kph and 60 kph both indicate a linear relation but measurements with the most available measurement points, 40 kph and SR1, only result in a correlation coefficient of 0.484. This indicates only a weak linear relation.

Similarly, the correlation coefficient of SKM measurements with 80 kph is only 0.44 for the SR1 measurements and 0.369 for the SR2. The small correlation coefficients of the 80 kph measurements can be explained by the small number of measurement points, which only vary slightly in the measured friction potential. The dependence of the correlation coefficient on the variability of the data is known as range restriction [142]. Measurements over the whole friction potential range might lead to a better correlation factor.

The varying linear approximations between the different measurement velocities in combination with the weak correlation of the 40 kph measurements show that although

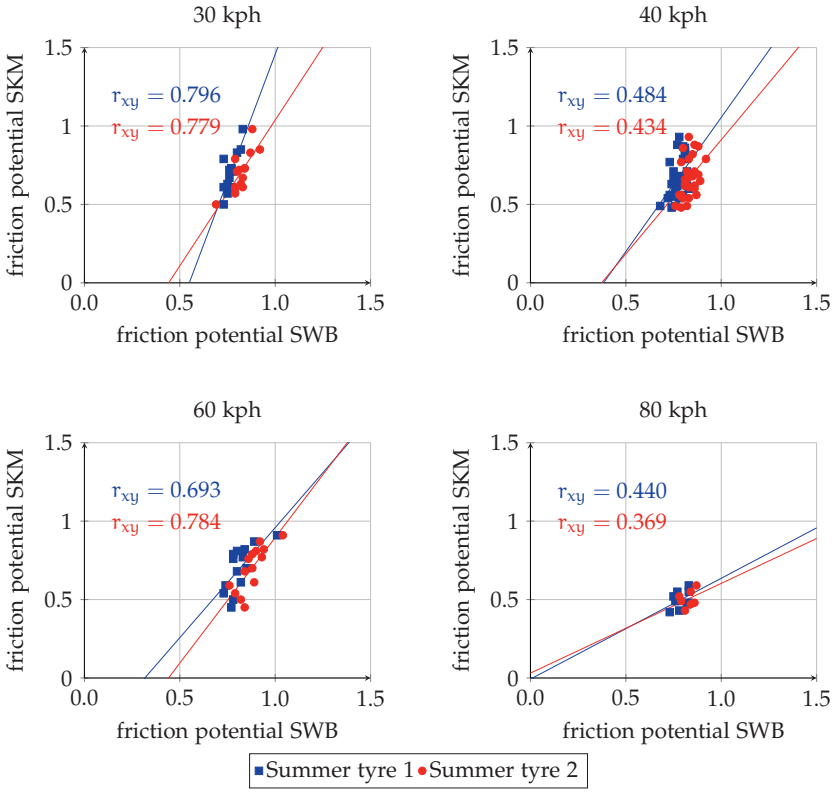

Figure 4.5: Comparison of SKM and SWB tests on public track

there is some relation between the SWB measurements and the SKM measurements using the linear relations would prove difficult. Probably the data contains a lot of measurement noise or other not discovered systematic measurement problems.

Another argument against the linear relation between SKM and SWB is that it would be expected, that SKM values approaching zero would result in SWB values also approaching zero. The linear functions do not exhibit this relation. This shows that the calculated linear relationship cannot be extrapolated outside the range of measured friction potential values.

It can be concluded that the achieved results cannot be used as an input for a wet friction potential layer. Likely problems of the SKM truck are that the tyre operat-

ing conditions and tyre construction of the SKM truck differ a lot from normal tyre operation conditions.

The velocity dependency of the SKM measurements could be caused by partial aquaplaning effects because the used tyre is a slick tyre. The special dimensions of the tyre do not allow fitting a standard vehicle tyre. Another disadvantage of the SKM method is a changing tyre operating condition whenever the truck drives a corner. No additional information about the dynamic tyre operating conditions is available. A constant static wheel load is assumed. Due to all these problems, only a poor correlation between SWB and SKM measurements was found. In addition, an insufficently accurate localisation leads to large gaps in the meausred map.

4.2 RoadSTAR Measurements

The RoadSTAR test program was planned similar to the SKM measurements. This way, the two main continuous measurement methods, a constant slip based and a side force based method can be compared. Aiming to improve the correlation between the measurements and friction potential measured by the vehicle, in addition to the normal RoadSTAR test measurements with the PIARC tyre, two purpose-built tyres have been used. The test program of the RoadSTAR truck was split over three days. Each day, the truck drove the public road track three times with one of the three tyres. The measurements on the test track were conducted on two days.

In the next section, the custom built tyres are named 'Tyre A' and 'Tyre B'. These tyres had the dimensions 185/75R16 and the construction of standard car tyres. Tyre B was made from the same rubber compound as the summer tyres used on the test vehicle during the SWB measurements[2]. Tyre A had the same construction as Tyre B but used a rubber compound with expected inferior wet grip properties. Since RoadSTAR uses a gearbox to generate the braking slip at the measurement wheel, the larger effective radius of the special test tyres (334 mm instead of 315 mm) leads to a reduction of the slip from 18 % to 13 %. The pressure of the tyres has been set to 2.7 bar, which is the same pressure as used in the test vehicle. The maximum possible vertical load of 3500 N was used. This way, the tyre operating point is as close as possible to the operating point during an SWB test with the test vehicle. The measurements conducted with the PIARC tyre used the default RoadSTAR operating conditions listed in table 1.2.

[2]The exact same tyres as used on the test vehicle did not fit on the RoadSTAR truck due to their dimensions.

The data of all measurements was provided in a csv file format. The data includes a latitude and longitude value each meter. Also the corner radius is provided with the same resolution. The measurement values used to calculate the friction potential value, the wheel load, brake force and suspension position are provided as one value every 5 m. In addition, the calculated friction potential value is given. Further measurements include a temperature value and parameters about the road texture. These surface parameters are not used in the scope of this thesis. The wheel load is calculated using the data from two sensors. A 'static' part is measured by a load cell fitted along the force path of the air spring, which is used to set the nominal static load and the shock absorbers. A dynamic component is measured by an accelerometer fitted on the unsprung mass. Due to the suspension geometry, the position, which is measured by a linear potentiometer, and the horizontal force have to be used to correct the wheel load. The horizontal force is calculated by measuring the wheel load using a load cell on the drive shaft and dividing the value by the dynamic radius. Altogether, this means that four different sensors are required to calculate the friction potential value.

For a detailed analysis of the measurements, for some of the test drives also the raw data of the sensors was provided. These files also included the vehicle speed and the wheel speed, but no GNSS information. These raw data files provide one measurement value each 0.1 m.

The following sections are structured analogously to the SKM previous evaluation and focus on the provided 5 m friction potential values. A section comparing the results of the different tyres and a discussion of the provided raw data files is included.

4.2.1 Test Track

All measurements on the test track have been repeated three times. The measurement speeds 30 kph, 40 kph and 60 kph have been used. In combination with the three different tyres, this sums up to 27 different tests. 60 kph is the default measurement speed for the RoadSTAR truck. Normally, no other measurement speeds are used but tests at different speeds have been described in [18]. It is stated that measurement speeds between 30 kph and 80 kph can be considered valid. For better comparison with the SKM measurements, the velocity of 40 kph was chosen. The velocity 30 kph was added to gain information about the measurement device behaviour at these low speeds required for several parts of the public test track.

The measurement values for all three tyres can be seen in the appendix in figures C.2, C.3 and C.4. The PIARC measurements show a similar trend during all measurements. The measurements conducted with the custom tyres indicate systematic measurement

errors, which needed further analysis but could not be corrected without repeating the measurements. Possible causes for the systematic errors are discussed in section 4.2.2, when discussing the raw measurement data.

A comparison between the RoadSTAR measurement results and the SKM results shows that the sharp decrease of the friction potential around segment 100, the change from asphalt to concrete, on the first straight is not present in the RoadSTAR measurement. The friction potential decrease after segment 155 is present in both the SKM and the RoadSTAR method but it is more pronounced and present for a longer period in the RoadSTAR measurements. Since at this point a road irregularity is located, the assumption is that the measurements of both methods are affected by this excitation but that the SKM reaches stable wheel operating conditions faster than the RoadSTAR after the excitation.

Reproducibility

Due to the systematic measurement errors visible in the measurements with the custom tyres at almost all speeds, only the PIARC measurements are discussed in more detail. It was decided to use only the median value as result for the measurements conducted with the custom tyres. It seems that measurements using the special tyres are not reproducible.

Since only three repetitions of the measurement are available, only method two (equation 4.3), to calculate the average standard error has been used. The result is an increasing average standard error with increasing speed. The error at 30 kph is 0.0184 and increases to 0.02 at 60 kph. Therefore, the standard error of the RoadSTAR measurements is smaller than the error of the SKM measurements at all tested speeds.

Figure 4.6 shows the error distribution of all measurements. The included q-q plot indicates that the error distribution of the 30 kph and 60 kph measurements can be assumed to be a normal distribution. The measurements conducted with 40 kph on the other hand indicate that the probability of large measurement deviations is higher than it should be if the measurement errors were normally distributed. No reason why the 40 kph measurements exhibit this different behaviour was identified.

Velocity Dependency

Similar to the SKM measurements, an empirically derived velocity dependency is used to correct measurement speed variations. This correction is given by equation 4.4 and it would result in friction potential values higher by 0.075 (0.05) if measured at 30 kph (40 kph) compared to the 60 kph values.

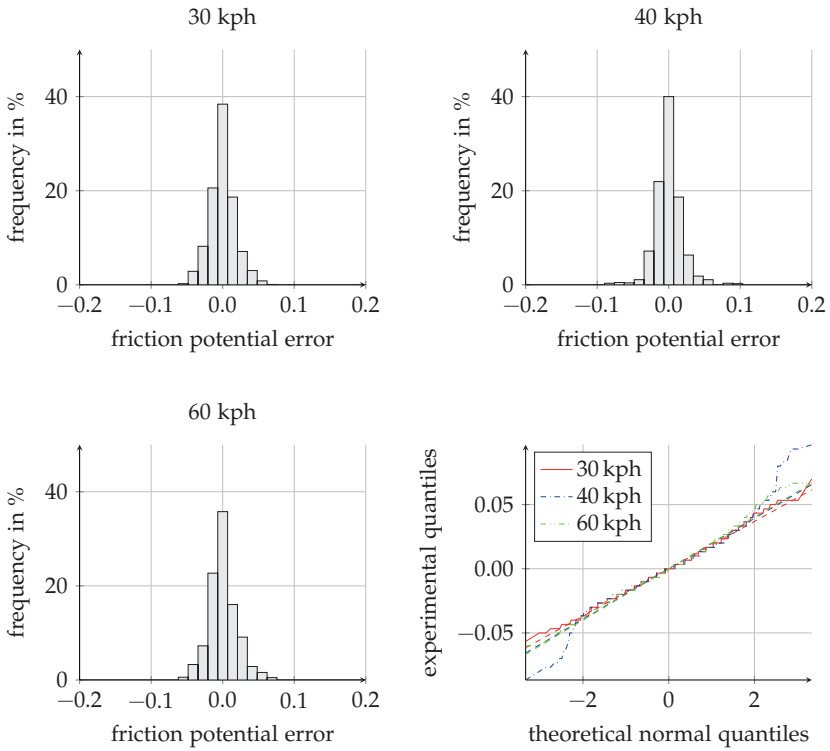

Figure 4.6: Measurement error distribution of RoadSTAR measurements on test track; bottom right: q-q-plot of error distribution

$$\mu_{\text{corr}} = \mu + (\tilde{v} - 60) \cdot 0.0025 \tag{4.4}$$

A comparison between the mean values of the PIARC tyre with the three different velocities is plotted in figure 4.7 without this velocity correction. This figure already shows that the measurements at 60 kph produce the smallest friction potential value. The mean reduction between the 60 kph and the 30 kph values is 0.043 and between 60 kph and 40 kph 0.029. Thus, the reduction between 40 kph and 30 kph is 0.014. Therefore, a linear velocity correction seems appropriate but for the test track the correction factor should be 0.0015 instead of the empirical value of 0.0025.

Since only measurement velocities between 30 kph and 60 kph are valid, the largest

error due to the velocity is 0.029. This is $1.5s_N$ of the measurement variation derived in the previous section. It is larger than the measurement spread of almost 90 % of the measurements assuming a normal error distribution. Thus, a velocity correction should be applied. Since the correction factor applicable on the test track is only 60 % of the normally applied value, a longer test track with many different surfaces is required to validate the velocity correction factor. The velocity dependency can most likely be explained by different excitation frequencies due to higher relative velocities between the rubber and the road surface. This changes the hysteresis friction. Since this friction component is also an interaction of surface texture and rubber properties, it can only be applied to the PIARC tyre and different correction factors need to be derived for the other tyres.

Keeping in mind that the custom tyres showed systematic measurement errors and that it was decided to use the median value of the three repeated measurements, the following velocity corrections for the custom tyres were derived. Tyre A shows a friction potential reduction with increasing measurement velocity but for this tyre no linear relationship is valid. The correction factor between 60 kph and 30 kph is 0.0045 and between 60 kph and 40 kph 0.0027. Calculating the correction between the 40 kph and the 30 kph measurement the value increases to 0.0082. In figure C.2, the systematic measurement error is largest for the 30 kph measurements. Therefore, it was decided to use the correction factor 0.0027. For tyre B the calculated correction factor between 60 kph and 40 kph is 0.002 and between 60 kph and 30 kph 0.0015. It was decided to use the average 0.0018 of these two correction factors. All these corrections would need to be confirmed with extensive testing on many road surfaces after the discovered systematic measurement problems are resolved.

Tyre Comparison

The last point discussed using the test track measurements is the tyre influence. The measurements of all three tyres are compared for the measurement velocity of 60 kph. The measurements are plotted in figure 4.8. The direct comparison between tyre A and B yields an average increase of 13.6 % of the measured friction potential. These tyres have the same tyre construction and operating condition. Thus, the difference can be attributed to the rubber compound only. This highlights, that it is important to know the tyre for any successful friction potential estimation method. Due to the different dimensions, the operating longitudinal slip of the PIARC tyre is larger. Since the friction decreases with increasing slip after the friction potential of the tyre perspective, this could decrease the measured friction potential. In addition, the friction potential

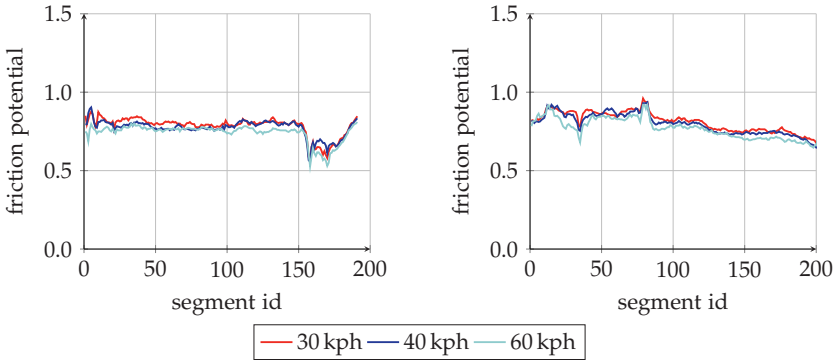

Figure 4.7: Comparison of RoadSTAR measurements with different measurement velocities using the PIARC tyre on test track; left: straight 1; right: straight 2

is affected by the different tyre construction and rubber compound. A comparison between the PIARC tyre and tyre A and B results in an increased friction potential of 1.0310 and 1.1715 respectively. Thus, the performance of tyre A is only slightly better than the PIARC tyre.

4.2.2 Public Road

The RoadSTAR measurements on the public road track were provided with one continuous measurement file for each lap. Because each tyre was driven for three laps, altogether nine measurement files are available. RoadSTAR measurements with a velocity below 30 kph were considered invalid. The measurements on the test track showed only a minor velocity dependency, so that all measurement velocities above 30 kph are considered valid.

While the RoadSTAR measurement tyre can run side-force free around large bends due to geometric constraints and body roll, small corner radii cannot be measured. The valid radii vary with driving speed and are shown in [18]. Corner radii speed combinations, which are considered invalid according to this definition, are also excluded.

Figure C.6 shows the friction potential measurements for tyre B for all valid segments. Outliers with very low friction potential values are evident in these measurements. These are reproduced on all three laps. The measurements with tyre A and the PIARC tyre plotted in figure C.5 and C.7 also show these outliers but they are not as

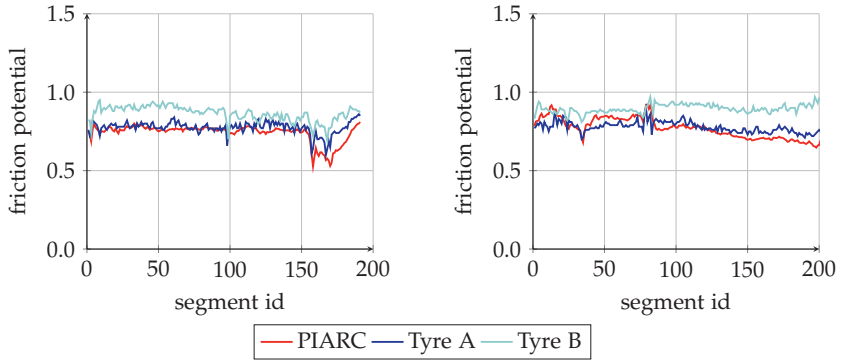

Figure 4.8: Tyre comparison of RoadSTAR measurements with velocity 60 kph; left: straight 1; right: straight 2

pronounced in these measurements.

After three laps with measurement tyre B, 89 % of the segments can be assigned a valid measurement value. On average, a single measurement results in friction potential values at 84.2 % of the segments. These numbers show that the RoadSTAR truck yields more valid measurements than the SKM truck. The reasons are that RoadSTAR can measure in most bends and does not require measurements within small velocity limits.

A comparison of all valid measurements with tyre B yields a standard deviation of $s_N = 0.0339$. This value is larger than previously calculated on the test track. One possibility for this increase is a variation of the measurement velocity between the three laps but a conversion of all measurements to the standard measurement velocity of 60 kph yields only a very minor improvement ($s_N = 0.0335$).

The quality of the roads on the lap can only be analysed using the PIARC tyre measurements, since only for these measurement tyres limit values exist. On the test track, a different velocity correction than officially used was derived. Therefore, figure 4.9 shows the friction potential distribution without any velocity correction, with the official velocity correction and with the velocity correction derived on the test track. The official warning and limit values are included as vertical lines. The velocity corrections are used on the measurements of each lap and if there is more than one valid measurement, the median value is used in the distribution plots. Applying the velocity correction reduces the friction potential variation and the measured friction potential because almost all segments are measured with velocities below 60 kph. Independent

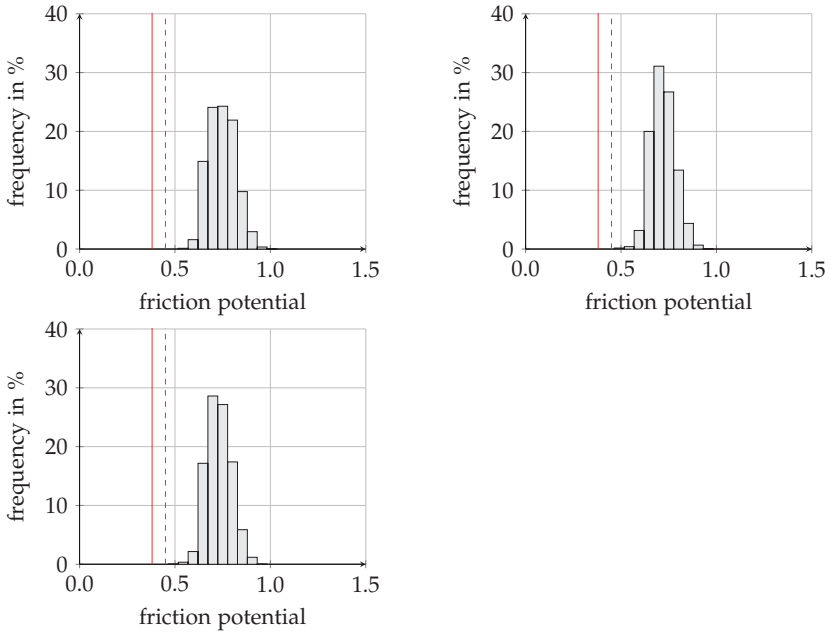

Figure 4.9: Friction potential distribution of public road track measured with RoadSTAR; top left: without velocity correction; top right: with default velocity correction; bottom left: with velocity correction derived from test track data

of the used velocity correction, the RoadSTAR measurements indicate that the measured roads are better than the threshold and warning value. Thus, RoadSTAR classifies the measured roads as even better than SKM did but both methods indicate that the measured track has to be considered rather good. If the results of SKM and RoadSTAR correlate to vehicle measurements, this also suggests that there are other road segments, where the friction potential measured with SWB should be lower, thus the influence of the road surface might even be larger than discussed in section 3.3.2.

Due to the systematic measurement errors and outliers visible in the test track and public road data, a comparison of the repeatability between the test track measurements and the measurements on public roads has been omitted. Instead, the next section will focus on some problems discovered during the analysis of the RoadSTAR measurements.

Discovered Measurement Shortcomings using Raw Data of RoadSTAR

In order to analyse the discovered measurement shortcomings, the AIT provided raw measurement files with a resolution of 0.1 m. The RoadSTAR truck needs measurements of four sensors in order to calculate the friction potential. In the raw data files, the data of all these four sensors is available separately, while only the calculation result has been available in the final result files discussed in the previous section.

Looking at the raw data, it turned out that the load cell to measure the moment is limited by the Analogue Digital Converter (ADC) at 1092 N m. Tyre B reaches this limit due to two reasons. The larger effective radius increases the lever arm. The overall better performance of tyre B than the standard PIARC tyre increased the forces, while tyre A does not reach the limit as often due to the similar performance to the PIARC tyre.

The next minor problem discovered was that in the calculation the loaded radius r_L of the tyre instead of the rolling radius r_e to convert the moment to the horizontal force is used. Thus, the moment arm used is too small, leading to an overestimated horizontal force and due to the suspension geometry an underestimated vertical force.

Next, it was discovered that the RoadSTAR measurements are severely affected by road excitation. The raw data showed that the transfer function between the second derivative suspension movement and the dynamic force has an amplification factor of around 32 but the unloaded mass of the measurement wheel setup is 75 kg. This mismatch seems due to calibration errors in the acceleration sensor. Also, it was found that only two rather weak dampers are used. A damping factor of about 0.1 is reached with tyre B. Since the vertical stiffness of the PIARC tyre is assumed smaller in the standard RoadSTAR setup, the damping factor is slightly higher[3]. All these problems concerning the vertical load of the tyre only slightly affect the standard RoadSTAR measurements, since the truck is normally used on highways, which are normally smoother than urban roads. In addition, the friction potential is averaged over distances 20 times longer than used in this evaluation. Therefore, errors due to road excitation and wrong dynamic load measurements are averaged out.

Last but not least, in the standard data evaluation process a negative load or a friction potential higher than 1.2 are set to 0. The average is then calculated including these 0 values. This correction happens most often for tyre B. Once again, averaging over longer intervals reduces the influence of these 0 values in the measurement.

[3] No vertical stiffness measurements are available.

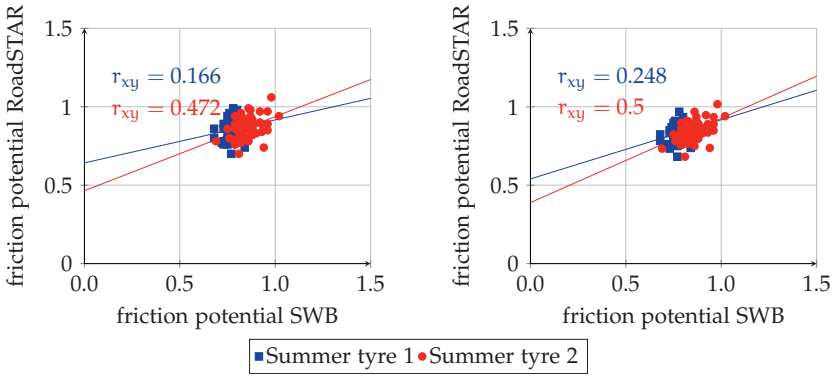

Figure 4.10: Comparison of RoadSTAR with tyre B and SWB tests on public track; left: without velocity correction; right: with velocity correction

4.2.3 Comparison with Single Wheel Braking

Despite of the discovered measurement problems in the RoadSTAR measurements, a comparison with the SWB results is conducted. The approach follows the same pattern applied for the SKM measurements, but all road renewals were finished before the RoadSTAR measurements. Therefore, only measurements after the road maintenance was finished have been compared with the RoadSTAR measurements. Once again, only SWB measurements on a wet surface and only the tyres SR1 and SR2 are used in the analysis.

Figure 4.10 shows the correlation of the RoadSTAR measurements with tyre B and the SWB measurements. On the left side, the results of tyre B without applying any velocity correction are shown, while on the right side the velocity correction derived in section 4.2.1 has been used. It can be seen that especially using the SWB measurements conducted with SR1 almost no relation between the Roadstar measurements and the SWB tests can be found. When comparing the RoadSTAR measurements with the SWB measurements of SR2, which contain more brake points, a slightly better coefficient of only 0.472 is calculated. Similar to the 80 kph measurements of the SKM measurement, part of a possible explanation is the small spread in measured friction potential at the different brake points. Another reason can be the discovered problems with road excitation discussed in section 4.2.2. In the right plot of the figure it can be seen that applying the derived velocity correction leads to a small improvement of the correlation.

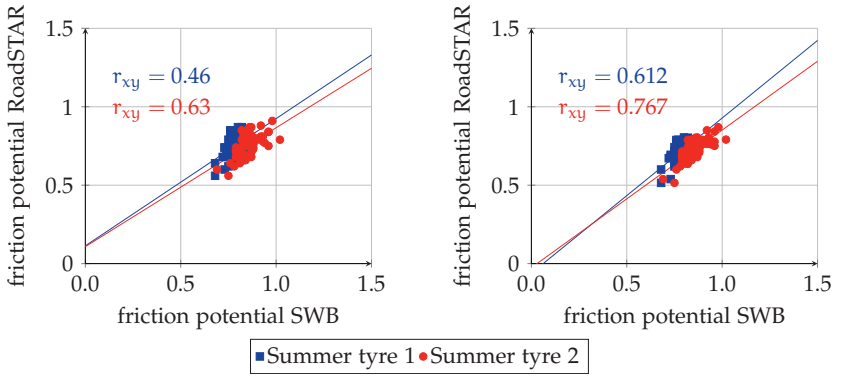

Figure 4.11: Comparison of RoadSTAR with PIARC tyre and SWB tests on public track; left: without velocity correction; right: with velocity correction

It was expected that the correlation between the SWB tests and RoadSTAR measurements with tyre B would be better than the correlation with the standard RoadSTAR measurements. The idea was that using the same rubber compound eliminates one of the main influencing factors. Since the discovered measurement shortcoming had the highest influence on the measurements with tyre B, the standard RoadSTAR measurements conducted with the PIARC tyre are also compared to the SWB tests.

These results are shown in figure 4.11. Especially the comparison with SR2 shows a good linear correlation of $r_{xy} = 0.63$. Applying the default velocity correction, the correlation coefficient improves further to $r_{xy} = 0.767$, indicating a reasonable linear relation between both measurement methods. Furthermore, the y-axis intercept is almost 0. The maximum error between the linear approximation and the RoadSTAR/SWB SR2 measurement pairs is 0.11, the mean absolute error 0.035. Assuming a normal error distribution (without any further validation or proof) results in a standard deviation of 0.0248. Using this assumption and applying a security margin of $3s_N$, the standard RoadSTAR measurements of the public road track can be used to estimate the wet friction potential of the vehicle using equation 4.5.

$$\mu_{pot} \geqslant 1.1398 \cdot \mu_{RoadSTAR} + 0.0294 - (3 \cdot 0.0248) \tag{4.5}$$

In conclusion, the RoadSTAR measurements show some promising results, making it possible to map the wet friction potential and using it inside an autonomous vehicle. Nevertheless, improvements in the measurement setup are required to improve the res-

ults using tyre A and B. The results of the RoadSTAR truck are more consistent than the SKM results. The additional measurement of the wheel load compared to the SKM truck proofed valuable. Especially the problems encountered during the RoadSTAR measurements with tyre B highlight the importance of this measurement value. The increased road unevenness on urban roads and shorter measurement intervals prevent averaging out the influence of wheel load oscillations. Thus, the static load assumption of the SKM method should be scrutinised and a measurement of this property is desirable.

The RoadSTAR truck suffered problems with the calculation of the dynamic wheel load. Nevertheless, the results with the PIARC tyre showed a rather good correlation with the SWB tests. The construction of the RoadSTAR truck allows to fit small vehicle tyres but it was discovered that the measurement range of the moment signal was exceeded. Fitting a tyre with larger stiffness highlighted the importance of sufficient damping and correct dynamic load measurements. It is expected that the correlation between RoadSTAR and the SWB tests with tyre B can be improved as soon as these shortcomings are resolved. Since in this scenario the same rubber compound is used on the RoadSTAR tyre and the test vehicle, an even better correlation than currently achieved using the PIARC tyre should be possible. In the further discussion, the continuous wet friction potential map measured with the RoadSTAR truck equipped with the PIARC tyre is used.

Although RoadSTAR is able to measure larger bend radii, measurement gaps due to small radii or low driving speed remain. These gaps in the continuous friction potential map need to be filled with reasonable safe assumptions. One possibility would be to use a methodology similar to the approach used to derive the threshold values for road maintenance. This methodology requires measuring a significant amount of the road network and fill the gaps with the minimum value measured on the network. This conservative approach results in slow driving speeds, whenever no continuous measurements are available.

5 Intermediate Layer Classification

As already seen in the accident statistics and further shown by the SWB measurements on the test course, a change from dry to damp conditions decreases the friction potential by some margin, while ice or snow massively reduces the friction potential. Therefore, in this chapter, it will be evaluated how well these road conditions can be predicted. The problem of mapping several inputs to classes is called a classification problem. Several combinations of sources for the weather information, classification methods and output classes are compared in this chapter.

The chapter starts with a description of the available input sources. After this, the rational behind the chosen output classes are given. After these three methods, which can be found in literature or are comercially available, are applied to the data. The first one is solely based on taking the road condition measured at the next Road Weather Information System (RWIS) station. This can be seen as baseline to show the improvement of the other methods. The next method is the method presented in the recent FAT project [9], although slightly different input sources were available during this project. The last method is a dedicated road-weather forecast provided by a weather forecast company for the public road track.

In the last, part two well known classification methods, the Multinomial Logistic Regression (MLR) and Artificial Neural Network (ANN) are applied in a new way to the classification problem. Several ways to tune the results of the ANN towards a conservative safe classification are presented.

5.1 Input Sources

Due to the preview requirements derived in section 1.1 as input sources, in reality, no sensor values of the own vehicle can be used. Therefore, infrastructure information or information from other vehicles has to be relied upon. The advantage of infrastructure data is that it is continuously available. A major disadvantage is, that the location the infrastructure data is generated for can be far away from the road, for which the friction potential is required. Data from other vehicles requires that a vehicle sending

relevant information via car2x is driving in front of the autonomous vehicle, which will not always be given. Another assumption which can be made is that the weather experienced by the vehicle stays constant for the next few hundred meters and therefore no preview information is required. In this thesis, the sensor data of the test vehicle is used as if it was received from another vehicle driving in front or as if this assumption is always true. Two different sets of input sources are tested. In the first set, only infrastructure data is used and in the second set, the vehicle data is included in the inputs. A list of inputs, their source and their use in the different discussed methods can be found in table 5.1.

5.1.1 Road Weather Information System

Road weather information systems use special weather stations located at the sides of major roads. Their main use is to help winter maintenance and traffic management. In Germany, the data of many RWIS stations is distributed by the Deutscher Wetterdienst (DWD) via a FTP server. The used data formats are either an American Standard Code for Information Interchange (ASCII) format called SH10 [143] or the binary format BUFR [144]. Every 15 minutes, new RWIS data is available. The delay between the measurement and availability of the data is at most a few minutes and has therefore been neglected.

The number and types of sensors available at each RWIS station vary. A fully equipped station consists of several sensors, which provide information about the atmospheric weather and the road condition. The air temperature is normally measured in 2 m height. A surface temperature and up to three underground temperatures in different depths are measured. Some RWIS stations can actively cool a small surface part down and measure the freezing point. This way, the salt content on the road can be calculated. RWIS stations can measure the amount of precipitation, water height on the road and the intermediate layer type. Furthermore, the humidity and dew point are measured. Other sensors measuring the wind direction and speed as well as visibility can be available, but most stations are only fitted with a small subset of the described sensors. Therefore, it was decided to use the measured properties which are likely available on many stations. The evaluated methods focus on the five inputs air temperature, dew point temperature, humidity, surface temperature and road condition. The possible road conditions output by the RWIS station vary depending on the equipped sensors and used data format.

For the purpose of this project, the road conditions have been mapped to the three different states: dry, wet and snow/ice. The nominal road condition is mapped to

three input variables, one for each road condition. The variable is set to one if the road condition is measured and zero otherwise. Only one of the three inputs can be one at the same time, this is called one-hot encoding.

The RWIS station used for this project, the closest to the measured route, is the station with the short name Q441. It is located on a motorway crossing. The station provides the five input properties specified. During the conducted measurements, the measured road condition was always either dry or wet. The road condition snow/ice was never reported.

In addition to the measurement values, the age of the reported data and the distance to the RWIS station have been used as inputs to some of the methods. Therefore, nine inputs of the RWIS station are available as features in the machine learning methods.

5.1.2 Radar

The used radar data is also provided by the DWD. Three different radar products are used as input source. These products are called pg [145], rw and sf [146].

The pg product is provided in the Binary Universal Form for the Representation of meteorological data (BUFR) format and contains the reflexivity of the clouds in six different decibel levels. A new measurement is provided every 5 min. The resolution of the data is 2 km $\times$ 2 km. The data is available with almost no delay.

The rw and sf products combine radar measurements and ground stations to provide the amount of precipitation. The rw data provides amount of precipitation during the last hour and sf during the last 24 h. This precipitation data is provided in a format called runlength. It consists of an ASCII header and a binary data section. The data resolution is 1 km $\times$ 1 km and is only available with a delay of more than half an hour. Therefore, it was decided to use only data, which is at least 1 h old as input. This constant one hour offset has been subtracted from the input data age.

Based on the GNSS position of the vehicle, the correct pixel in the radar image is chosen. For each of the three radar products, the value of this pixel and the age of the data are included in the input vector.

5.1.3 Vehicle Data

Vehicles are fitted with sensors which give indications about the current weather situation. The two common sensors equipped are an air temperature sensor and a rain sensor, which is used for automatic wiper control. It was the aim to use both these sensors as input for the machine learning approaches.

The use of the outside temperature is straightforward.

Using the raw rain sensor signal is difficult. For example, the measured values depend on the wiper position. If the wiper is just in front of the rain sensor surface, an increased water height is measured because the wiper is pushing a thin water layer forward. After the wiper has passed, no water is measured because it had just been removed by the wiper. Therefore, instead of using the raw rain sensor signal, it was decided to simply count the wiper cycles and thus use the results of the automatic wiper control software. During all test drives, the wiper setting was set to the most sensitive automatic control setting. In order to filter very short wiper velocity changes, floating 30 s intervals were used to calculate the value wiper cycles per minute. Finally, this value is used as input in the machine learning methods.

In general, using the sensors of the test vehicle does not fulfil the preview requirements. A valid assumption might be that the current weather is the same in the next few seconds and meters making the measured values useable as a preview. These sensor data can be sent via car2x from another vehicle driving in front. In this case, the data would fulfil the spatial preview requirement. But there is no guarantee that another vehicle has driven the same road in front of the vehicle requiring the information. Therefore, the vehicle data should only be used as additional inputs. This is empoyed as a second option in the machine-learning models.

5.2 Ground Truth

To validate any prediction of the road condition, a correct ground truth is necessary. Before the build up of the test vehicle, the RoadEye sensor used in the 'Friction' EU-project [66] and the MARWIS sensor were considered as ground truth sensors. Both sensors operate with the same measurement principle measuring the different absorption properties of water in different near-infrared frequencies. Laboratory experiments and more details of this measurement principle can be found in [147].

It was decided to use the MARWIS sensor. The main reason was especially because of the additional output values road surface temperature and water height. Furthermore, also the classification of the road condition seemed superior using this sensor. The test vehicle was equipped with two MARWIS sensors. Due to their size, they are mounted on a bike rack behind the vehicle. Since the water displacement of the wheels would affect the measured water height, the sensors were mounted in between the wheel tracks.

Initial tests with the MARWIS sensors showed that the sensor is not able to de-

Table 5.1: Complete feature vector used in the classification methods

			Method					
Property	Source	Type	Next RWIS	FAT Method	MLR	MLR with vehicle data	ANN	ANN with vehicle data
Air Temperature	RWIS	real		x	x	x	x	x
Surface Temperature	RWIS	real	x		x	x	x	x
Dew Point Temperature	RWIS	real		x	x	x	x	x
Humidity	RWIS	real		x				
Intermediate Layer	RWIS	class	x	x	x	x	x	x
Distance	RWIS	real					x	x
Data Age	RWIS	real					x	x
Reflectivity	Radar (pg)	1-6			x	x	x	x
Data Age	Radar (pg)	real					x	x
Precipitation 1h	Radar (rw)	real			x	x	x	x
Data Age	Radar (rw)	real					x	x
Precipitation 24h	Radar (sf)	real			x	x	x	x
Data Age	Radar (sf)	real					x	x
Air Temperature	Vehicle	real		x		x		x
Wiper Cycles	Vehicle	real		x		x		x

termine the correct road condition in a sufficient number. Measurement problems of several available sensors including the MARWIS sensor were also observed in laboratory tests by other researchers [148]. Especially during the SWB measurements, it was discovered that on the one hand very small water layers, which already impacted the friction potential and were detectable by the driver, were labeled as dry. On the other hand, dry roads were classified as damp/wet. Especially lane markings were identified as wet. In case of larger water heights on the road, the MARWIS classification seemed trustworthy. In the laboratory tests [148], it has been shown that the measured water height is most often underestimated. Since no ground truth of the water height was available during this research, water height measurements of MARWIS were not validated.

Due to the short-comings of the MARWIS sensor, several different methods to de-

termine the correct road condition were tried. The first approach was to use the road condition most often measured during the single wheel braking interval as ground truth. The measurements of both MARWIS sensors were used together. Because these results were not satisfying, and classifying a wet road as dry would be a safety risk, the next tested approach was to use the worst case road condition measured with either of the sensors in the last 30 s as ground truth. This method proved far too pessimistic in the labeling of the road condition. Only seldomly roads were labeled dry. One reason discovered for this behavior is, that driving over white road markings always resulted in wet measurements. In the city parts of the tracks, almost every 30 s the car is driven over a white direction arrow or a white stopping line, pedestrian crossing or similar.

Table 5.2: Mapping of MARWIS road condition to manually labeled intermediate layer

MARWIS Road Condition	Manually Labeled Intermediate layer
Dry	Dry
Damp	Wet
Wet	Wet
Ice-covered	Snow/Ice
Snow-/Ice-covered	Snow/Ice
Chemically wet	Wet
Critically wet	Wet
Snow-covered	Snow/Ice

Finally, it was decided to manually label all measurements using dash cam footage. In case of measurements labeled as snow/ice by MARWIS, the measured friction potential was also used as an indicator. If the road seems wet but there is no further reduction in the friction potential, the ice values are labeled wet. In some cases, MARWIS even labeled a dry road as icy.

Manually labeling the intermediate layer does not allow to set the class based on the measured water height. Therefore, the measurements were only assigned to the classes dry, wet and snow/ice. In order to evaluate the MARWIS measurement performance, the eight MARWIS output classes also have to be labeled according to these three classes. The mapping shown in table 5.2 has been used in the evaluation of the MARWIS method. This mapping is applied before the final determination of the most often measured road condition. Only the first method to use the MARWIS sensors has been used to evaluate the performance of the sensor. The results can be seen in table 5.3. The columns indicate the number of measurements labeled by MARWIS in the category and the rows the number of measurements labeled manually in the category. The main diagonal shows the number of measurements labeled correctly by

MARWIS. The road condition is classified correctly in about 77 % of the time. The table shows clearly that the main error source is, wet roads being labeled as dry.

During winter, the road condition of all measurements is influenced by road maintenance due to plowing and gritting activities. In order to exclude this maintenance from the ground truth[1] if the manually labeled road condition is wet and one of both equipped MARWIS sensors measures a negative road surface temperature, the road condition is labeled as ice/snow. This correction converts 425 wet measurements to snow/ice measurements. Altogether, the collected basic ground truth data consists of 2310 dry, 1831 wet and 428 snow/ice measurements.

The accident statistics show, that aquaplaning is the cause of a significant amount of accidents. This means, that while the water height is irrelevant as long as it is below a critical height, which also depends on the vehicle speed, it needs to be considered in order to include a warning if the available friction potential is reduced due to aquaplaning. Since the critical water height depends on these mentioned factors and no validation of the measured water height by MARWIS has been conducted, a rather conservative water height of 0.5 mm is used as critical water height. This was the minimal water height for aquaplaning to appear according to [120]. In the extended ground truth data, a fourth label is introduced accordingly named 'standing water'. This label is set, whenever the manual label in the basic ground truth data is wet and at least one of the sensors has measured a water height above the critical value. Only 22 of the wet measurements move into this class.

Table 5.3: Comparison between manually labeled and MARWIS measurements; columns: MARWIS; rows: manual label

		MARWIS		
		Dry	Wet	Snow/Ice
Labeled	Dry	2242	53	15
	Wet	790	1283	183
	Snow/Ice	0	0	3

5.3 Classification methods

In this section, several methods to predict the correct intermediate layer have been evaluated. First, the nearest road weather station measurement was used as a base

[1] There is no guarantee that the maintenance took place and the weather sources, except the RWIS station, do not know anything about road maintenance activities.

line of the prediction. The next method uses a physical weather model to predict the road condition. The next three methods are based on machine learning techniques and use the input data discussed at the beginning of this chapter. The first of the three methods presented uses the solution developed in [9], which is loosely based on logistic regression. The second method describes a multinomial logistic regression approach. Third, a non-linear classification method, an ANN, is trained to predict the class.

The last three methods require data to train the models. The first method can be found in [9], while the other two methods are new applications to the intermediate layer classification problem. For all three methods, 60 % of the available input sets are used as training data and the remaining 40 % to test the performance of the method. The data has been split randomly between the training set and the test set, but the ratio of samples of each class has been kept the same in the training and the test data. Especially, using the four classes (dry, wet, standing water, snow/ice), which includes the class for possible aquaplaning, the data set is heavily imbalanced. Correctly identifying the classes with only a few training and test samples is important. For example predicting an icy road as wet poses a safety risk, while wrongly classifying a wet road as icy only set a very low target speed. Therefore these under-represented classes have to be handled with special care. This is discussed for the neural network in section 5.3.2. The same training and test data set are used in all following machine learning methods.

5.3.1 Established Intermediate Layer Classification Methods

Three different readly available methods have been used to classify the intermediate layer. The first method relies on the measurements of the next RWIS station. The second uses a comercially available road weather forcast. The third method is based on [9].

Next RWIS Station

Based on the assumption that the weather stays the same over larger spatial regions, and that it only changes slowly most of the time, using the latest measurement data of the nearest station should provide good results and a good base line to compare it with the other methods. The classified road condition measured by the RWIS station is affected by winter road maintenance, which resulted in no measurements of the road condition snow or ice. Therefore, similarly to the ground truth data, a wet road

condition in combination with a negative surface temperature has been relabeled to snow/ice. Table 5.4 shows the results of this approach. During 79 % of the measurements, this method would provide the correct road condition, but it seems problematic that using this method, in most instances a snow/ice labeled intermediate layer is predicted as wet instead of beeing classified correctly. This indicates that the RWIS station is in a warmer spot than many other brake points most of the time. Wet road conditions are labeled dry as often as dry road conditions wet.

The used RWIS provides no information about the water height. Therefore, using this method no hydroplaning warning can be provided. Thus, no results for the four classes are given.

Table 5.4: Confusion matrix using the nearest RWIS station to classify the road condition

		Prediction		
		Dry	Wet	Snow/Ice
Labeled	Dry	1930	319	61
	Wet	305	1519	7
	Snow/Ice	5	263	160

Road Weather Forecast

There are several road weather forecast products commercially available. These products focus on predicting the road condition for winter road maintenance. The inputs of these models include global weather models and information of RWIS stations. They incorporate further local information about the road. These are collected using measurements along the track. The first of these measurements is called thermal mapping. During this measurement, a mobile pyrometer is used to determine the heat capacity of the road surface and ground [149]. Another measurement uses a fish eye camera mounted to the vehicle to determine the so called sky view factor [150]. This property describes the occlusion of the horizon and can be used together with the sun position to calculate shadows on the road. Additional information like land use or traffic data can be incorporated in these models. The model available for the public road track used for testing provided forecast data once an hour. The comparison of this model with the manually labeled truth shown in table 5.5 used the latest available forecast data. The data was only available starting in the first week of February, therefore the number of observations is lower.

Using this forecast, 75 % of the forecasted road condition is correct, which is less than the 79 % achieved using the nearest RWIS station. Although the overall accuracy

of the weather forecast seems worse, looking at the most dangerous intermediate layer snow and ice, the forecast is able to predict this correctly in 47 cases instead of only 8 cases predicted by the RWIS. By comparison of the RWIS results with the results of the forecast, it can be seen that the forecast predicts the road condition dry too often.

This incorrect road condition prediction could be improved by setting all road conditions with forecasted negative road temperatures to ice. The results of this correction can be seen in table 5.6. Now 83 % of all 190 snow or ice cases are correctly predicted as snow or ice. This correction also introduces many false positives, since whenever the road temperature is negative the road condition snow or ice is assumed. This increase is most visible in the 111 dry cases now predicted as snow or ice.

A direct comparison to the RWIS station provides the conclusion, that the weather forecast is better at predicting negative road surface temperatures at the examined location, but the RWIS is better at predicting a wet road surface. One possible reason for this behaviour is, that winter road maintenance often uses a water-salt solution during gritting [151] , which can change a dry road to a wet road without the weather being the reason. The RWIS location experiences similar winter maintenance as the rest of the tested track, thus it can measure the correct road condition more often.

Table 5.5: Confusion matrix using a road weather forecast to classify the road condition

		Prediction		
		Dry	Wet	Snow/Ice
Labeled	Dry	1800	314	6
	Wet	219	599	148
	Snow/Ice	141	2	47

Table 5.6: Confusion matrix using a road weather forecast with all negative road temperatures set to snow/ice road condition

		Prediction		
		Dry	Wet	Snow/Ice
Labeled	Dry	1769	314	37
	Wet	216	599	151
	Snow/Ice	30	2	158

Method based on FAT Project

The method developed in the FAT Project 'Unfallvermeidung durch Reibwertprognose' [9] (Accident prevention with the help of a friction potential prediction) to estimate the

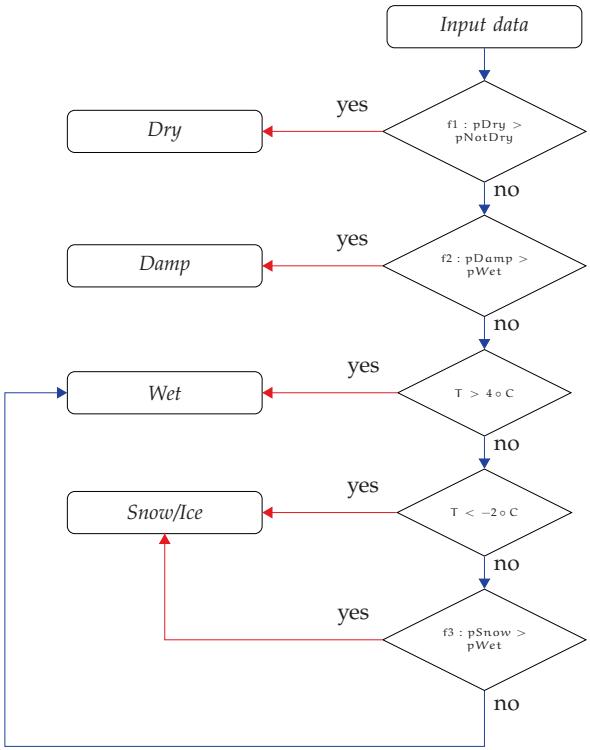

Figure 5.1: Flow diagram of FAT method described in [9]

correct intermediate layer is loosely based on logistic regression functions and some empirically derived rules. The problem of classifying the road condition correctly is splitted into several binary decisions. These are shown in the flow diagram in figure 5.1. In the first level, the data is split into the two categories dry/not dry. After this, all data classified as not dry is further split into the categories damp and worse than damp. Finally, the data in the worse than damp category is split into the categories wet or snow and ice. Thus, in the project four similar categories to the once defined in this thesis were used.

The data at each level is split into two categories using different input values. The function f1 uses the inputs humidity, dew point difference, air temperature and wiper activity. The dew point difference is the difference between the dew point temperature

measured at the station and the air temperature measured at the vehicle. A small difference indicates a high humidity at the location of the vehicle.

In the second level, the output was always hard-coded to output the condition damp if the nearest RWIS provided this road condition. The RWIS used in this project was not able to distinguish different wet road conditions, making applying this rule impossible. Therefore, this hard-coded decision has been omitted. The decision function uses the inputs humidity, air temperature at the vehicle, road condition and wiper activity.

The last decision function f3 uses the humidity, air temperature, dew point difference, road condition and wiper activity. The decision function of the last level is only used if the air temperature measured at the vehicle is below 4 °C and above −2 °C. Whenever the temperature is below −2 °C, the output is hard-coded to the class snow or ice. If the temperature is above 4 °C, the output can never be inside this category[2].

The decision functions f1, f2 and f3 are based on a weighted sum of binary functions each based on one input variable F. These decision functions have the shape of equation 5.1. EIML denotes the estimated intermediate layer class and F the input value used for the decision. The parameters a_{FAT}, b_{FAT}, c_{FAT} are optimised using the least square error function.

Finally, each of the optimised error functions is weighted by equation 5.2. Thus, the probability of an input vector $\mathbf{F}$ consisting of several features F belonging to class EIML can be calculated with equation 5.3. Instead of applying the parameters provided in the project report, new decision functions have been trained. The main reason for this was that the wiper signals differ. But it was also apparent that the RWIS road condition was different, since the one used in this project never showed the road condition ice. In addition, different wet classes are used compared to [9]. The FAT project decided between a damp and a wet intermediate layer, while the method is used here to distinguish a wet road from standing water.

$$P^{F}_{\mathrm{EIML}}(F) = \frac{c_{FAT}}{1 + a_{FAT} e^{-b_{FAT} F}} \tag{5.1}$$

$$G_{w}{}^{F}_{\mathrm{EIML}}(F) = \frac{1}{4 P^{F}_{\mathrm{EIML}} (1 - P^{F}_{\mathrm{EIML}})} \tag{5.2}$$

$$P_{\mathrm{EIML}}(\mathbf{F}) = \frac{\sum_{i=1}^{M} G_{w}{}^{F}_{\mathrm{EIML}}(F_i) P^{F}_{\mathrm{EIML}}(F_i)}{\sum_{i=1}^{M} G_{w}{}^{F}_{\mathrm{EIML}}(F_i)} \tag{5.3}$$

[2]This is an important limitation. Although snow/ice with air temperature above 4 °C was not encountered during the measurements discussed in this project, other RWIS stations show, that even if the air temperature is above this value, the surface temperature can be below 0 °C. Thus, a snow or ice intermediate layer can be possible in reality.

Every decision function P^{F}_{EIML} has been optimised using the training data set.

These results of predicting the test data set with the trained model can be seen in table 5.7. 81 % of the test data sets are labeled correctly. This is a slight improvement over the 79 % correctly classified using the nearest RWIS, even though the RWIS station data was only used to differentiate three classes, which is easier than the four classes problem.

A correct classification of the class standing water proves difficult using the method. No standing water labeled test data set is detected correctly. Most of them are classified as wet and two even as dry. The reason for the wrong classification of standing water can be manifold. The small amount of samples in the data set leads to a very small influence of mis-classifications on the overall error. Other reasons could be that the labeling of the standing water samples is wrong. They solely depend on the MARWIS measurements because no other ground truth was available. The identified problems of MARWIS classifying the correct road condition are likely caused by wrong water height measurements. These problems could also lead to a mis-labeling between wet and standing water. The final possible reason is that the used input data is not sufficient to discriminate between wet surfaces and standing water. Not only large amounts of precipitation but also insufficient drainage is required to lead to standing water on the road. The input data only covers the precipitation part. All other methods discussed in the next sections exhibit the same problems differentiating between wet and standing water.

Table 5.7: Confusion matrix using method described in FAT project [9]

		Prediction			
		Dry	Wet	Standing Water	Snow/Ice
Labeled	Dry	796	102	0	26
	Wet	143	581	0	0
	Standing Water	2	7	0	0
	Snow/Ice	24	41	0	107

Due to the problems of classifying wet and standing water, decision functions f2 and f3 were combined to a new decision function $\tilde{f2}$, which uses humidity, air temperature, dew point difference, road condition and wiper activity to decide between the combined class wet/standing water and snow/ice. The hard coded temperature limits are also used in this decision. The results of this three classes problem can be found in table 5.8. The correct classification increases by another 0.5 %.

Table 5.8: Confusion matrix using method described in FAT project [9] reduced to 3 classes

		Prediction		
		Dry	Wet	Snow/Ice
Labeled	Dry	796	102	26
	Wet	145	588	0
	Snow/Ice	24	41	107

5.3.2 Application of Classification Methods

In this section, two classification methods are applied to the classification problem. Although the methods are well known, these methods have not yet been applied to the intermediate layer classification problem using the inputs applied in this thesis.

Multinomial Logistic Regression

The next two sections use machine-learning models to solve the classification problem. A detailed introduction to these methods can be found in [152]. Only a short introduction to all neccessary equations is provided. $P(X = x)$ describes the probability of a random variable X having the outcome x. In case of more than one random variable, the probability can be described by the joint probability (equation 5.4).

$$f(x, y) = P(X = x, Y = y) \tag{5.4}$$

The probability of an outcome of $X = x$ given the condition $Y = y$ can be written by the conditional probability $P(X = x|Y = y)$. The Bayes' theorem (equation 5.5) relates the conditional probabilities $P(X|Y)$ and $P(Y|X)$.

$$P(X = x|Y = y) = \frac{P(Y = y|X = x)P(X = x)}{P(Y = y)} \tag{5.5}$$

If x is a binary variable with the possible outcomes $x \in \{0, 1\}$, the probability of the possible outcomes can be described by $P(x = 1|\eta_D) = \eta_D$ and $P(x = 0|\eta_D) = 1 - \eta_D$. This probability distribution can be calculated by equation 5.6 and is called Bernoulli distribution, where η_D is a parameter of the distribution.

$$Bern(x|\eta_D) = {\eta_D}^x(1 - \eta_D)^{1-x} \tag{5.6}$$

Given a set D with N observations $D = \{\mathbf{F}_1, \ldots, \mathbf{F}_N\}$ of a Bernoulli distribution $Bern(\mathbf{F}|\eta_D)$, the probability that the observations are drawn from the distribution with parameter η_D, is calculated by

$$P(D|\eta_D) = \prod_{i=1}^{D} \eta_D{}^{x_i}(1-\eta_D)^{(1-x_i)} \tag{5.7}$$

and is called likelihood function. The parameter η_{DML} maximising this function provides the best approximation of the 'true' distribution. Instead of finding the maximum of equation 5.7, the problem can be simplified by optimising the logarithm of this equation called log-likelihood.

Applying the Bayes' Theorem to a binary classification problem, the conditional probability that an observation x belongs to class O_1 can be written as

$$P(O_1|x) = \frac{P(x|O_1)P(O_1)}{P(x|O_1)P(O_1) + P(x|O_2)P(O_2)} \tag{5.8}$$

This equation can be reformulated as the logistic sigmoid function sig (equation 5.9)

$$sig(\Phi) = \frac{1}{1+\exp(-\Phi)}, \tag{5.9}$$

where Φ is defined as the log odds

$$\Phi = \ln(\frac{P(O_1|\mathbf{F})}{P(O_2|\mathbf{F})}). \tag{5.10}$$

Logistic regression assumes a linear relationship between the log odds Φ and the observations, also called feature vector $\mathbf{F}$. The weight vector $\boldsymbol{w}$ assigns the weights to the features.

$$\Phi = \boldsymbol{w}^T\mathbf{F} \tag{5.11}$$

In order to include a bias, the feature vector is extended by $\mathbf{F}^0 = 1$. Therefore, $M+1$ parameters have to be found, where M is the number of independent variables –features – in each observation $\mathbf{F}_i$.

Using a training set with N observations $D = \{\mathbf{F}_1, \ldots, \mathbf{F}_N\}$ and the correct class $\mathbf{o} = \{o_1, \ldots, o_N\}$ with $o_i \in \{0, 1\}$ the probability of observation $\mathbf{F}_i$ belonging to class O_1 given the parameters $\boldsymbol{w}$

$$y_i = P(O_1|\mathbf{F}, \boldsymbol{w}) = sig(\boldsymbol{w}^T\mathbf{F}_i) \tag{5.12}$$

equation 5.7 can be rewritten as

$$P(\mathbf{o}|\boldsymbol{w}) = \prod_{i=1}^{N} y_i^{o_i}(1-y_i)^{(1-o_i)}. \tag{5.13}$$

The maximum of this function can be found by using an iterative optimisation method.

The extension of the binary logistic regression method is straight forward. A reference class O_k can be chosen and the log odds of all classes compared to this class can be modeled by a linear function. In the case of U classes, the vector becomes a matrix $\boldsymbol{w} \in \mathbb{R}^{(U-1)\times(M+1)}$. The conditional probability of the last class can then be calculated by

$$P(O_k|\boldsymbol{F}_i) = 1 - \sum_{j=1}^{U-1} P(O_j|\boldsymbol{F}_i). \tag{5.14}$$

Based on the log-likelihood function of a multinomial distribution, the function

$$P = \sum_{i=1}^{N} \sum_{j=1}^{U} o_{ij} \ln(y_{ij}) \tag{5.15}$$

is maximised. o_{ij} is 1 if the i-th observation belongs to class j, otherwise it is 0. y_{ij} describes the probability $P(O_j|\boldsymbol{F}_i)$.

The resulting conditional probability is called softmax function (equation 5.16).

$$P(O_k|\boldsymbol{F}) = \frac{\exp(\Phi_k)}{\sum_{j=1}^{K} \exp(\Phi_j)} \tag{5.16}$$

Instead of calculating $(U-1)\times(M+1)$ parameters, the used model of the python package scikit-learn [153] calculates $U \times (M+1)$ parameters and uses the additional constrained that $\sum_{j=1}^{U} P(O_j|F) = 1$. Both formulations can be easily converted into each other.

In the default configuration, sklearn adds a regularisation term to the log-likelihood functions. This regularisation term penalises large values in the parameter vector $\boldsymbol{w}$. This technique is used to prevent over-fitting of the model to the training data. Thus, it should decrease the prediction performance during training but improve the performance when evaluating the unknown training set. The effect of different regularisation methods has not been studied in this project. Therefore, the regularisation has been switched off.

The features used as input for the logistic regression are the data from the RWIS and radar but not the distance and age of the data, since assuming a linear relationship of improving the odds of one class based on this data seemed unreasonable. The humidity and dew point contain the same information and can be converted into each other based on the temperature. Therefore, it was decided to drop this redundant

information and only use the humidity as input. This results in seven inputs if no vehicle data is used or nine inputs when the measured temperature and wiper activity are included in the inputs.

The results of only using weather data as input and three output classes can be seen in table 5.9. This multinomial logistic regression method increases the correct classification to 83.75 %, which is better than all previously discussed methods. Including the measurements of the vehicle, the correct classification rate can be improved to 84.8 %.

Table 5.9: Confusion matrix using multinomial logistic regression for 3 classes without vehicle data

		Prediction		
		Dry	Wet	Snow/Ice
Labeled	Dry	790	77	57
	Wet	120	603	10
	Snow/Ice	21	12	139

Table 5.10: Confusion matrix using multinomial logistic regression for 3 classes with vehicle data

		Prediction		
		Dry	Wet	Snow/Ice
Labeled	Dry	825	52	47
	Wet	143	588	2
	Snow/Ice	22	12	138

In case of the four output classes, multinomial logistic regression based on weather data only classifies all standing water data sets as wet. These results are shown in table 5.11. Including the vehicle data (table 5.12), more inputs are labeled as dry. This leads to one example of standing water predicted as dry. This shift towards the dry label is also observable for the three classes problem.

Artificial Neural Network

ANNs are a non-linear machine-learning method. The network is formed by many artificial neurons, also called units. These units are non-linear activation functions, mapping a weighted sum of inputs to an output value. For example

$$z_j = f(\sum_{i=1}^{I} w_{ji} x_{in,i} + w_{j0}) \tag{5.17}$$

Table 5.11: Confusion matrix using multinomial logistic regression for 4 classes without vehicle data

		Prediction			
		Dry	Wet	Standing Water	Snow/Ice
Labeled	Dry	792	75	0	57
	Wet	123	591	0	10
	Standing Water	0	9	0	0
	Snow/Ice	21	12	0	139

Table 5.12: Confusion matrix using multinomial logistic regression for 4 classes with vehicle data

		Prediction			
		Dry	Wet	Standing Water	Snow/Ice
Labeled	Dry	826	51	0	47
	Wet	142	580	0	2
	Standing Water	1	8	0	0
	Snow/Ice	22	8	0	138

describes the output of the j-th neuron, which has I inputs $x_{in,i}$. The inputs x_{ini} can be inputs from a previous layer of neurons or the feature vector **F**. Thus, the neurons can be concatenated to a network like shown in picture 5.2. This network maps the feature vector **F** to one or many outputs.

The network can consist of an arbitrary number of layers, which can be connected arbitrarily. In this thesis, two layers each with the same number of units as the feature vector size were used. All layers were connected densely, which means that each output of a unit is an input of each unit in the next layer. The last layer of the network has to have the same number of units as the number of classes, in our case either three or four.

Many different non-linear functions can be used as function f like the sigmoid function 5.9. In the neural network used for the classification tasks, the rectified linear unit (equation 5.18) has been used.

$$z_j = max(0, \sum_{i=1}^{I} w_{ji} x_{in,i} + w_{j0}) \tag{5.18}$$

Neural networks can be used to approximate functions or classification tasks depending on the output layer. In order to use the network for a classification task, where one of several possible classes has to be selected, the softmax equation 5.16 is

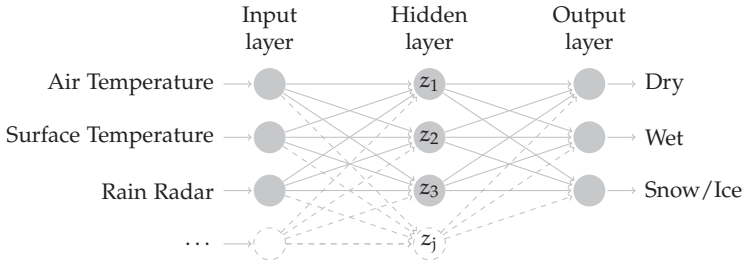

Figure 5.2: Structure of the ANN

used in the output layer. According to the multinomial logistic regression, the negative log-likelihood function (equation 5.15) is used as error function of a non-linear optimiser. The tensorflow package [154] in combination with Keras [155] has been used to train the neural network.

Table 5.13: Confusion matrix using artifical neural network for 3 classes without vehicle data

		Prediction		
		Dry	Wet	Snow/Ice
Labeled	Dry	826	60	38
	Wet	104	625	4
	Snow/Ice	17	12	143

Since the neural network finds a non-linear mapping between the inputs and the correct output class, the inputs distance and age of the data can be used. It can be speculated that the age of the input data and/or the distance to the weather station providing the input data can be useful additional information. A likely non-linear relationship would be to trust the rain radar data more than the weather station data, the further the vehicle is away from the weather station. Similarly, trusting up to date vehicle data more than old data from the weather station is imaginable.

Table 5.14: Confusion matrix using artifical neural network for 3 classes with vehicle data

		Prediction		
		Dry	Wet	Snow/Ice
Labeled	Dry	860	25	39
	Wet	145	583	5
	Snow/Ice	22	6	144

The neural network results in a further improvement over the Multinomial Logistic Regression (MLR). Without the use of vehicle data, 87 % of the test data can be separated into the classes dry, wet and snow/ice correctly (see table 5.13). Surprisingly, the inclusion of the vehicle measurements shown in table 5.14 slightly decreases the correct classification down to 86.7 %.

Table 5.15: Confusion matrix using artificial neural network for 4 classes without vehicle data

		Prediction			
		Dry	Wet	Standing Water	Snow/ice
Labeled	Dry	813	78	0	33
	Wet	94	622	0	8
	Standing Water	0	9	0	0
	Snow/ice	16	9	0	147

Table 5.16: Confusion matrix using artificial neural network for 4 classes with vehicle data

		Prediction			
		Dry	Wet	Standing Water	Snow/ice
Labeled	Dry	835	41	0	48
	Wet	124	595	0	5
	Standing Water	0	9	0	0
	Snow/ice	15	10	0	147

Despite of the best performance of the discussed methods, the neural network is not able to differentiate standing water and wet. The network labels all standing water cases as wet. The overall correct classification accuracy of both variants without vehicle data (table 5.15) and with vehicle data (table 5.16) is in both cases just over 87 % and thus comparable to the results with three output classes.

Table 5.17: Confusion matrix using artificial neural network for 4 classes with vehicle data with different sample weights depending on class frequency in training data

		Prediction			
		Dry	Wet	Standing Water	Snow/ice
Labeled	Dry	812	33	0	79
	Wet	98	593	17	16
	Standing Water	0	7	2	0
	Snow/ice	6	8	1	157

All discussed methods cannot classify standing water correctly. Since classifying a road with aquaplaning risk as a wet road can be a safety risk, two modifications of

the neural net algorithm have been implemented to rectify this problem. Several approaches to handle machine learning with imbalanced data are discussed in [156]. A cost-sensitive approach is used to counter the small number of samples of the class standing water included in the data set. This is achieved by modifying the error function of the optimiser, which is based on equation 5.15 by multiplying each sample error with another factor $l(o_i)$. The new error function is shown in equation 5.19. The new factor $l(o_i)$ scales the error proportional to the inverse of the frequency the class j has in the overall data set. This way, the costs of predicting a rare class wrong is increased compared to an error appearing in the classification of a common variable. The application of this factor leads to the results shown in table 5.17. This approach results in the correct classification of two standing water cases, while the majority is still labeled as wet. At the same time, the classification accuracy drops down to 85.5 %.

$$E(\boldsymbol{w}) = -\sum_{i=1}^{N}\sum_{j=1}^{U} l(o_i) o_i \ln(y_{ij}) \tag{5.19}$$

The last approach multiplies another factor $u(i,j)$ based on the predicted class i and the true class j of the data set. This way, a different cost can be applied to different wrong predictions. For example in terms of safety risk labeling a wet road as snow/ice results in no risk, but labeling a wet road as dry can result in only a slightly increased risk. In order to show the effect of this method, some extreme costs have been set. These can be seen in the equation 5.20, where the row of the matrix specifies the predicted label and the column the true label. Predicting dry or wet instead of standing water or snow/ice now has an increased cost of 100, while prediction errors the other way round are not penalized.

$$u(i,j) = \begin{pmatrix} 1 & 2 & 100 & 100 \\ 1 & 1 & 100 & 100 \\ 1 & 1 & 1 & 1 \\ 1 & 1 & 1 & 1 \end{pmatrix} \tag{5.20}$$

The results of this additional cost factor are shown in table 5.18. Now five cases of standing water are labeled correctly. Almost all snow/ice cases are now classified correctly. The disadvantage of the cost factors is that the accuracy of the new prediction model dropped. Now only 75 % of the test data are predicted correctly.

Table 5.18: Confusion matrix using artificial neural network for 4 classes with vehicle data using different mis-classification costs

		Prediction			
		Dry	Wet	Standing Water	Snow/ice
Labeled	Dry	709	70	0	145
	Wet	94	491	93	46
	Standing Water	0	4	5	0
	Snow/ice	2	1	3	167

5.4 Comparison of Classification Results

In the previous section, the focus of the result discussion focused on the amount of correctly predicted cases. Especially the last two variants show, that only looking at the accuracy is not sufficient to decide if a method is suited for the friction potential estimation problem. The prediction models can be tuned conservative in order not to miss too many safety critical cases. A too conservative model will predict many uncritical cases as potentially risky, which can reduce the performance of the autonomous vehicle.

In terms of the three classes, there is a clear ordering of the classes from safe to risky. This ordering is dry, wet and finally snow/ice. This allows to introduce two more measures. A false positive warning is defined as selecting a riskier class than needed and a false negative shall be defined as choosing a too safe class. This means the false positives are all entries in the upper triangle of the prediction matrix and all false negatives are in the lower triangle. The ratios of false negative and false positive and accuracy for all methods can be found in table 5.19. The sum of all correctly classified road conditions and false positives defines the cases, where the classification would allow safe driving. Thus, the column is called safe prediction. The safest model, which is also the most accurate, is the ANN.

Adding vehicle data to this model not only decreases the accuracy but also the safety. On a similar level as the ANN is the road weather forecast with the modification that all forecasted negative surface temperatures are relabeled to snow/ice. Compared to the unmodified forecast, this modification only adds 1 % more false positives but decreases the safety risk by 3.5 %. Of all models, the forecast, even in its unmodified form, has the most false positives, which shows that the product is already tuned to the conservative/safe side.

In case of four classes, the ordering is not as straight forward because aquaplaning and snow/ice can have similar friction potentials. It was decided to sort standing water

Table 5.19: Classification result comparison for 3 classes in %

Method	Accuracy	False positive	False negative	safe prediction
Next RWIS	78.99	8.47	12.54	87.46
RWF	74.66	14.29	11.05	88.95
RWF (modified)	77.11	15.32	7.57	92.43
FAT Method	81.52	7	11.48	88.52
MLR	83.76	7.87	8.37	91.63
MLR with vehicle data	84.8	5.52	9.68	90.32
ANN	87.15	5.58	7.27	92.73
ANN with vehicle data	86.77	3.77	7.27	90.54

less severe than snow/ice because for aquaplaning effects to appear, a certain velocity has to be surpassed, while snow/ice always exhibits low friction potential values. The results of this ordering are summarised in table 5.20.

Table 5.20: Classification result comparison for 4 classes in %

Method	Accuracy	False positive	False negative	safe prediction
FAT Method	81.14	7	11.86	88.14
MLR	83.2	7.76	9.02	90.96
MLR with vehicle data	84.42	5.47	9.9	89.89
ANN	86.5	6.51	7	93.1
ANN with vehicle data	86.22	5.14	8.64	91.36
ANN with class weights	85.51	7.93	6.56	93.44
ANN with classification costs	75.01	19.35	5.69	94.36

The results of the ANN variants show that penalizing critical mis-classifications can increase the amount of safely predicted classes and thus increases the overall safety of the system. The ANN with the extreme costs for wrong labeling of standing water and ice predicts 94.36 % of the test cases safely at the cost of predicting 19.35 % of the data too conservative and thus potentially limits the system performance in these cases.

6 Remaining Risk of Overestimating the Friction Potential

In this chapter, the results of the previous chapters are combined to provide a coarse estimation of the remaining risk of exceeding the friction potential. The missing ingredient of this estimation is the required friction during normal driving situations. Therefore, in the first section two different naturalistic driving studies are compared. The available friction potential data found in [9] and chapter 3 is used to estimate the frequency of exceeding the friction potential. In the last section, both the data of the naturalistic driving studies and continuous wet friction potential measurements shown in chapter 4 are applied to calculate the remaining risk, if an intermediate layer classification and the continuous wet grip map is used in the AV.

6.1 Friction Requirements for Normal Driving

Several naturalistic driving studies with human drivers have been conducted in the past. Although the AV might drive differently from human drivers, the cars will share the roads with other human drivers and therefore need to react to their driving behaviour, resulting in similar acceleration, and thus friction potential utilisation.

Data from two studies is compared: The 100-car naturalistic driving study conducted in the USA [157] and data recorded by 15 vehicles during the EU project EuroFOT [158]. While only results of the first study are available, access to the raw data of the latter allows a more detailed analysis.

The data of the 100-car naturalistic driving study was used to determine indicators for safe and risky driving behaviour [157]. In this analysis, the drivers of the study were grouped into three categories depending on their level of involvement in near-crash and crash scenarios. For each of these three groups, Klauer et al. analysed the accelerations during normal driving. 88.8 % of this baseline data was recorded during clear conditions, 10.9 % during rain and only 0.3 % during snow conditions. Thus, it can be assumed that the data is dominated by driving in high friction potential condi-

tions. The baseline data, which consists of random 6 s samples of all drives recorded in the study, was used to evaluate the peak accelerations, decelerations and lateral accelerations. Only accelerations larger than 0.3 g have been evaluated because all lower accelerations were attributed to normal driving. The results were then used to calculate the number of expected events per million vehicle miles traveled. The analysis shows that unsafe drivers experience accelerations above 0.3 g more often than safe drivers. This is especially visible in the braking frequency. The differentiation between the driver groups is not important for the discussion. Instead, figure 6.1 shows the lateral acceleration and deceleration events averaged over all three groups. The data shows an exponential decrease in the frequency with which large accelerations are experienced by the human driver. The data indicates that lateral accelerations in the range up to 0.4 g are more frequent than decelerations but the frequency of even larger lateral accelerations decreases faster than the frequency of decelerations. Comparing this data to friction potential ranges found in [9] and plotted in figure 1.3, which were lower than the ones encountered in the measurements presented in this thesis, it can be seen that only in rare instances friction values close to these friction potentials are required. For example, the lower quartile of the wet friction potential on asphalt based on the data published in [9] starts at a value of about 0.6. In combination, about 1550 lateral acceleration events or deceleration events per 1 million km would require a friction potential equal or above this value. This would be on average one event every 645 km driving on a worse than average asphalt road. Assuming a value of 0.7, which is around the lower quartile of all wet friction potential measurements with SR 1 presented in this thesis and about the median of all wet friction potential measurements shown in [9], only once every 2030 km driving on a worse than average wet asphalt road, a larger friction potential than available would be required. The median wet friction potential found via SWB test with SR 1 is 0.78. A lateral or longitudinal acceleration above the nearest bin limit 0.8 is required 154 times per 1 million km traveled. Thus, driving on an average wet road, the available friction potential is exceeded only once every 6490 km. Since the distribution between wet roads and dry roads in Germany is heavily biased towards dry, an average driver will not experience this situation every year. This evaluation also shows, why ABS interventions are very uncommon.

In [159], the accelerations of 15 vehicles, which took part in the EuroFOT study [158], were evaluated. In this data set, more than 99 % of the measured combined accelerations are below 4.5 $\mathrm{m\,s^{-2}}$. The distribution of the accelerations between 40 kph and 100 kph based on this publication can be seen in figure 6.2. It can be seen that accelerations larger than 0.6 g only make up less than 0.001 % of the measured values.

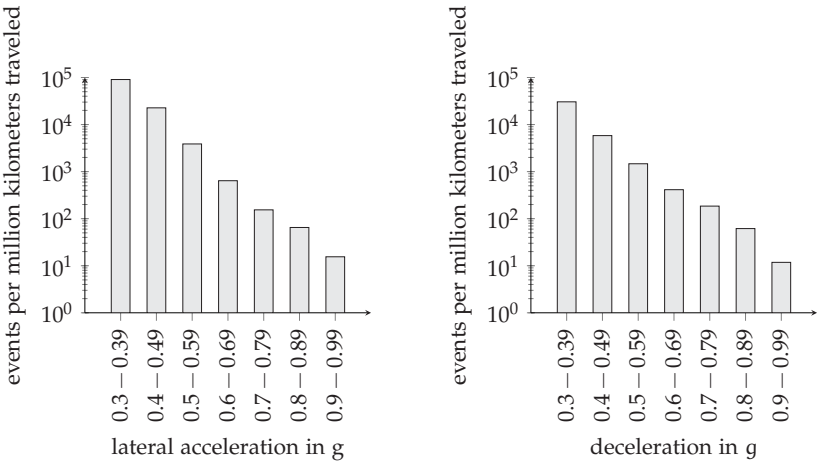

Figure 6.1: Lateral acceleration events (left) and deceleration events (right) per million vehicle kilometers traveled based on the 100-car naturalistic driving study presented in [157]

The results of the EuroFOT evaluation cannot directly be compared with the 100-car study. There are two main reasons for this. First of all, it is unknown, what amount of driving has been conducted on surfaces with a high friction potential. In order to exclude snow or ice from the evaluation, only data with a measured ambient temperature above 5 °C has been used in the new analysis. Second, the original evaluation focused on the frequency of measurement values but consecutive measurement values are not independent of each other. For example, a full braking event starting at 100 kph would result in more large acceleration entries than one starting at 30 kph, despite both only being one event. Therefore, similar to the 100-car study evaluation, the drives have been split into 6 s long parts and the maximum acceleration in these intervals has been used as one event. In order to exclude measurement noise, the raw data has been filtered with a low pass filter with a stopband at 2 Hz.

In addition, the data has been limited to a maximum velocity of 100 kph, since the EuroFOT data was otherwise dominated by highway driving. Applying the temperature and velocity filter to the data, a driven distance of almost 204 000 km remains as data basis. Using this total driven distance in combination with the number of events in each bin, a comparison with the 100-car study is possible. The results for deceleration and lateral acceleration can be seen on the left side of figure 6.3. Deceleration in the bin above 0.3 g appear 7.9 times more often and lateral accelerations in the same

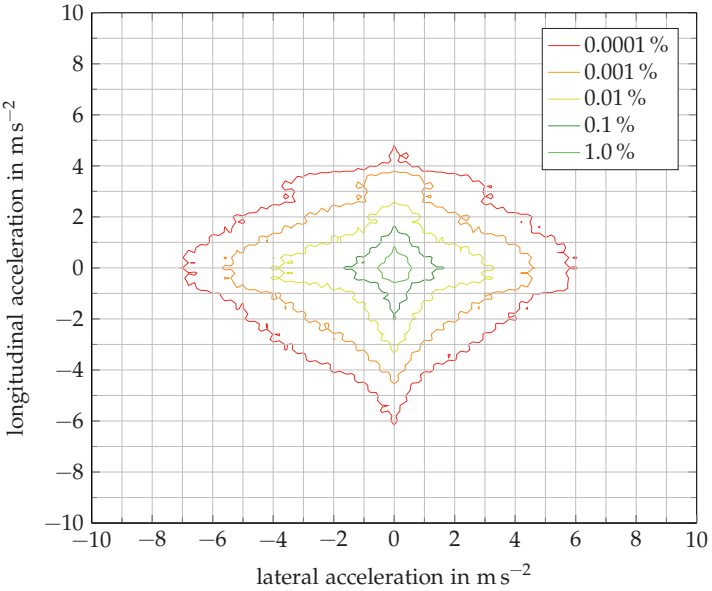

Figure 6.2: Distribution of longitudinal and lateral accelerations of EuroFOT data based on [159]

bin 5.5 times more often than in the 100-car study. This trend is observable for all bins. Nevertheless, the data shows that larger accelerations appear rarely. Compared with the 100-car study, an acceleration value above 0.7 g would be required for deceleration or lateral acceleration 3250 (compared to 1550) times per million kilometers or once every 307 km. A possible explanation for the more frequent larger accelerations present in the EuroFOT data could be different driving customs in Germany. Also traffic density or the performance of the vehicles could influence the measurements.

Instead of evaluating the lateral and longitudinal acceleration separately, the combined lateral and longitudinal acceleration determines the required friction potential. An evaluation of this combined acceleration can be seen on the right hand side of figure 6.3. As already seen in figure 6.2, combined lateral and longitudinal accelerations are quite common. Thus, large combined acceleration events are more frequent than lateral or longitudinal events evaluated separately. For example a combined acceleration above 0.7 g would be required 3725 times per million km traveled.

The evaluation confirms the relative low acceleration levels recorded in the EuroFOT

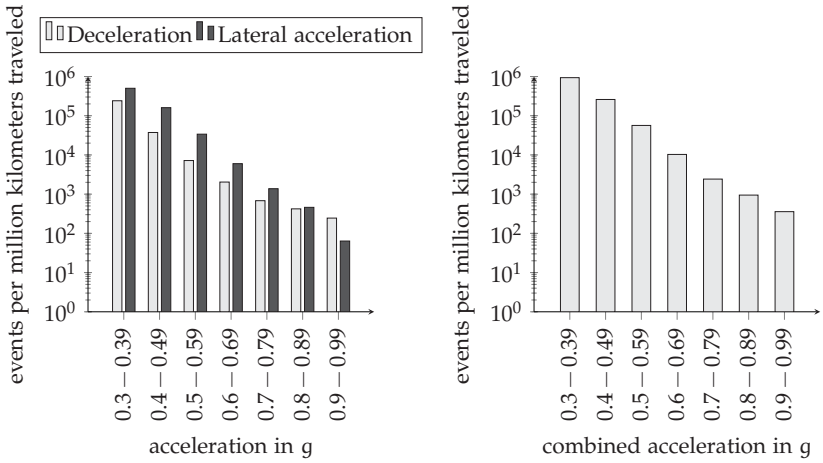

Figure 6.3: Deceleration and lateral acceleration events (left) and combined acceleration events (right) per million vehicle kilometers traveled based on the EuroFOT data

study. Less than 2.5 % of the used accelerations are above 0.3 g and only 0.4 % are above 0.4 g. This means less than a fifth of all accelerations above 0.3 g are also above 0.4 g, which are comparable observations to those made in the previously mentioned 100-car study. Comparing both driving studies with the available friction potential in literature and measured during the SWB tests described in section 3.3 it can be concluded that human drivers only rarely experience driving situations close to the friction potential on wet or dry roads. In case of snow and ice on the road, the available friction potential falls below the normally used friction. Thus, in these situations, an adaption of driving style is required and also driving situations close to or at the available friction potential are common.

6.2 Risk Estimation

Since not all road conditions are equally frequent and because the risk of missing an intermediate layer is different, at last, a very coarse estimation of an accident risk shall be conducted. This requires several assumptions and the resulting numbers are only valid for the tested track and vehicle, although the same calculation process can be applied to different data sets if available.

The first set of assumptions are:

1. On a dry intermediate layer, there is never insufficent friction potential.

2. On a correctly classified intermediate layer, there is never a friction potential related accident risk.

Assumption 1 requires that a sufficiently conservative dry friction potential value is used for planning. The single wheel braking tests conducted on the public road track shown in figure 3.17 show that the smallest measured dry friction potential values are around 0.95. Including the safety margin for errors between SWB and the full braking performance, a value of 0.85 should be available for the trajectory planning on dry surfaces.

Assumption 2 requires that if the classification category is correct, the friction potential estimation is also sufficiently conservative and that the trajectory planning can prevent the need for higher friction values than this conservative estimate.

The next assumption concerns the intermediate layer. It has been assumed that over a period of one year, the measured intermediate layer at the RWIS is representative for the whole track. The influence of winter road maintenance has again been corrected by setting the intermediate layer of every measurement with negative road surface temperature and a wet intermediate layer to snow/ice. The distribution was calculated from stored data of the RWIS Q441 in the period from 01.09.2016 to 31.08.2017. Unfortunately, not all data was available. Four measurements were lost due to problems during the download process. A larger part (4354 of the 35 040 data points) is not available because the RWIS did not send valid data. The intermediate layer distribution was calculated ignoring these missing data points. This results in a distribution of 68.3 % dry, 23.9 % wet and 7.8 % snow/ice.

If the intermediate layer is estimated better than it is in reality according to the previously defined sorting, a risk of exceeding the available friction potential exists. The distribution of the required friction potential during planning is derived from the EuroFOT study first discussed in section 6.1. Instead of the short 6 s intervals, the maximum combined acceleration in longer 5 min intervals has been used to derive the maximum required friction potential during one hour of driving. The longer interval was chosen because testing different interval lengths showed that the 6 s segments were not long enough to result in independent samples. The longer interval length reduced the effect of this short-coming.

The hourly distribution is calculated by drawing 12 random samples from the 5 min distribution. The distribution of the maximal required friction potential can be seen in figure 6.4. A finer resolution of the bins of $\Delta\mu = 0.025$ was chosen.

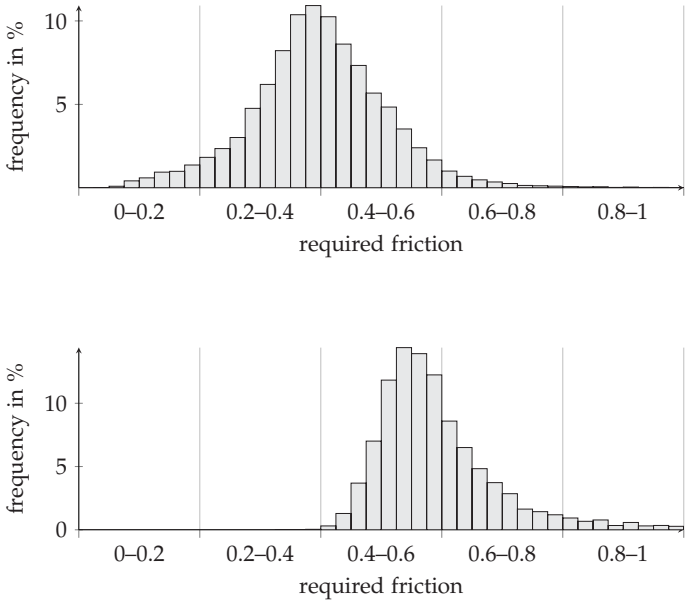

Figure 6.4: Required friction potential distribution based on the maximum combined acceleration in 5 min; top: 5 min distribution; bottom: calculated 1 h distribution based on 5 min distribution

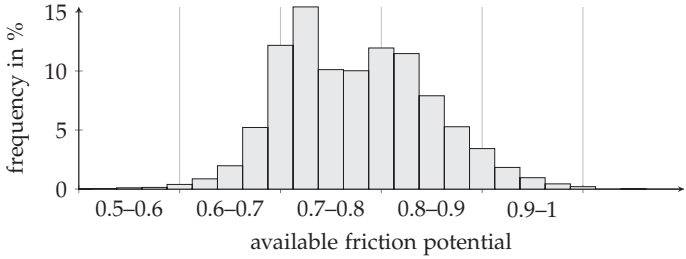

Figure 6.5: Available friction potential distribution calculated from RoadSTAR measurements with the PIARC tyre

The distribution of the available wet friction potential is derived from the measured friction potential on the public road track measured with the RoadSTAR truck and the PIARC tyre. The friction potential values are first velocity corrected and finally scaled to the estimated friction potential of the vehicle using equation 4.5. Although this distribution describes the friction potential variation over the tested track, it is assumed that the friction potential distribution over time would be similar. The distribution of the available friction potential on a wet road can be seen in figure 6.5.

An alternative not followed would be to weight the friction potential proportional to the allowed velocity on the road segment. Another assumption used is, that the friction potential of segments, where the RoadSTAR truck was unable to measure a valid friction potential, do not distort the distribution.

Using both the distribution of the required friction potential during planning and the available wet friction potential, the risk of exceeding the available friction, whenever a wet track is estimated as dry can be calculated by equation 6.1.

$$Pwet(\mu_{planned} \geqslant \mu_{pot}) = \sum_{i=0}^{N} P(\mu_{pot} \in \mu_i) \left[\sum_{j=i}^{N} P(\mu_{planned} \in \mu_j) \right] \tag{6.1}$$

$P(\mu \in \mu_i)$ describes the probability that the friction is inside the i-th bin of either the distribution of the available friction potential or the planned friction. Inserting the distributions shown in figure 6.5 and 6.4, the risk results in 7.2 % that the required friction is larger than the available friction potential. In order to apply the condition stated for the friction values, that the friction potential for planning on dry roads should not exceed $\mu = 0.85$, the distribution of the required friction can be adapted that this condition is fulfilled. Therefore, all entries in the bins requiring more than 0.85 are shifted to the bin $[0.825, 0.85)$. This reduces the risk further down to 5.5 % per hour driving on wet roads.

The risk of exceeding the required friction potential on a snow or ice covered road, that is mistakenly classified as wet or dry, has been assumed as 100 %. The available friction potential on these surfaces is usually lower than the maximal friction ($\mu_{pot} < 0.4$) required for normal driving seen in figure 6.4.

Altogether, the risk of exceeding the friction potential can now be calculated by

$$\begin{aligned} P(\mu_{planned} \geqslant \mu_{pot}) =& P(\text{IML} = \text{ICE}) \cdot P(\text{EIML} \neq \text{ICE}|\ \text{IML} = \text{ICE}) \cdot 1 \\ &+ P(\text{IML} = \text{WET}) \cdot P(\text{EIML} = \text{DRY}|\ \text{IML} = \text{WET}) \cdot 0.055 \\ =& 0.078 \cdot 0.1628 \cdot 1 + 0.239 \cdot 0.198 \cdot 0.055 \\ =& 0.0153. \end{aligned} \tag{6.2}$$

In this equation, EIML is the estimated intermediate layer and $P(\text{EIML} = x)$ has been calculated using the results presented in table 5.14 and IML is the real intermediate layer. $P(\text{EIML} = \text{DRY}|\ \text{IML} = \text{WET})$ is calculated $145/(145 + 583 + 5) = 0.198$. The majority of the remaining risk of 1.53 % is due to missing the intermediate layer snow / ice. In reality, this probability is significantly lower because of the winter maintenance. This highlights the importance to include information about winter maintenance in an estimation model.

The same methodology could be applied to the four classes. Additional assumptions concerning the probability of high water heights and a velocity distribution are required. Since both distributions are not available, an analysis of the remaining risk of the four classes estimators has not been conducted.

7 Conclusions

The guarantee of a lower friction potential bound is a requirement for safe route planning and espcially for safe trajectory planning. A very conservative estimation of this bound conflicts with the aim to drive comparable to human drivers and not impede other traffic participants. The AV has to adapt the velocity according to the changing friction potential. In order to conduct this velocity change in a comfortable manner, a large preview distance, which is dependent on the friction potential change and the driving velocity, is required. This preview distance cannot be covered by on-board sensors and thus requires the inclusion of external data sources leading to the preference of a cause-based friction potential estimation method. If the objective is using this method type, the relevant factors influencing the friction potential have to be known and included. A mapping from the change of an included influencing factor to the change in available friction potential has to be available.

A review of the established norms and publications showed that no common definition of the friction potential is available, but the used definitions always depend on the application. Often only the relative sorting of the friction potential is used. For example, this is done while determining the EU wet friction label but also road maintenance, where the limit and warning values are derived from a reference measurement campaign. The friction potential definition most suited for the trajectory planning task is defined by the average possible deceleration to standstill. The straight-forward and usually used approach to measure this friction potential is to conduct full-braking tests. Since these tests cannot be conducted on public roads, in this thesis a new measurement method has been developed, which fully brakes only one wheel for a short period of time (SWB). A comparison of this method with full-braking measurements on a proving ground showed that this method can reproduce the friction potential values of the full-braking tests, but due to the short evaluation interval, it cannot predict the full-braking friction potential, if the available friction potential changes along the travelled distance of the full-braking tests. On the proving ground, this was the case due to suspected partial aquaplaning resulting in errors of the measured friction potential of about 0.1.

The SWB method was used on a track along public roads to determine the relev-

ant influencing factors on the friction potential. A clear dependence of the measured friction potential on the used tyre, intermediate layer and road surface was found. Indications of an additional influence of the surface temperature on the measured friction potential have been found. This influence varied between different measurement points and is smaller than the previously mentioned factors. A surprising result are different friction potential values between two tyre sets of the same tyre type, which can only be explained by the tyre wear. No friction potential dependence on the velocity was found. Also no seasonal effects or road polishing effects were visible during the measurement period.

Therefore, it was decided to include the influencing factors road surface and intermediate layer in the cause-based friction potential estimation method and fix the tyre set used on the AV. Existing rubber friction theories allow to approximate the available friction potential based on the rubber properties and the road texture but require the specification of several free parameters. In case of Persson's theory presented, these are the cut-off frequency and the background temperature. In publications applying this theory, often a fixed slip-velocity and pressure are used, while the basic brush tyre model already shows that this assumption is invalid. Another problem of these theories is that it is difficult to measure the road surface texture in a sufficient resolution over longer distances. Instead of these theories, it was decided to apply established road friction measurement methods used in road maintenance. According to the conducted SWB measurements, the friction potential on dry roads is always sufficient, thus measuring the wet friction potential is sufficient. The German SKM and the Austrian RoadSTAR method have been evaluated with the RoadSTAR method resulting in more promising results. A modification of the RoadSTAR truck in order to use similar measurement conditions as in the test vehicle used for SWB failed due to limitations in the RoadSTAR measurement truck. Nevertheless, a correlation between the default RoadSTAR measurement results and the SWB measurements was found. Even though no velocity dependence of the SWB measurements was found, a velocity correction of the RoadSTAR measurements improves the correlation. An explanation of this required velocity correction is, that RoadSTAR measures at a fixed slip value, while the ABS of the vehicle controls the slip around the optimum value, which can change with the velocity.

Several classification methods using road weather station, radar and vehicle measurements as well as a road weather forecast have been used to determine the correct intermediate layer. In many cases, a good differentiation between the intermediate layers dry, wet and snow/ice was possible. A further destinction between a critical water height for aquaplaning named standing water and wet was difficult. A possible

reason is a wrong measured water height and/or that no input considering the water drainage is included in the methods. Several approaches to tune the estimation methods more conservative have been highlighted. The road weather forecast showed that the surface temperature can be modelled accurately but the intermediate layer proves difficult.

Finally, an approach to estimate the risk of exceeding the available friction potential has been shown. On the public road track, the risk on the wet surface is very low but on snow the risk is over 1 % per hour. In reality, this risk is lower because no winter maintenance has been included in the calculation.

In order to further develop a cause-based friction potential estimation method using the components developed in this thesis, a larger data basis using more measurement points should be achieved. Especially brake points with low friction potential are currently missing in the statistics. A better correlation between the measured wet grip friction potential using a measurement truck and the test vehicle should be pursued. The longitudinal slip measurement method of the RoadSTAR truck proved functioning.

Further improvements should focus on a more accurate measurement of the wheel load and on increasing the measurement ranges of the sensors. In addition, using more representative tyre operating conditions, increased wheel load, larger damping and smaller slip-values could further improve the correlation. The correct classification of the intermediate layer showed three areas, which require further improvement. The sensors measuring the ground truth need a better accuracy not only measuring the intermediate layer but also the water height. The detection of potential aquaplaning situations is currently not possible. Besides the improved ground truth measurements, the inclusion of road geometry in the classification methods could be tested. Finally, information about the winter maintenance should be included in the classification as this has a major impact on the distribution of the intermediate layer.

Appendix

A Vehicle Model

A very simple two track model has been used to simulate the trajectory during a single wheel braking test. The coordinate systems are defined according to ISO 8855 [160]. The model uses six states. The three states v_x, v_y and r describe the vehicle motion in the vehicle fixed coordinate system with v_x describing the forward motion of the vehicle, v_y the lateral motion and r the yaw rate. The state in the global coordinate system is calculated using the states X, Y and Ω. X desribes the position along the X-axis, Y along the Y-axis and Ω the heading. Using these six states, the vehicle motion can be calculated by the nonlinear ordinary differential equation system described by equation A.1.

$$\begin{aligned}
\dot{X} &= \cos(\Omega)v_x - \sin(\Omega)v_y \\
\dot{Y} &= \sin(\Omega)v_y + \cos(\Omega)v_x \\
\dot{\Omega} &= r \\
\dot{v_x} &= \frac{F_x}{m} + v_y r \\
\dot{v_y} &= \frac{F_y}{m} - v_x r \\
\dot{r} &= \frac{M_z}{I_{zz}}
\end{aligned} \tag{A.1}$$

The calculation of the forces F_x, F_y and moment M_z require the tyre forces at each wheel. Therefore, the lateral forces are calculated using a magic formula tyre model. This model requires the parameters κ, α and F_z at each tyre. For the three tyres rear-left, rear-right and front-left only lateral forces are considered. Therefore, $\kappa = 0$. In order

to calculate α, the velocities have to be transformed into the wheel coordinate system. The equations for the velocities at the tyre contact patches in the vehicle coordinate system are:

$$\begin{aligned} v_{x,rr} &= v_x + \frac{t_r}{2} r \\ v_{y,rr} &= v_y - l_r r \end{aligned} \tag{A.2}$$

$$\begin{aligned} v_{x,rl} &= v_x - \frac{t_r}{2} r \\ v_{y,rl} &= v_y - l_r r \end{aligned} \tag{A.3}$$

$$\begin{aligned} v_{x,fr} &= v_x - \frac{t_f}{2} r \\ v_{y,fr} &= v_y + l_f r \end{aligned} \tag{A.4}$$

$$\begin{aligned} v_{x,fl} &= v_x + \frac{t_f}{2} r \\ v_{y,fl} &= v_y + l_f r \end{aligned} \tag{A.5}$$

For the rear tyres, the vehicle coordinate system equals the wheel coordinate system. For the front tyres, the velocities have to be converted to the coordinate system rotated by the steering angle δ_W.

$$\begin{aligned} v_{x,fr_w} &= \cos(\delta_W) v_x + \sin(\delta_W) v_y \\ v_{y,fr_w} &= -\sin(\delta_W) v_x + \cos(\delta_W) v_y \end{aligned} \tag{A.6}$$

The slip angle α can now be calculated by

$$\alpha = \tan^{-1}\left(\frac{v_y}{v_x}\right). \tag{A.7}$$

The wheel loads are calculated by equations A.8. The factor k_s accounts for the roll-stiffness distribution between both axles.

$$\begin{aligned} F_{z,rr} &= \frac{1}{2} m g \frac{l_f}{l_{wb}} + m a_x \frac{h_{cog}}{l_{wb}} - (1 - k_s) m a_y \frac{h_{cog}}{\frac{t_f + t_r}{2}} \\ F_{z,rl} &= \frac{1}{2} m g \frac{l_f}{l_{wb}} + m a_x \frac{h_{cog}}{l_{wb}} + (1 - k_s) m a_y \frac{h_{cog}}{\frac{t_f + t_r}{2}} \\ F_{z,fr} &= \frac{1}{2} m g \frac{l_r}{l_{wb}} - m a_x \frac{h_{cog}}{l_{wb}} - k_s m a_y \frac{h_{cog}}{\frac{t_f + t_r}{2}} \\ F_{z,fl} &= \frac{1}{2} m g \frac{l_r}{l_{wb}} - m a_x \frac{h_{cog}}{l_{wb}} + k_s m a_y \frac{h_{cog}}{\frac{t_f + t_r}{2}} \end{aligned} \tag{A.8}$$

The accelerations are calculated according to equations A.9.

$$\begin{aligned} a_x &= \dot{v_x} - v_y r \\ a_y &= \dot{v_y} + v_x r \end{aligned} \tag{A.9}$$

The resulting α and F_z values are inserted in a magic formula tyre model to calculate the lateral forces of the tyres front-left, rear-right and rear-left. It was assumed that the front-right tyre does not transfer any lateral forces. For the front-right tyre no tyre model was used. It was assumed that this force acts in the opposite direction of the velocity vector at this tyre. The magnitude of the force is calculated by

$$F_{h,fr} = max(\frac{M_{brk}}{r_e}, \mu_{pot} F_{z,fr}) \tag{A.10}$$

whenever a brake torque is applied, otherwise it is 0.

Transforming the forces from the tyre coordinate system back into the vehicle coordinate system, the values F_x, F_y and M_z required in equation A.1 can be calculated according to equation A.11.¸

$$\begin{aligned} F_x &= F_{x,fl}cos(\delta_W) - F_{y,fl}sin(\delta_W) + F_{x,fr}cos(\delta_W) - F_{y,fr}sin(\delta_W) \\ F_y &= F_{y,fl}cos(\delta_W) + F_{x,fl}sin(\delta_W) + F_{y,fr}cos(\delta_W) + F_{x,fr}sin(\delta_W) + F_{y,rl} + F_{y,rr} \\ M_z &= -\frac{t_f}{2}(F_{x,fl}cos(\delta_W) - F_{y,fl}sin(\delta_W) + \frac{t_f}{2}(F_{x,fr}cos(\delta_W) - F_{y,fr}sin(\delta_W)) \\ &\quad + l_f(F_{y,fl}cos(\delta_W) + F_{x,fl}sin(\delta_W) + F_{y,fr}cos(\delta_W) + F_{x,fr}sin(\delta_W)) \\ &\quad - l_r(F_{y,rl} + F_{y,rr}) \end{aligned} \tag{A.11}$$

B Vehicle Measurements

In this section, the data to validate the SWB measurements on the test track discussed in section 3.2 are plotted. All measurements were conducted with the first summer tyre set. The measurements on dry cobblestone have been conducted on an earlier day than the other measurements due to the weather conditions. On the second date, the cobblestone surface did not dry. Figure B.1 shows the measured tyre curves and fitted tyre models. Figure B.2 displays the measured accelerations during the full braking measurements on the seven different surface and intermediate layer combinations.

B.1 Friction Measurements on FAT track

Figure B.3 shows a comparison between SWB measurements conducted on the brake points used in the FAT project [9] and the results of this project. All measurements were conducted in wet conditions. The SWB tests have been measured using the first summer tyre set. It can be seen, that the friction potential values of the SWB measurements are always higher than the results reported in FAT but the trend in the measured friction potential is the same. It is also visible, that several of the braking points specified in the FAT project have a lower wet friction potential than the brake points used in this thesis shown in figure 3.17.

B.2 Hydroplaning Example

Figure B.4 shows full braking measurements conducted on a proving ground. The test vehicle and summer tyres are different from the vehicle mainly used in this thesis. The water height on the proving ground was specified with 1 mm, no water height measurements to verify this value have been conducted. The measurements are recorded by a vbox 3i from Racelogic [161]. All full braking tests were started with a velocity of around 130 kph. The different decelerations measured with the new tyres compared to the worn tyre in the velocity range above about 70 kph can be explained by partial aquaplaning. Even for the new tyres, a partial aquaplaning effect is visible for

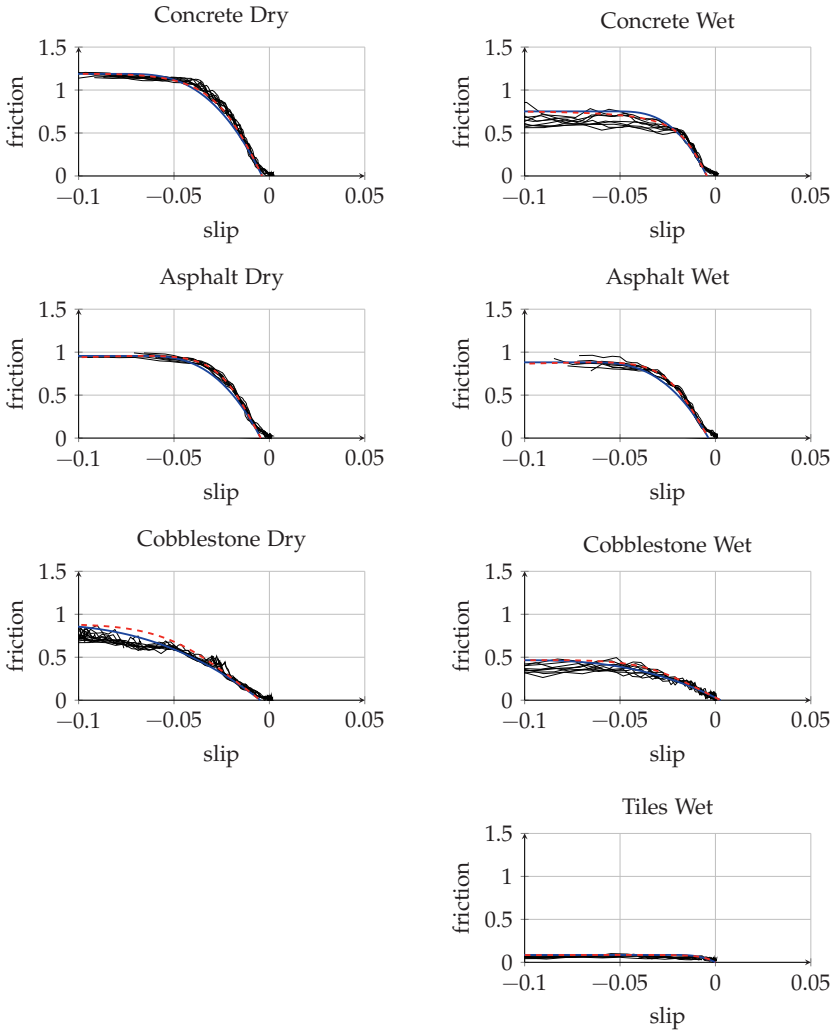

Figure B.1: Measured tyre curves during SWB tests on proving ground

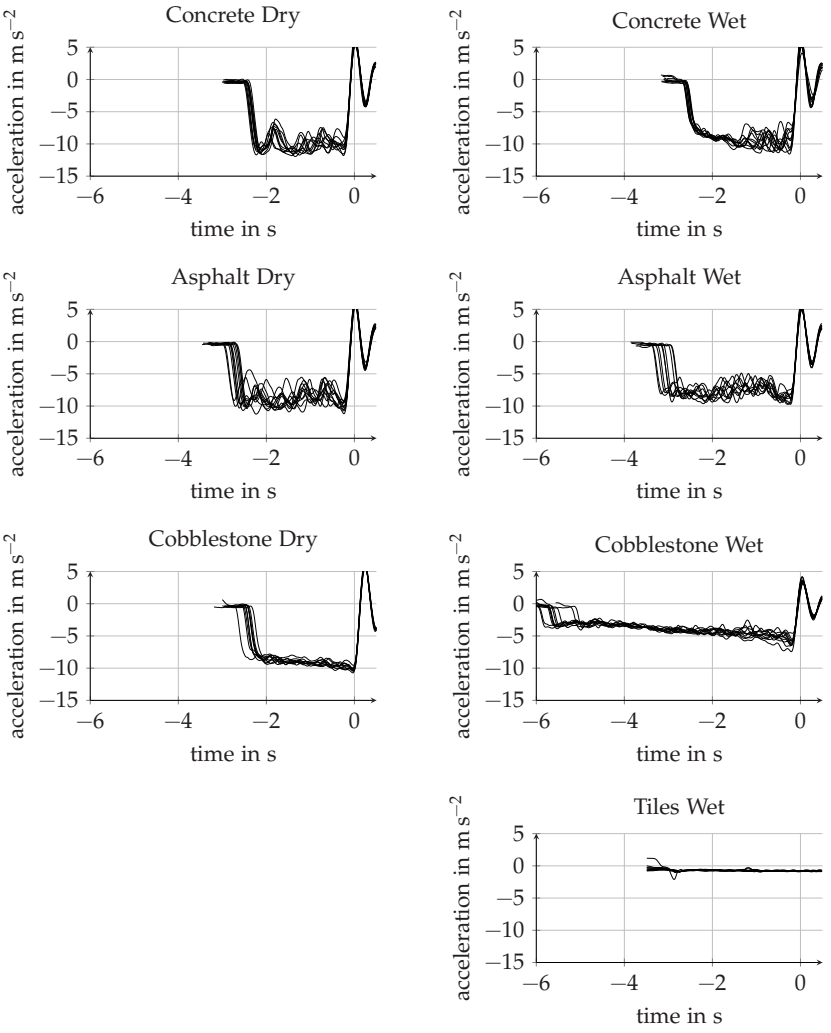

Figure B.2: Full braking measurements on proving ground

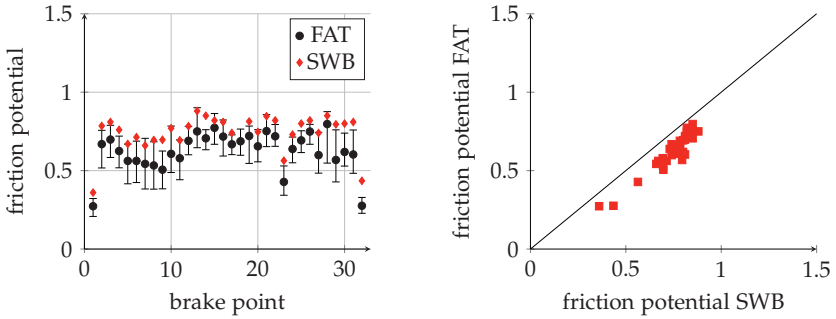

Figure B.3: Comparison between friction potential measurement results of the FAT project and SWB; FAT measurement: median of all wet measurements on each brake point; error bars between minimal and maximal wet measurement value on each brake point

velocities above 80 kph which results in a friction potential reduction at higher speeds.

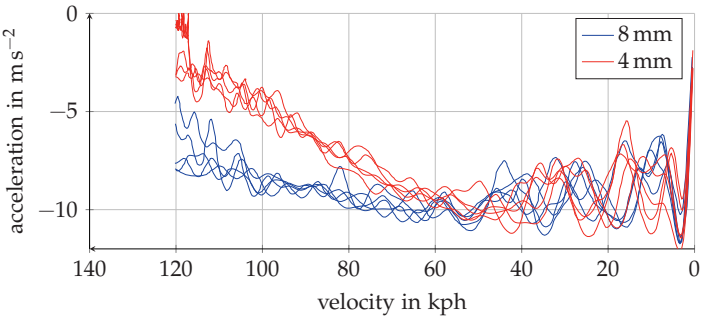

Figure B.4: Full braking tests with new (8 mm profile depth) and worn tyres (4 mm profile depth) on a wet test track with 1 mm water depth

B.3 Measurements on Snow/Ice

Measurements on snow and ice have been conduted during repeated drives along a route in Sweden over a period of two weeks. The friction potential values are calculated using full braking tests. The evaluation interval has been specified as the whole time period when ABS is active. The same test vehicle as used for the SWB tests has been

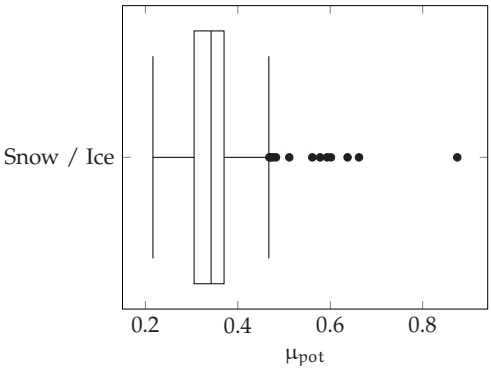

Figure B.5: Results of repeated full braking tests conducted on a snow covered track in Sweden over a period of two weeks

used, but different winter tyres were equipped. Whenever the majority of the MARWIS measurements showed the intermediate layer snow, ice or snow/ice the measurement has been included. No manual labeling was used. Altogether 203 valid measurement results are included in the boxplot shown in figure B.5.

C Continuous Friction Potential Measurements

The following figures show the data provided by the road maintenance measurement trucks SKM and RoadSTAR. Figure C.1 shows the data measured by the SKM truck on the public road course. All three laps are plotted. The different velocity categories are plotted in different colours.

Figures C.2, C.3 and C.4 show the results generated by the RoadSTAR truck on the two test track straights. For each tyre, the three measurement velocities and three repetitions are plotted.

Figures C.5, C.6, C.7 show the RoadSTAR measurement results on the public road track using the three different tyres.

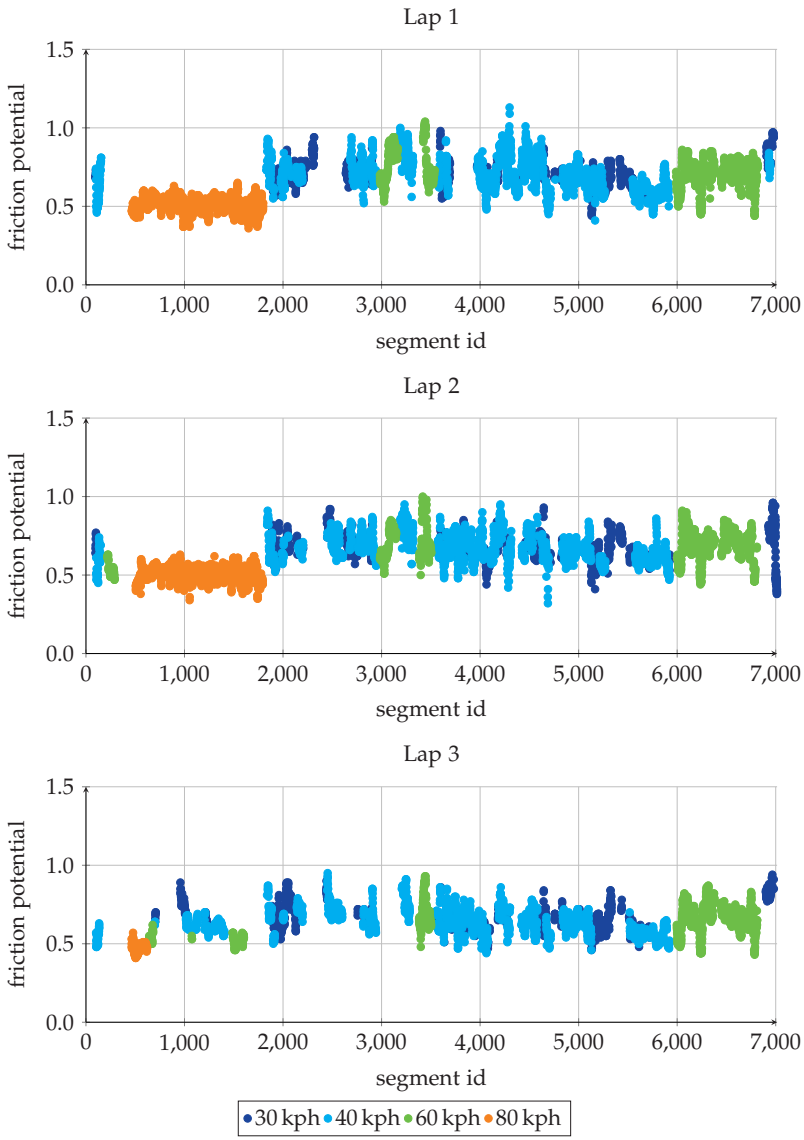

Figure C.1: SKM measurements on the public road track evaluated over 5 m segments

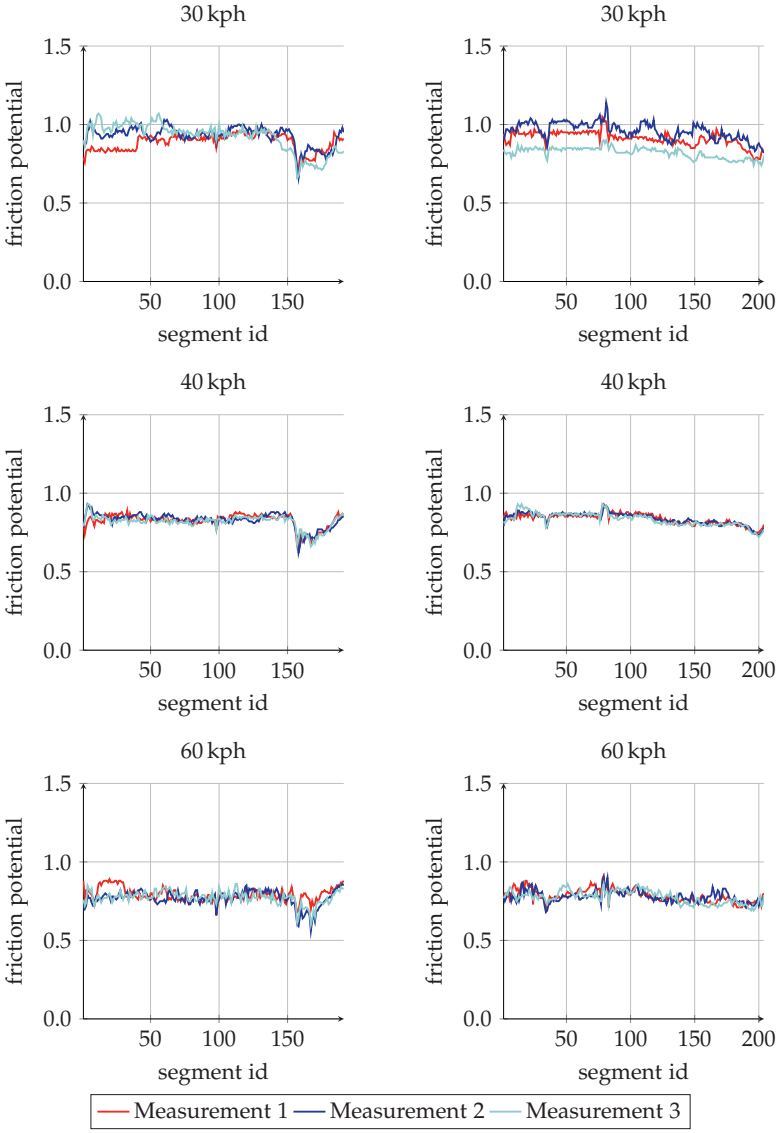

Figure C.2: RoadSTAR measurements with tyre A on test track; left column: straight 1; right column: straight 2

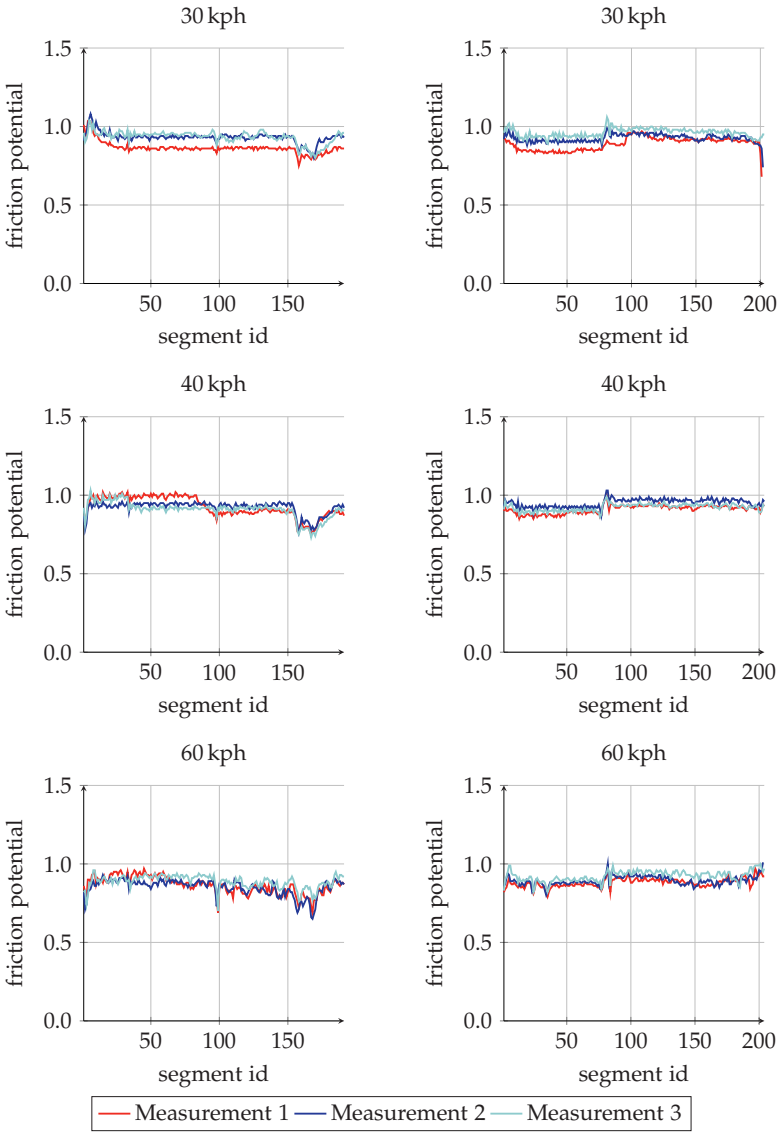

Figure C.3: RoadSTAR measurements with tyre B on test track; left column: straight 1; right column: straight 2

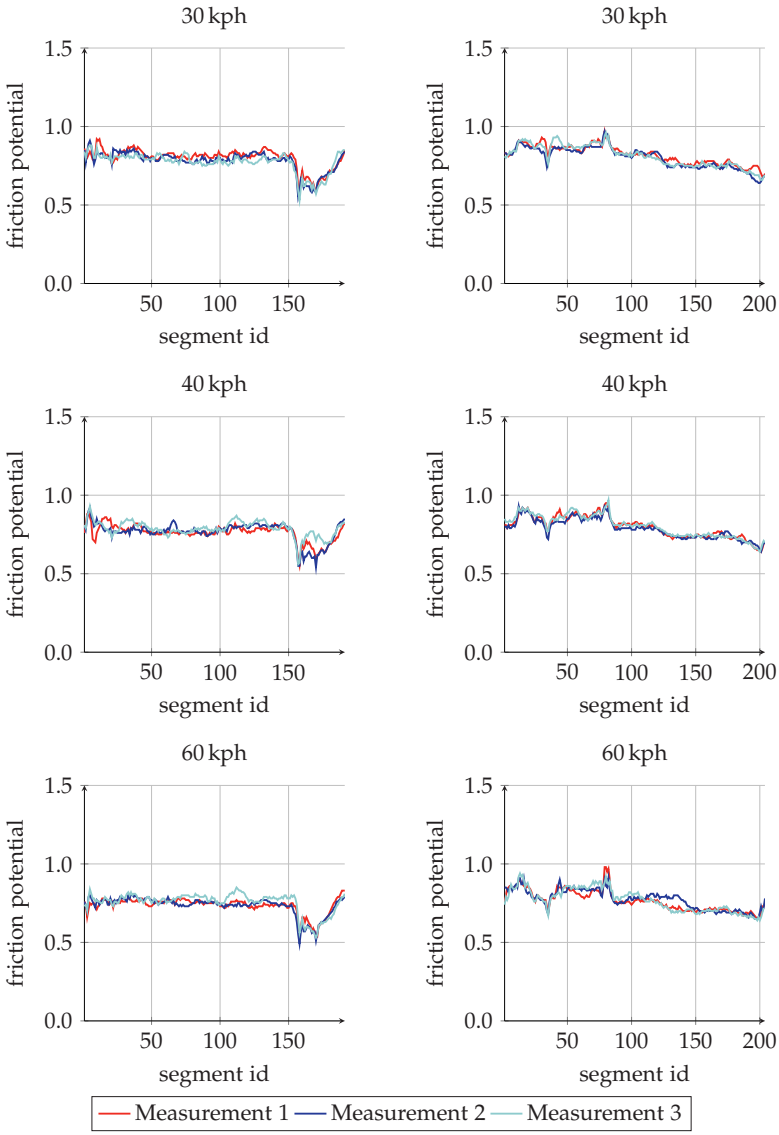

Figure C.4: RoadSTAR Measurements with PIARC tyre on test track; left column: straight 1; right column: straight 2

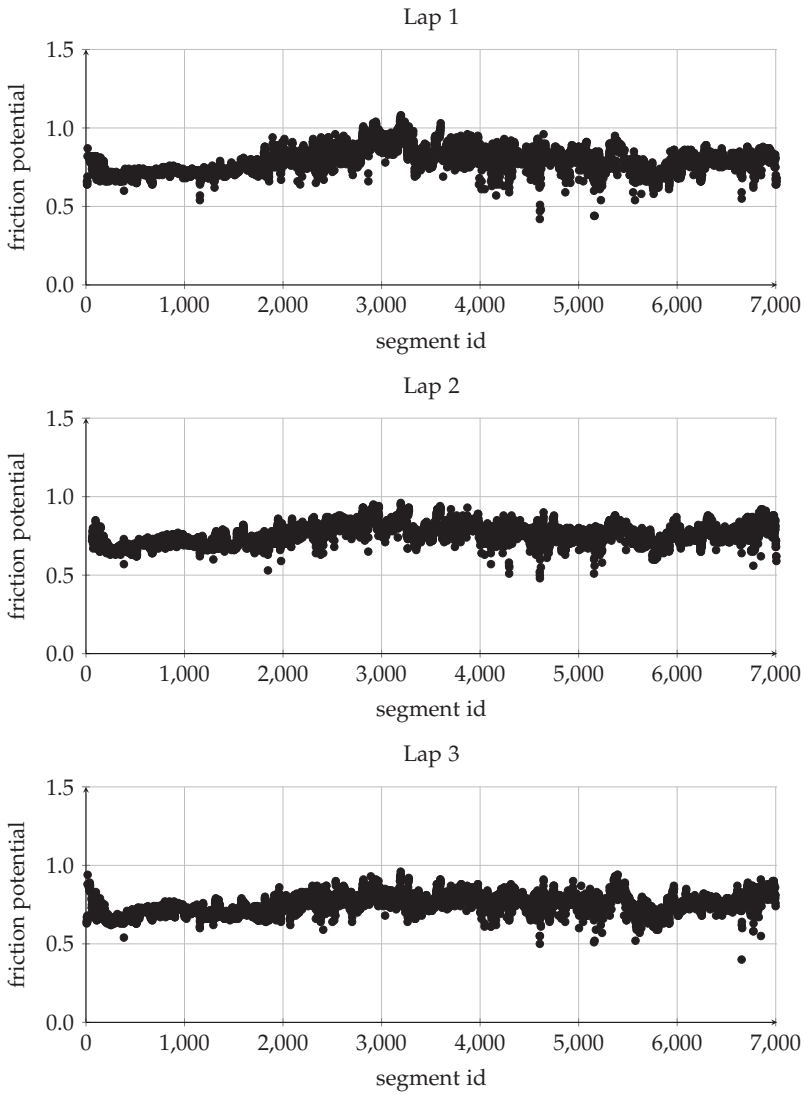

Figure C.5: RoadSTAR measurements on the public road track evaluated over 5 m segments without velocity correction using tyre A

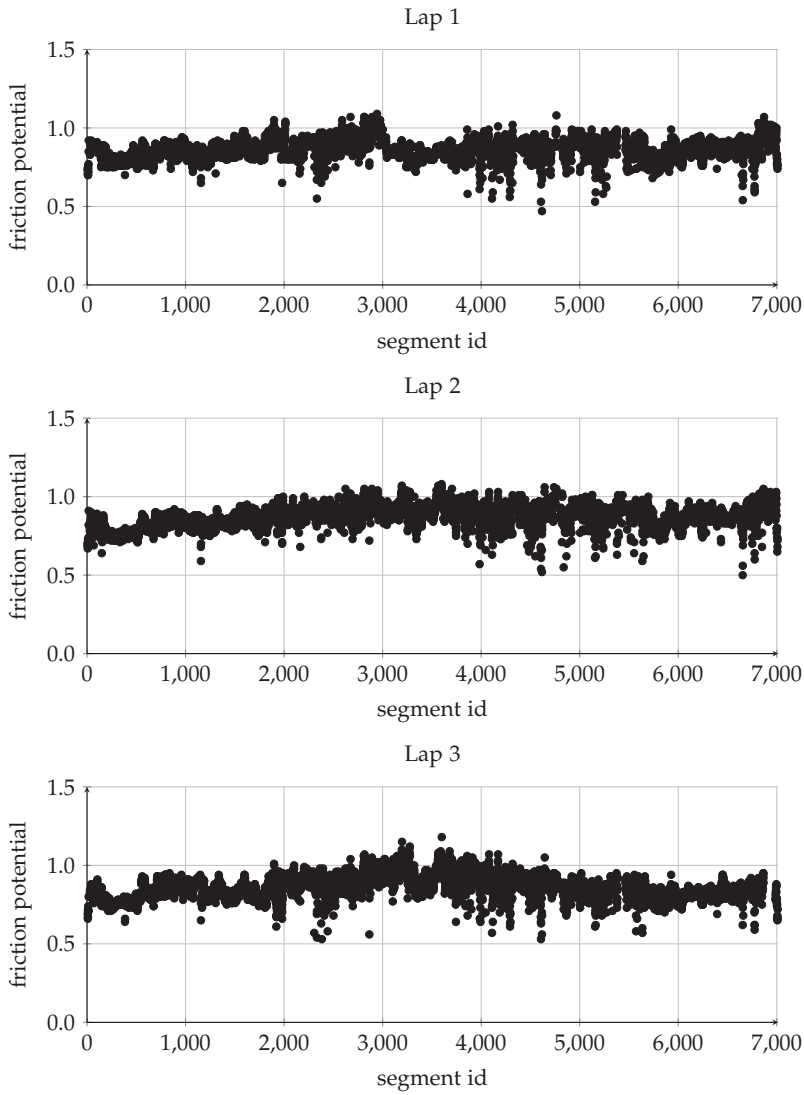

Figure C.6: RoadSTAR measurements on the public road track evaluated over 5 m segments without velocity correction using tyre B

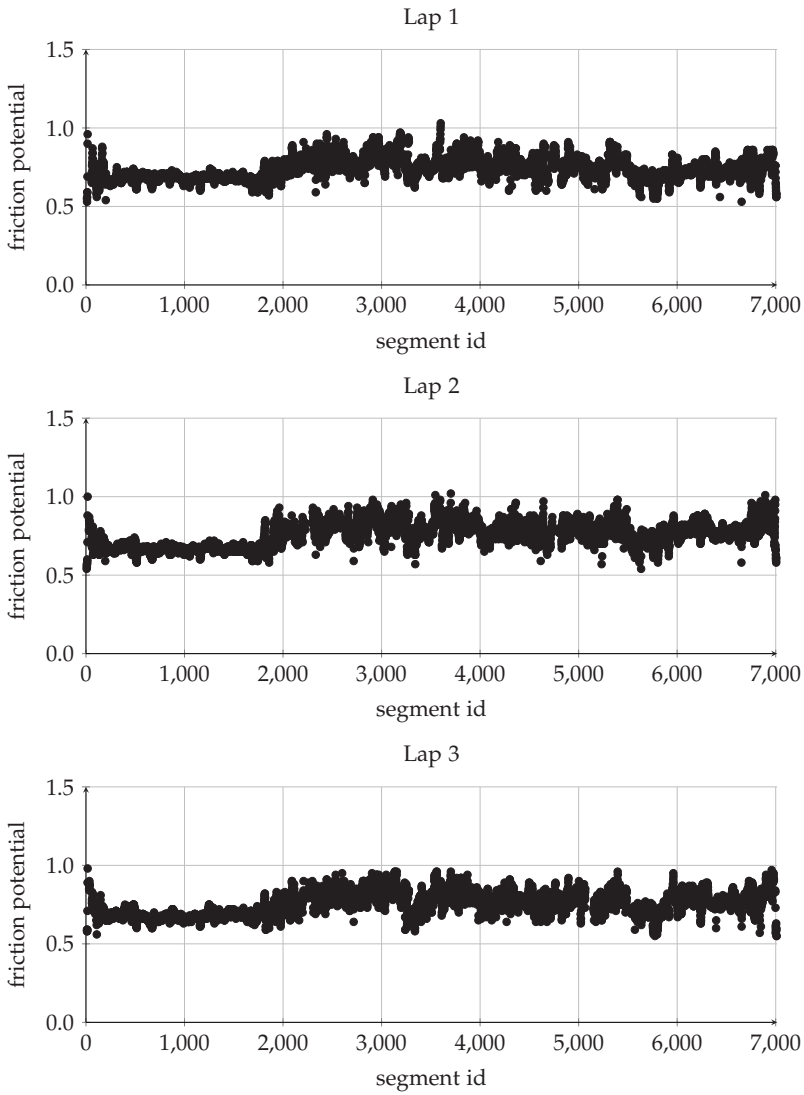

Figure C.7: RoadSTAR measurements on the public road track evaluated over 5 m segments without velocity correction using the PIARC tyre

Bibliography

1. BÄUMER, M.; HAUTZINGER, H.; PFEIFFER, M. et al. *Fahrleistungserhebung 2014 – Inlandsfahrleistung und Unfallrisiko*. Bundesanstalt für Straßenwesen, 2017.
2. KIM, E.; MUENNIG, P.; ROSEN, Z. Vision zero: a toolkit for road safety in the modern era. *Injury Epidemiology*. 2017, vol. 4, no. 1.
3. SINGH, S. *Critical reasons for crashes investigated in the national motor vehicle crash causation survey*. United States. National Highway Traffic Safety Administration, 2015. Tech. rep. U.S. National Highway Safety Administration.
4. KLAUER, S. G.; DINGUS, T. A.; NEALE, V. L. et al. *The impact of driver inattention on near-crash/crash risk: An analysis using the 100-car naturalistic driving study data*. United States. National Highway Traffic Safety Administration, 2006. Tech. rep. U.S. Department of Transportation - National Highway Traffic Safety Administration.
5. COOKSON, G.; PISHUE, B. *The Impact of Parking Pain in the US, UK and Germany* [online]. 2017 [visited on 2019-10-30]. Available from: `http://www2.inrix.com/research-parking-2017`.
6. AGUA, F. *Simulation einer urbanen Mobilitätslösung basierend auf autonom fahrenden E-Robotaxen in München*. 2017. Research rep. Berylls Strategy advisors and TU München.
7. SAE STANDARD. J3016 Levels of Automated Driving. *SAE international taxonomy and definitions for terms related to on-road motor vehicle automated driving systems, levels of driving automation*. 2014.
8. BRACH, R.; BRACH, M. The Tire-Force Ellipse (Friction Ellipse) and Tire Characteristics. In: *SAE Technical Paper*. SAE International, 2011.
9. MÜLLER, G.; BRÄSEMANN, C.; JOAO, N. et al. *Unfallvermeidung durch Reibwertprognosen*. 2017. Research rep. Technische Universität Berlin, Institut für Land- und Seeverkehr / Fachgebiet Kraftfahrzeuge.

10. DELANNE, Y.; SCHAEFER, G.; LECHNER, D. et al. Vehicle Dynamics and tyre road friction performance models. In: *2nd international colloquium on vehicle tyre road interaction, Friction Potential And Safety, Prediction Of Handling Behaviour – external expert contribution*. 2001.

11. STATISTISCHES BUNDESAMT. *Verkehr; Verkehrsunfälle; 2017*. 2018. Tech. rep. Fachserie 8, Reihe 7.

12. SINGH, K. B.; TAHERI, S. Estimation of tire-road friction coefficient and its application in chassis control systems. *Systems Science & Control Engineering*. 2015, vol. 3, no. 1, pp. 39–61.

13. LEX, C. *Estimation of the Maximum Coefficient of Friction between Tire and Road Based on Vehicle State Measurements*. 2015. PhD thesis. TU Graz.

14. BRUZELIUS, F.; SVENDENIUS, J.; YNGVE, S. et al. Evaluation of tyre to road friction estimators, test methods and metrics. *International Journal of Vehicle Systems Modelling and Testing*. 2010, vol. 5, no. 2-3, pp. 213–236.

15. TECHNICAL COMMITTEE ISO/TC 22. *ISO 8349:2002 Road vehicles – Measurement of road surface friction*. Geneva, CH, 2002. Standard. International Organization for Standardization.

16. ECONOMIC COMMISSION FOR EUROPE OF THE UNITED NATIONS (UNECE). *Regulation No. 13 of the Economic Commission for Europe of the United Nations (UN/ECE) – Uniform provisions concerning the approval of vehicles of categories M, N and O with regard to braking [2016/194]*. 2016. Standard. United Nations Economic Commission for Europe.

17. ECONOMIC COMMISSION FOR EUROPE OF THE UNITED NATIONS (UNECE). *Regulation No. 117 of the Economic Commission for Europe of the United Nations (UN/ECE) – Uniform provisions concerning the approval of tyres with regard to rolling sound emissions and/or to adhesion on wet surfaces and/or to rolling resistance [2016/1350]*. 2016. Standard. United Nations Economic Commission for Europe.

18. MAURER, P. *Aspekte der Fahrbahngriffigkeit und ihr Einfluss auf erreichbare PKW-Bremsverzögerungen*. 2007. Tech. rep., 564. Bundesministerium für Verkehr, Innovation und Technologie.

19. SLUIS, S. van der. *Ableitung einer Wechselbeziehung zwischen Griffigkeit, Geschwindigkeit und Haltesichtweite anhand realer Bremsvorgänge*. 2003. PhD thesis. RWTH Aachen University.

20. MÜLLER, G.; LESCHIK, C.; GREGULL, V. et al. *Unfallvermeidung durch Reibwertprognosen - Umsetzung und Anwendung*. 2019. Research rep. Technische Universität Berlin, Institut für Land- und Seeverkehr / Fachgebiet Kraftfahrzeuge.

21. LAJEWSKI, T.; RAUH, J.; MÜLLER, S. Measuring a reference friction potential by anti-lock braking tests. In: BARGENDE, M.; REUSS, H.-C.; WIEDEMANN, J. (eds.). *16. Internationales Stuttgarter Symposium*. Wiesbaden: Springer Fachmedien Wiesbaden, 2016, pp. 419–433.

22. WALLMAN, C.-G.; ÅSTRÖM, H. *Friction measurement methods and the correlation between road friction and traffic safety: A literature review*. Swedish National Road and Transport Research Institute, 2001.

23. HALL, J.; SMITH, K. L.; TITUS-GLOVER, L. et al. Guide for pavement friction. *Final Report for NCHRP Project*. 2009, pp. 01–43.

24. ZEHNTER TESTING INSTRUMENTS. *SRT 5800 Portable Skid Resistance Tester* [online]. 2018 [visited on 2018-03-17]. Available from: `http://www.zehntner.com/products/categories/skid-resistance/srt-5800`.

25. ASTM. *Standard Test Method for Measuring Surface Frictional Properties Using the British Pendulum Tester*. West Conshohocken, PA, 2018. Standard. ASTM International.

26. ASI, I. M. Evaluating skid resistance of different asphalt concrete mixes. *Building and Environment*. 2007, vol. 42, no. 1, pp. 325–329.

27. BRITTAIN, S. *Comparison of SCRIM and SKM sideway-force skid resistance devices*. 2014. Tech. rep. Transport Research Laboratory.

28. BUSLAPS, A.; ALTEMEIER, T. *Erfassen und Bewerten von Oberflächeneigenschaften*. Ed. by BUNDESANSTALT FÜR STRASSENWESEN. 2017.

29. MAURER, P. *Fahrbahngriffigkeitsmessungen im Wandel der Zeit*. 2009.

30. COMITÉ TECHNIQUE 1 CARACTÉRISTIQUES DE SURFACE / TECHNICAL COMMITTEE 1 SURFACE CHARACTERISTICS. *Specification for a standard test tyre for friction coefficient measurement of a pavement surface: ribbed test tyre*. 2009. Tech. rep. PIARC – World Road Association.

31. ZAID, N.; HAININ, M.; IDHAM, M. et al. Evaluation of Skid Resistance Performance Using British Pendulum and Grip Tester. In: *IOP Conference Series: Earth and Environmental Science*. IOP Publishing, 2019, vol. 220. No. 1.

32. MÜLLER, G.; MÜLLER, S. Comparison of standardised roughness measurement methods and friction potential tests under real conditions. In: *Bericht der Bundesanstalt für Straßenwesen*. Bundesanstalt für Straßenwesen, 2017, vol. 117.

33. WAMBOLD, J. C.; HENRY, J. International PIARC experiment to compare and harmonize texture and skid resistance measurement. *Nordic Road and Transport Research*. 1994.

34. FUENTES, L. G. *Investigation of the factors influencing skid resistance and the international friction index*. 2009. PhD thesis. University of South Florida.

35. DESCORNET, G.; SCHMIDT, B.; BOULET, M. et al. Harmonization of European routine and research measuring equipment for skid resistance. In: *Forum of European National Highway Research Laboratories – FEHRL. Report*. 2006, vol. 1.

36. ANDERSSON, M.; BRUZELIUS, F.; CASSELGREN, J. et al. Road friction estimation, part II. *Saab Automobile AB, Trollhättan, Sweden*. 2010.

37. KHALEGHIAN, S.; EMAMI, A.; TAHERI, S. A technical survey on tire-road friction estimation. *Friction*. 2017, vol. 5, no. 2, pp. 123–146.

38. LI, K.; MISENER, J. A.; HEDRICK, K. On-board road condition monitoring system using slip-based tyre-road friction estimation and wheel speed signal analysis. *Proceedings of the Institution of Mechanical Engineers, Part K: Journal of Multibody Dynamics*. 2007, vol. 221, no. 1, pp. 129–146.

39. MÜLLER, S.; UCHANSKI, M.; HEDRICK, K. Estimation of the maximum tire-road friction coefficient. *Journal of dynamic systems, measurement, and control*. 2003, vol. 125, no. 4, pp. 607–617.

40. AHN, C.; PENG, H.; TSENG, H. E. Robust estimation of road frictional coefficient. *IEEE Transactions on Control Systems Technology*. 2011, vol. 21, no. 1, pp. 1–13.

41. GUSTAFSSON, F. Slip-based tire-road friction estimation. *Automatica*. 1997, vol. 33, no. 6, pp. 1087–1099.

42. YI, K.; HEDRICK, K.; LEE, S.-C. Estimation of Tire-Road Friction Using Observer Based Identifiers. *Vehicle System Dynamics*. 1999, vol. 31, no. 4, pp. 233–261.

43. LEE, C.; HEDRICK, K.; YI, K. Real-time slip-based estimation of maximum tire-road friction coefficient. *IEEE/ASME Transactions on Mechatronics*. 2004, vol. 9, no. 2, pp. 454–458.

44. LI, B.; DU, H.; LI, W. A novel cost effective method for vehicle tire-road friction coefficient estimation. In: *Advanced Intelligent Mechatronics (AIM), 2013 IEEE/ASME International Conference on Advanced Intelligent Mechatronics*. 2013, pp. 1528–1533.

45. RAJAMANI, R.; PHANOMCHOENG, G.; PIYABONGKARN, D. et al. Algorithms for real-time estimation of individual wheel tire-road friction coefficients. *IEEE/ASME Transactions on Mechatronics*. 2012, vol. 17, no. 6, pp. 1183–1195.

46. AHN, C. S. *Robust Estimation of Road Friction Coefficient for Vehicle Active Safety Systems*. 2011. PhD thesis. University of Michigan.

47. UCHANSKI, M. R. *Road friction estimation for automobiles using digital signal processing methods*. 2001. PhD thesis. University of California.

48. DEUR, J.; IVANOVIĆ, V.; PAVKOVIĆ, D. et al. On low-slip tire friction behavior and modeling for different road conditions. In: *19th IAVSD Symposium Dynamics of Vehicles on Roads and Tracks*. 2005.

49. ONO, E.; ASANO, K.; SUGAI, M. et al. ESTIMATION OF AUTOMOTIVE TIRE FORCE CHARACTERISTICS USING WHEEL VELOCITY. In: *IFAC Proceedings Volumes - 15th IFAC World Congress*. 2002, vol. 35, pp. 175–180. No. 1.

50. VILLAGRA, J.; D'ANDRÉA-NOVEL, B.; FLIESS, M. et al. A diagnosis-based approach for tire-road forces and maximum friction estimation. *Control Engineering Practice*. 2011, vol. 19, no. 2, pp. 174–184. ISSN 0967-0661.

51. RAY, L. R. Nonlinear Tire Force Estimation and Road Friction Identification: Simulation and Experiments. *Automatica*. 1997, vol. 33, no. 10, pp. 1819–1833.

52. ALBINSSON, A.; BRUZELIUS, F.; JACOBSON, B. Friction utilization for tyre-road friction estimation on snow: An experimental study. In: *Proceedings of the 13th International Symposium on Advanced Vehicle Control (AVEC' 16)*. 2016.

53. HAHN, J.-O.; RAJAMANI, R.; ALEXANDER, L. GPS-based real-time identification of tire-road friction coefficient. *IEEE Transactions on Control Systems Technology*. 2002, vol. 10, no. 3, pp. 331–343.

54. BAFFET, G.; CHARARA, A.; STEPHANT, J. Sideslip angle, lateral tire force and road friction estimation in simulations and experiments. In: *2006 IEEE Conference on Computer Aided Control System Design, 2006 IEEE International Conference on Control Applications, 2006 IEEE International Symposium on Intelligent Control*. 2006, pp. 903–908.

55. SOLMAZ, S.; BAŞLAMIŞLI, S. Simultaneous estimation of road friction and sideslip angle based on switched multiple non-linear observers. *IET Control Theory & Applications*. 2012, vol. 6, no. 14, pp. 2235–2247.

56. MATILAINEN, M. J.; TUONONEN, A. J. Tire friction potential estimation from measured tie rod forces. In: *2011 IEEE Intelligent Vehicles Symposium (IV)*. 2011, pp. 320–325.

57. HSU, Y.-H. J. *Estimation and Control of Lateral Tire Force Using Steering Torque*. 2009. PhD thesis. Stanford University.

58. HSU, Y.-H. J.; LAWS, S. M.; GERDES, J. C. Estimation of tire slip angle and friction limits using steering torque. *IEEE Transactions on Control Systems Technology*. 2010, vol. 18, no. 4, pp. 896–907.

59. BOBIER, C. G. *A Phase portrait approach to vehicle stabilization and envelope control*. 2012. PhD thesis. Stanford University.

60. MATSUDA, T.; JO, S.-I.; NISHIRA, H. et al. Instantaneous estimation of road friction based on front tire SAT using Kalman filter. *SAE International Journal of Passenger Cars – Mechanical Systems*. 2013, vol. 6, no. 2013-01-0680, pp. 147–153.

61. SHAO, L.; LEX, C.; HACKL, A. et al. Estimation of Tire Road Friction during Vehicle Steering. In: *AVEC'16*. 2016.

62. NISKANEN, A. J.; XIONG, Y.; TUONONEN, A. J. Towards the friction potential estimation: A model-based approach to utilizing in-tyre accelerometer measurements. In: *2016 IEEE Intelligent Vehicles Symposium (IV)*. 2016, pp. 625–629.

63. SINGH, K. B.; ARAT, M. A.; TAHERI, S. An intelligent tire based tire-road friction estimation technique and adaptive wheel slip controller for antilock brake system. *Journal of Dynamic Systems, Measurement, and Control*. 2013, vol. 135, no. 3.

64. MATILAINEN, M.; TUONONEN, A. J. Tyre contact length on dry and wet road surfaces measured by three-axial accelerometer. *Mechanical Systems and Signal Processing*. 2015, vol. 52-53, pp. 548–558.

65. TUONONEN, A. J. On-board estimation of dynamic tyre forces from optically measured tyre carcass deflections. *International journal of heavy vehicle systems*. 2009, vol. 16, no. 3, pp. 362–378.

66. KOSKINEN, S.; PEUSSA, P. *Fricti@n*. 2009. Deliverable 13: Final Report. EU.

67. EICHHORN, U.; ROTH, J. Prediction and monitoring of tyre/road friction. In: *Proceedings of FISITA, London*. 1992.

68. ZHANG, Y.; MCDANIEL, J. G.; WANG, M. L. Estimation of Pavement Macrotexture by Principal Component Analysis of Acoustic Measurements. *Journal of Transportation Engineering*. 2014, vol. 140, no. 2.

69. BOYRAZ, P. Acoustic road-type estimation for intelligent vehicle safety applications. *International Journal of Vehicle Safety*. 2014, vol. 7, no. 2, pp. 209–222.

70. ABDIĆ, I.; FRIDMAN, L.; BROWN, D. E. et al. Detecting road surface wetness from audio: A deep learning approach. In: *23rd International Conference on Pattern Recognition (ICPR)*. 2016, pp. 3458–3463.

71. AKAMA, S.-I.; TABARU, T.; SHIN, S. Bayes estimation of road surface using road noise. In: *30th Annual Conference of IEEE Industrial Electronics Society, 2004. IECON 2004*. 2004, vol. 3, pp. 2923–2928.

72. HOLZMANN, F.; BELLINO, M.; SIEGWART, R. et al. Predictive estimation of the road-tire friction coefficient. In: *2006 IEEE Conference on Computer Aided Control System Design, 2006 IEEE International Conference on Control Applications, 2006 IEEE International Symposium on Intelligent Control*. 2006, pp. 885–890.

73. HARTMANN, B.; AMTHOR, M.; JARISA, W. Fahrbahnzustandserkennung als grundlegender Baustein für das Umfeldmodell. *VDI Reifen, Fahrwerk, Fahrbahn*. 2015.

74. PANHUBER, C.; LIU, B.; SCHEICKL, O. et al. Recognition of Road Surface Condition Through an On-Vehicle Camera Using Multiple Classifiers. In: *Proceedings of SAE-China Congress 2015: Selected Papers*. Singapore: Springer Singapore, 2016, pp. 267–279.

75. CASSELGREN, J.; KUTILA, M.; JOKELA, M. Slippery road detection by using different methods of polarised light. *Advanced Microsystems for Automotive Applications 2012*. 2012, pp. 207–220.

76. HÄKLI, J.; SÄILY, J.; KOIVISTO, P. et al. Road surface condition detection using 24 GHz automotive radar technology. In: *2013 14th International Radar Symposium (IRS)*. 2013, vol. 2, pp. 702–707.

77. RUDOLF, H.; WANIELIK, G.; SIEBER, A. J. Road condition recognition using microwaves. In: *Proceedings of Conference on Intelligent Transportation Systems*. 1997, pp. 996–999.

78. FUCHS, H.; HOFMANN, F.; LÖHR, H. et al. Vehicle-2-X. In: *Handbook of Driver Assistance Systems: Basic Information, Components and Systems for Active Safety and Comfort*. Ed. by WINNER, H.; HAKULI, S.; LOTZ, F. et al. Cham: Springer International Publishing, 2016, pp. 663–684.

79. BALDESSARI, R.; BÖDEKKER, B.; DEEGENER, M. et al. *Car-2-car communication consortium-manifesto*. 2007.

80. JAEGER, A.; HUSS, S. A. The weather hazard warning in simTD: A design for road weather related warnings in a large scale Car-to-X field operational test. In: *2011 11th International Conference on ITS Telecommunications*. 2011, pp. 375–380.

81. JAEGER, A. *Weather Hazard Warning Application in Car-to-X Communication*. Springer, 2016.

82. PANAHANDEH, G.; EK, E.; MOHAMMADIHA, N. Road friction estimation for connected vehicles using supervised machine learning. In: *2017 IEEE Intelligent Vehicles Symposium (IV)*. 2017, pp. 1262–1267.

83. KUMMER, H. W. *Unified theory of rubber and tire friction*. Pennsylvania State University, College of Engineering, 1966.

84. PERSSON, B. N. J. Theory of rubber friction and contact mechanics. *The Journal of Chemical Physics*. 2001, vol. 115, no. 8, pp. 3840–3861.

85. TOLPEKINA, T. V.; PERSSON, B. N. J. Adhesion and Friction for Three Tire Tread Compounds. *Lubricants*. 2019, vol. 7, no. 3.

86. TECHNICAL COMMITTEE ISO/TC 43/SC 1. *Characterization of pavement texture by use of surface profiles – Part 2: Terminology and basic requirements related to pavement texture profile analysis*. Berlin, 2002. Tech. rep., ISO 13473-2:2002. International Organization for Standardization.

87. PERSSON, B. N. J.; ALBOHR, O.; TARTAGLINO, U. et al. On the nature of surface roughness with application to contact mechanics, sealing, rubber friction and adhesion. *Journal of Physics: Condensed Matter*. 2005, vol. 17, no. 1, R1.

88. PRATICÒ, F.; VAIANA, R. A study on the relationship between mean texture depth and mean profile depth of asphalt pavements. *Construction and Building Materials*. 2015, vol. 101, pp. 72–79.

89. TECHNICAL COMMITTEE ISO/TC 43/SC 1. *Characterization of pavement texture by use of surface profiles – Part 1: Determination of mean profile depth*. Berlin, 2002. Tech. rep., ISO 13473-1:1997. International Organization for Standardization.

90. EICHHORN, U. *Reibwert zwischen Reifen und Fahrbahn-Einflußgrößen und Erkennung*. VDI, 1994.

91. KLEMPAU, F. Untersuchungen zum Aufbau eines Reibwertvorhersagesystems im fahrenden Fahrzeug. *Fortschritt Berichte VDI Reihe 12 Verkehrstechnik Fahrzeugtechnik*. 2004.

92. KANE, M.; DO, M. T.; PIAU, J. M. On the Study of Polishing of Road Surface under Traffic Load. *Journal of Transportation Engineering*. 2010, vol. 136, no. 1, pp. 45–51.

93. HOFKO, B.; KUGLER, H.; CHANKOV, G. et al. A laboratory procedure for predicting skid and polishing resistance of road surfaces. *International Journal of Pavement Engineering*. 2019, vol. 20, no. 4, pp. 439–447.

94. KUGLER, H.; HOFKO, B.; SPIELHOFER, R. *Prognose der Griffigkeit von Fahrbahnoberflächen - Entwicklung eines Labor-Verfahrens PROGRIP*. Bundesministerium für Verkehr, Innovation und Technologie Abteilung Mobilitäts- und Verkehrstechnologien, 2015. Research rep. TPA – Gesellschaft für Qualitätssicherung und Innovation GmbH.

95. VEITH, A. G. The most complex tire-pavement interaction: tire wear. In: *The Tire Pavement Interface*. ASTM International, 1986.

96. KANAFI, M. M.; KUOSMANEN, A.; PELLINEN, T. K. et al. Macro- and microtexture evolution of road pavements and correlation with friction. *International Journal of Pavement Engineering*. 2015, vol. 16, no. 2, pp. 168–179.

97. AHAMMED, M. A.; TIGHE, S. L. Effect of short-term and long-term weather on pavement surface friction. *International Journal of Pavement Research and Technology*. 2010, vol. 3, no. 6, p. 295.

98. GONZALEZ, O. D. *Evaluation of pavement surface friction seasonal variations*. 2009. PhD thesis. Virginia Polytechnic Institute and State University.

99. KWAN, K. S. *The role of penetrant structure in the transport and mechanical properties of a thermoset adhesive*. 1998. PhD thesis. Virginia Polytechnic Institute and State University.

100. ACHORN, P. J.; FERRILLO, R. G. Comparison of thermal techniques for glass transition measurements of polystyrene and cross-linked acrylic polyurethane films. *Journal of Applied Polymer Science*. 1994, vol. 54, no. 13, pp. 2033–2043.

101. HOGE, K. G. An experimental study to verify the time-temperature superposition principle. *International Journal of Fracture Mechanics*. 1971, vol. 7, no. 2, pp. 229–232.

102. GROSCH, K. The relation between the friction and visco-elastic properties of rubber. *Proceedings of the Royal Society of London. Series A. Mathematical and Physical Sciences*. 1963, vol. 274, no. 1356, pp. 21–39.

103. WILLIAMS, M. L.; LANDEL, R. F.; FERRY, J. D. The temperature dependence of relaxation mechanisms in amorphous polymers and other glass-forming liquids. *Journal of the American Chemical Society*. 1955, vol. 77, no. 14, pp. 3701–3707.

104. LUO, W.; HU, X.; WANG, C. et al. Frequency- and strain-amplitude-dependent dynamical mechanical properties and hysteresis loss of CB-filled vulcanized natural rubber. *International Journal of Mechanical Sciences*. 2010, vol. 52, no. 2, pp. 168–174.

105. HEINRICH, G.; KLÜPPEL, M. Rubber friction, tread deformation and tire traction. *Wear*. 2008, vol. 265, no. 7, pp. 1052–1060.

106. WESTERMANN, S.; PETRY, F.; BOES, R. et al. Experimental investigations into the predictive capabilities of current physical rubber friction theories. *Kautschuk Gummi Kunststoffe*. 2004, vol. 57, no. 12, pp. 645–650.

107. UECKERMANN, A.; WANG, D.; OESER, M. et al. A contribution to non-contact skid resistance measurement. *International Journal of Pavement Engineering*. 2015, vol. 16, no. 7, pp. 646–659.

108. GAL, L. *Investigation and modelling of rubber stationary friction on rough surfaces*. 2007. PhD thesis. Leibniz Universität Hannover.

109. SHARP, R. S.; GRUBER, P.; FINA, E. Circuit racing, track texture, temperature and rubber friction. *Vehicle System Dynamics*. 2016, vol. 54, no. 4, pp. 510–525.

110. PERSSON, B. N. J. Rubber friction: role of the flash temperature. *Journal of Physics: Condensed Matter*. 2006, vol. 18, no. 32, p. 7789.

111. GOLDEN, J. A molecular theory of adhesive rubber friction. *Journal of Physics A: Mathematical and General*. 1975, vol. 8, no. 6, p. 966.

112. LORENZ, B. *Contact mechanics and friction of elastic solids on hard and rough substrates*. Forschungszentrum Jülich, 2012. PhD thesis. RWTH Aachen University.

113. EUROPEAN UNION. Commision Regulation (EC) No 1221/2009 OF THE EUROPEAN PARLIAMENT AND OF THE COUNCIL. *Official Journal of the European Union*. 2009.

114. GABRIEL, C. F. S.; ALENCAR PADUA GABINO, A. de; SOUSA, A. M. F. de et al. Tire tread rubber compounds with ternary system filler based on carbon black, silica, and metakaolin: Contribution of silica/metakaolin content on the final properties. *Journal of Elastomers & Plastics*. 2019, vol. 51, no. 7-8, pp. 712–726.

115. EUROPEAN UNION. Commission Regulation (EU) No. 228/2011 amending Regulation (EC) No 1222/2009 of the European Parliament and of the Council with regard to the wet grip testing method for C1 tyres. *Official Journal of the European Union*. 2011.

116. LAMBOURN, R.; VINER, H. Friction tests on contaminated road surfaces. In: *Institute of Traffic Accident Investigators (ITAI) International Conference, 7th, Dunblane*. 2005.

117. PERSSON, B. N. J.; TARTAGLINO, U.; ALBOHR, O. et al. Rubber friction on wet and dry road surfaces: The sealing effect. *Phys. Rev. B*. 2005, vol. 71.

118. CLARK, S. K. *Mechanics of pneumatic tires*. U.S. Government Printing Office, 1981.

119. TUONONEN, A.; HARTIKAINEN, L. Optical position detection sensor to measure tyre carcass deflections in aquaplaning. *International Journal of Vehicle Systems Modelling and Testing*. 2008, vol. 3, no. 3, pp. 189–197.

120. HORNE, W. B.; DREHER, R. C. *Phenomena of pneumatic tire hydroplaning*. National Aeronautics and Space Administration, 1963.

121. BROWNE, A.; CHENG, H.; KISTLER, A. Dynamic hydroplaning of pneumatic tires. *Wear*. 1972, vol. 20, pp. 1–28.

122. YEAGER, R. W. Tire hydroplaning: testing, analysis, and design. In: *The Physics of Tire Traction*. Springer, 1974, pp. 25–63.

123. GALLAWAY, B. M.; IVEY, D.; ROSS, H. E. et al. *Tentative Pavement and Geometric Design Criteria for Minimizing Hydroplaning*. 1975. Tech. rep. U.S. Federal Highway Administration. Offices of Research and Development.

124. STOCKER, A.; DOTSON, J.; IVEY, D. L. *AUTOMOBILE TIRE HYDROPLANING. A STUDY OF WHEEL SPIN-DOWN AND OTHER VARIABLES*. 1974. Tech. rep. Texas A&M University.

125. CHO, J.; LEE, H.; SOHN, J. et al. Numerical investigation of hydroplaning characteristics of three-dimensional patterned tire. *European Journal of Mechanics-A/Solids*. 2006, vol. 25, no. 6, pp. 914–926.

126. VINCENT, S.; SARTHOU, A.; CALTAGIRONE, J.-P. et al. Augmented Lagrangian and penalty methods for the simulation of two-phase flows interacting with moving solids. Application to hydroplaning flows interacting with real tire tread patterns. *Journal of Computational Physics*. 2011, vol. 230, no. 4, pp. 956–983.

127. ELLA, S.; FORMAGNE, P.-Y.; KOUTSOS, V. et al. Investigation of rubber friction on snow for tyres. *Tribology International*. 2013, vol. 59, pp. 292–301.

128. TUONONEN, A. J.; KRISTON, A.; PERSSON, B. N. J. Multiscale physics of rubber-ice friction. *The Journal of Chemical Physics*. 2016, vol. 145, no. 11.

129. LAHAYNE, O.; PICHLER, B.; REIHSNER, R. et al. Rubber Friction on Ice: Experiments and Modeling. *Tribology Letters*. 2016, vol. 62, no. 2, p. 17.

130. SELIG, M.; LORENZ, B.; HENRICHMÖLLER, D. et al. Rubber friction and tire dynamics: A comparison of theory with experimental data. *Tire Science and Technology*. 2014, vol. 42, no. 4, pp. 216–262.

131. AMMON, D. *Modellbildung und Systementwicklung in der Fahrzeugdynamik*. Springer, 1997.

132. BAKKER, E.; NYBORG, L.; PACEJKA, H. B. Tyre Modelling for Use in Vehicle Dynamics Studies. In: *SAE Technical Paper*. SAE International, 1987.

133. PACEJKA, H. *Tire and vehicle dynamics*. 3rd ed. Elsevier, 2012.

134. SVENDENIUS, J.; WITTENMARK, B. Brush tire model with increased flexibility. In: *2003 European Control Conference (ECC)*. 2003, pp. 1863–1868.

135. MANCOSU, F.; SANGALLI, R.; CHELI, F. et al. A mathematical-physical 3D tire model for handling/comfort optimization on a vehicle: comparison with experimental results. *Tire Science and Technology*. 2000, vol. 28, no. 4, pp. 210–232.

136. ORTIZ, A.; CABRERA, J. A.; GUERRA, A. J. et al. An easy procedure to determine Magic Formula parameters: a comparative study between the starting value optimization technique and the IMMa optimization algorithm. *Vehicle System Dynamics*. 2006, vol. 44, no. 9, pp. 689–718.

137. ODHAMS, A.; COLE, D. Identification of a driver's preview steering control behaviour using data from a driving simulator and a randomly curved road path. In: *Proceedings 10th International Symposium AVEC*. 2010, pp. 605–609.

138. LAJEWSKI, T.; RAUH, J.; MÜLLER, S. Single Wheel Braking - A New Method to Measure Friction Potential on Public Roads. In: *The IAVSD International Symposium on Dynamics of Vehicles on Roads and Tracks*. 2019, pp. 1033–1041.

139. RILL, G. First order tire dynamics. In: *3rd European Conference on Computational Mechanics Solids, Structures and Coupled Problems in Engineering CA Mota Soares et. al.(ed.) Lisbon, Portugal*. 2006, pp. 5–8.

140. BESSELINK, I. J. M. Tire Characteristics and Modeling. In: *Vehicle Dynamics of Modern Passenger Cars*. Ed. by LUGNER, P. Springer International Publishing, 2019, pp. 47–108.

141. STEINAUER, B.; UECKERMANN, A.; MAERSCHALK, G. Analyse vorliegender messtechnischer Zustandsdaten und Erweiterung der Bewertungsparameter für Innerortsstraßen. Bundesanstalt für Straßenwesen. *Schriftenreihe Berichte der Bundesanstalt für Straßenwesen*. 2006, vol. 46.

142. GOODWIN, L. D.; LEECH, N. L. Understanding correlation: Factors that affect the size of r. *The Journal of Experimental Education*. 2006, vol. 74, no. 3, pp. 249–266.

143. DEUTSCHER WETTERDIENST. *Dokumentation zu Glättemeldeanlagen und SH10 Schlüssel* [online]. 2016 [visited on 2017-08-19]. Available from: `https://www.dwd.de/DE/leistungen/opendata/help/schluessel_datenformate/bufr/sws_sh10_code_pdf.html`.

144. WORLD METEREOLOGICAL ORGANIZATION. *Manual on Codes (WMO-No. 306)*. 2019.

145. DEUTSCHER WETTERDIENST. *Informationen zum Radarprodukt Komposit PG* [online]. 2016 [visited on 2017-08-19]. Available from: `https://www.dwd.de/DE/leistungen/radarprodukte/radarkomposit_pg.pdf`.

146. DEUTSCHER WETTERDIENST. *Tabellarische Übersicht der RADOLAN-Produkte* [online]. 2015 [visited on 2017-08-19]. Available from: `https://www.dwd.de/DE/leistungen/radolan/produktuebersicht/radolan_produktuebersicht_pdf.pdf`.

147. CASSELGREN, J. *Road surface characterization using near infrared spectroscopy*. 2011. PhD thesis. Luleå tekniska universitet.

148. WÅHLIN, J.; JONSSON, P.; BAAD, H. et al. Laboratory test of five different optical road condition sensors. *Proceedings of the SIRWEC*. 2016.

149. TODESCHINI, I.; NAPOLI, C. D.; PRETTO, I. et al. Thermal mapping as a valuable tool for road weather forecast and winter road maintenance: an example from the Italian Alps. In: THEMISTOCLEOUS, K.; HADJIMITSIS, D. G.; MICHAELIDES, S. et al. (eds.). *Fourth International Conference on Remote Sensing and Geoinformation of the Environment (RSCy2016)*. SPIE, 2016, vol. 9688, pp. 144–154.

150. CHAPMAN, L.; THORNES, J. E.; BRADLEY, A. V. Modelling of road surface temperature from a geographical parameter database. Part 2: Numerical. *Meteorological Applications*. 2001, vol. 8, pp. 421–436.

151. HAUSMANN, G. Verteilung von Tausalzen auf der Fahrbahn. *Schriftenreihe Berichte der Bundesanstalt für Straßenwesen*. 2009, no. 180.

152. BISHOP, C. M. *Pattern recognition and machine learning*. Springer, 2006.

153. PEDREGOSA, F.; VAROQUAUX, G.; GRAMFORT, A. et al. Scikit-learn: Machine Learning in Python. *Journal of Machine Learning Research*. 2011, vol. 12, pp. 2825–2830.

154. ABADI, M.; AGARWAL, A.; BARHAM, P. et al. *TensorFlow: Large-Scale Machine Learning on Heterogeneous Systems* [online]. 2015 [visited on 2019-08-07]. Available from: `https://www.tensorflow.org/`. Software available from tensorflow.org.

155. CHOLLET, F. et al. *Keras* [online]. 2018 [visited on 2018-08-06]. Available from: `https://keras.io`.

156. GANGANWAR, V. An overview of classification algorithms for imbalanced datasets. *International Journal of Emerging Technology and Advanced Engineering*. 2012, vol. 2, no. 4, pp. 42–47.

157. KLAUER, S. G.; DINGUS, T. A.; NEALE, V. L. et al. *Comparing Real-World Behaviors of Drivers with High Versus Low Rates of Crashes and Near Crashes*. United States. National Highway Traffic Safety Administration, 2009. Tech. rep. U.S. Department of Transportation - National Highway Traffic Safety Administration.

158. EUROPEAN CENTER FOR INFORMATION AND COMMUNICATION TECHNOLOGIES. *EuroFOT* [online]. 2012 [visited on 2017-03-03]. Available from: `http://www.eurofot-ip.eu/`.

159. AMMON, D. Systemtechnische Überlegungen auf dem Weg zum automatisierten Fahren. Was bleibt und was muss sich ändern, wenn der Algorithmus statt des Fahrers fährt? *VDI-Berichte*. 2013, no. 2205.

160. TECHNICAL COMMITTEE ISO/TC 22/SC 33. *Road Vehicles – Vehicle dynamics and road-holding ability – Vocabulary*. Berlin, 2011. Tech. rep., ISO 8855:2011. International Organization for Standardization.

161. RACELOGIC LTD. *VBOX 3i — 100Hz Data Logger* [online]. 2020 [visited on 2020-04-21]. Available from: `https://www.vboxautomotive.co.uk/index.php/de/products/data-loggers/vbox-3i`.

VDI verlag

Alle 23 Reihen der „Fortschritt-Berichte VDI“
in der Übersicht – bequem recherchieren unter:
elibrary.vdi-verlag.de

Und direkt bestellen unter:
www.vdi-nachrichten.com/shop

Reihe 01 Konstruktionstechnik / Maschinenelemente
Reihe 02 Fertigungstechnik
Reihe 03 Verfahrenstechnik
Reihe 04 Bauingenieurwesen
Reihe 05 Grund- und Werkstoffe/Kunststoffe
Reihe 06 Energietechnik
Reihe 07 Strömungstechnik
Reihe 08 Mess-, Steuerungs- und Regelungstechnik
Reihe 09 Elektronik/Mikro- und Nanotechnik
Reihe 10 Informatik/Kommunikation
Reihe 11 Schwingungstechnik
Reihe 12 Verkehrstechnik/Fahrzeugtechnik
Reihe 13 Fördertechnik/Logistik
Reihe 14 Landtechnik/Lebensmitteltechnik
Reihe 15 Umwelttechnik
Reihe 16 Technik und Wirtschaft
Reihe 17 Biotechnik/Medizintechnik
Reihe 18 Mechanik/Bruchmechanik
Reihe 19 Wärmetechnik/Kältetechnik
Reihe 20 Rechnergestützte Verfahren
Reihe 21 Elektrotechnik
Reihe 22 Mensch-Maschine-Systeme
Reihe 23 Technische Gebäudeausrüstung

OHNE PROTOTYP GEHT NICHTS IN SERIE.

Unser Podcast ist das Werkzeug, mit dem Sie Ihre Karriere in allen Phasen entwickeln – vom Studium bis zum Chefsessel. Egal, ob Sie Ingenieur*in, Mechatroniker*in oder Wissenschaftler*in sind: Prototyp begleitet Sie. Alle 14 Tage hören Sie die Redaktion von INGENIEUR.de und VDI nachrichten im Gespräch mit prominenten Gästen.

INGENIEUR.de
TECHNIK - KARRIERE - NEWS

PROTOTYP

Karriere-Podcast

JETZT REINHÖREN UND KOSTENFREI ABONNIEREN:
WWW.INGENIEUR.DE/PODCAST

IN KOOPERATION MIT VDI NACHRICHTEN

VDI

REIHE 12
VERKEHRSTECHNIK/
FAHRZEUGTECHNIK

NR. 816

ISBN 978-3-18-381612-5
E-ISBN: 978-3-18-681612-2

BAND
1|1

VOLUME
1|1